Experimental control of the beam properties of laser-accelerated protons and carbon ions

Inaugural-Dissertation

zur

Erlangung des Doktorgrades der

Mathematisch-Naturwissenschaftlichen Fakultät

der Heinrich-Heine-Universität Düsseldorf

vorgelegt von

Munib Amin

aus Münster

Dezember 2008

Aus dem Institut für Laser- und Plasmaphysik

der Heinrich-Heine-Universität Düsseldorf

Gedruckt mit der Genehmigung der

Mathematisch-Naturwissenschaftlichen Fakultät der

Heinrich-Heine-Universität Düsseldorf

Referent: Prof. Dr. O. Willi

Koreferent: Prof. Dr. U. Samm

Tag der mündlichen Prüfung: 05.02.2009

Abstract

The laser generation of energetic high quality beams of protons and heavier ions has opened up the door to a plethora of applications. These beams are usually generated by the interaction of a short pulse high power laser with a thin metal foil target. They could already be applied to probe transient phenomena in plasmas and to produce warm dense matter by isochoric heating. Other applications such as the production of radioisotopes and tumour radiotherapy need further research to be put into practice. To meet the requirements of each application, the properties of the laser-accelerated particle beams have to be controlled precisely.

In this thesis, experimental means to control the beam properties of laser-accelerated protons and carbon ions are investigated. The production and control of proton and carbon ion beams is studied using advanced ion source designs: Experiments concerning mass-limited (i.e. small and isolated) targets are conducted. These targets have the potential to increase both the number and the energy of laser-accelerated protons. Therefore, the influence of the size of a plane foil target on proton beam properties is measured. Furthermore, carbon ion sources are investigated. Carbon ions are of particular interest in the production of warm dense matter and in cancer radiotherapy. The possibility to focus carbon ion beams is investigated and a simple method for the production of quasi-monoenergetic carbon ion beams is presented.

This thesis also provides an insight into the physical processes connected to the production and the control of laser-accelerated ions. For this purpose, laser-accelerated protons are employed to probe plasma phenomena on laser-irradiated targets. Electric fields evolving on the surface of laser-irradiated metal foils and hollow metal foil cylinders are investigated. Since these fields can be used to displace, collimate or focus proton beams, understanding their temporal and spatial evolution is crucial for the design of controllable sources of laser-accelerated protons. In addition, laser-irradiated water droplets are investigated. In previous work, these mass-limited targets could be shown to be the origin of quasi-monoenergetic protons and deuterons. The experiments presented in this thesis aim at the elucidation of the processes taking place when a water droplet is irradiated by a short pulse high power laser.

Experimental results are interpreted using models and simulations. A particle simulation code using advanced rendering algorithms is presented. These algorithms are of general interest for particle simulation and image processing.

Zusammenfassung

Die lasergestützte Erzeugung hochqualitativer Strahlen energetischer Protonen und anderer Ionen hat eine Vielzahl von Anwendungen in greifbare Nähe rücken lassen. Diese Teilchenstrahlen werden für gewöhnlich durch die Wechselwirkung von Kurzpuls-Hochleistungslasern mit dünnen Metallfolien generiert und konnten bereits für die Analyse kurzlebiger Phänomene in Plasmen oder zum isochoren Heizen verwendet werden. Andere mögliche Anwendung wie die Herstellung von Radioisotopen und die Behandlung von Tumoren mittels Strahlentherapie erfordern weitere Forschung. Um die Anforderungen der Anwendungen zu erfüllen, müssen die Eigenschaften der Teilchenstrahlen präzise kontrolliert werden.

Die vorliegende Arbeit behandelt die experimentelle Kontrolle laserbeschleunigter Protonen und Kohlenstoffionen. Gegenstand der Experimente sind zunächst moderne Konzepte für die Erzeugung der Teilchenstrahlen. Eines dieser Konzepte ist die Verwendung isolierter Targets mit geringer Masse. Mithilfe dieser Targets kann eine Erhöhung der Anzahl und der Energie beschleunigter Protonen erreicht werden. In der vorliegenden Arbeit wird untersucht, wie die Strahleigenschaften von der Größe eines Folientargets abhängen. Ferner wird die Beschleunigung von Kohlenstoffionen behandelt. Kohlenstoffionen sind für bestimmte Anwendungen wie isochores Heizen und die Behandlung von Tumoren mittels Strahlentherapie von besonderer Bedeutung. Die Möglichkeit, Kohlenstoffionen zu fokussieren, wird untersucht, und eine einfache Methode zur Erzeugung quasi-monoenergetischer Kohlenstoffionen wird vorgestellt.

Darüber hinaus gewährt diese Arbeit einen Einblick in die Prozesse, die mit der lasergestützten Ionenbeschleunigung und der Kontrolle der Teilchenstrahlen zusammenhängen. Zu diesem Zweck werden laserbeschleunigte Protonen verwendet, um die elektrischen Felder in lasergenerierten Plasmen abzutasten. Die zeitliche und räumliche Entwicklung elektrischer Felder auf der Oberfläche dünner Metallfolientargets und hohler Metallfolienzylinder wird untersucht. Da diese Felder imstande sind, Protonenstrahlen zu versetzen, zu kollimieren oder zu fokussieren, ist das Verständnis der räumlichen und zeitlichen Entwicklung dieser Felder für die Entwicklung kontrollierbarer Teilchenstrahlquellen von großer Bedeutung. Des Weiteren werden die Prozesse untersucht, die durch die Wechselwirkung von Hochleistungs-Kurzpulslasern mit Wassertröpfchen ausgelöst werden. Diese Wassertröpfchen sind Targets mit einer geringen Masse. In vorangegangenen Arbeiten wurde gezeigt, dass von diesen Targets quasi-

monoenergetische Protonen und Deuteronen ausgehen können. Die in der vorliegenden Arbeit vorgestellten Experimente sollen die damit verbundenen Prozesse beleuchten.

Die Interpretation der experimentellen Ergebnisse erfolgt mithilfe von Modellen und Simulationen. Ein Teilchenstrahl-Simulationsprogramm und die verwendeten Algorithmen zu Bildsynthese werden vorgestellt. Diese Algorithmen sind von generellem Interesse für Teilchensimulation und Bildverarbeitung.

Diese Arbeit ist im Graduiertenkolleg 1203 – Dynamik heißer Plasmen (Düsseldorf, Jülich) entstanden.

Table of contents

1 Introduction

The laser-aided generation of fast ions is well-known for more than 20 years now [1]. In the early days of laser ion acceleration experiments however, lasers with nanosecond pulse duration and intensities of typically 10^{12}-10^{16} W/cm^2 were used to generate ion beams emitted from the coronal plasma of laser solid interaction. These beams exhibited a large emission angle, a low laminarity and broad energy spectra with maximum temperatures lying in the order of 100 keV per nucleon.

It was not until 1999, that three groups from different laboratories discovered that high quality ion beams could be generated using lasers with a pulse duration of about 1 ps or less and an intensity of at least 10^{18} W/cm^2 [2-5]: A plane foil target is put into the focus of the laser. The surface of this foil contains natural hydrogen contaminants like water and hydrocarbons. A single shot is fired onto the front side of the target and on the rear side a particle beam consisting mainly of protons is emitted into a narrow cone whose axis of symmetry is normal to the surface of the target. Today, this is still the most commonly used laser ion acceleration technique.

These beams show amazing properties: maximum proton energies of up to about 60 MeV [2], particle numbers of up to 10^{13} protons [2], a small virtual source size of a few micrometres [6] and a tremendously high laminarity [7].

With advanced experience in high power short pulse laser engineering and the availability of commercial laser systems, the pioneering work from 1999 has now become feasible in many laboratories. Obtaining the laser parameters needed for ion acceleration still requires a lot of expertise. But once this task is done, generating a high quality proton beam is quite easy. To do this, any thin foil target can be put in focus. Admittedly, the proton beam will not show all of the impressive properties mentioned above, but it will still contain some highly energetic particles.

However, the demands on particle beam properties have increased dramatically. In recent years, a plethora of possible applications for laser-accelerated protons and other ions has been identified and thoroughly investigated. Among these are:

- Plasma diagnostics: using laser-accelerated proton beams as a probe to investigate transient electric fields in dense plasmas

- Isochoric heating: instantly heating a volume of solid state matter up to a state that is almost unexplored yet
- Source for the injection of ions into a conventional accelerator
- Fast ignition: a path to inertial confinement fusion reducing the energy requirements for the laser that drives fusion
- Production of radioisotopes for tracing methods in medical diagnostics
- Tumour radiotherapy

Each application requires specific beam properties and each requirement exactly defines a demanding task for today's research. This might mean to provide a large number of comparatively low energetic protons for isochoric heating. Or it might mean to provide a monoenergetic particle spectrum, to focus the beam and to assure the shot-to-shot reproducibility for future tumour radiotherapy. For each application one will need to control the relevant beam properties precisely. Without control, laser ion acceleration is merely a physical effect. Only by actively controlling the beam properties we can turn this effect into a tool.

This work aims at contributing to the solution of this task. It is organised in the following way:

Chapters 2 to 4 contain fundamental information about laser ion acceleration:

- Chapter 2 provides insight into the standard of knowledge about the acceleration process.
- Chapter 3 offers a description of the most important beam properties.
- Chapter 4 gives an overview on established and future applications for the laser acceleration of protons and heavier ions.

In Chapters 5 to 7, a description of the experiments conducted in the scope of this work is given. Results are presented and analysed.

- In Chapter 5, experimental methods used in this work are explained.
- Chapter 6 addresses the challenges of the production and control of proton and carbon ion beams. The advantages of mass-limited (i.e. small and isolated) targets as a source of proton beams are highlighted. The possibility to focus carbon ion beams is investigated,

and a simple method for the production of quasi-monoenergetic carbon ion beams is presented.

- Chapter 7 provides a deeper insight into the physical processes connected to the production and control of laser-accelerated protons and heavier ions. Laser-accelerated protons are used to probe plasma phenomena on laser-irradiated targets.

Chapter 8 summarises the results obtained in this work and provides a short outlook on future experiments.

In the appendix, computer algorithms developed for the analysis of experimental data are presented. These algorithms are of general interest for particle simulation and image processing. Additionally, the appendix provides a description of target fabrication that can be used for future experiments.

In the following, the term *laser ion acceleration* includes the acceleration of protons and refers to beams emitted from the rear side of a laser-irradiated target – not to hot ions from coronal plasmas as described in [1]. The term *conventional accelerators* refers to electrostatic and radiofrequency accelerators such as linear particle accelerators, synchrotrons and cyclotrons.

Working on the experiments presented in this thesis, the author acquired profound knowledge in the preparation and conduction of laser plasma experiments, in modelling transient plasma phenomena and in the simulation of particle beams. Preparation of the experiments included target material search and evaluation, target fabrication and target holder construction. The conduction of the experiments included beam alignment and timing, target preparation and alignment, and setting up particle detectors and beam diagnostics. The author developed a schedule for the experiments he was in charge of and coordinated the activities of the collaborators. To analyse experimental results, the author modelled plasma phenomena in a given target geometry and simulated particle beams to generate synthetic spectra and detector images that were compared to experimental data. The analysis also included the reconstruction of detector images and the retrieval of ion energy spectra from the coordinates of particles detected by a Thomson spectrometer. The author could contribute significantly to the understanding of physical processes by determining plasma parameters and by revealing and explaining features of the experimental results that would have been neglected without the analysis. The author developed a new particle beam simulation program and significantly increased the performance of the program by conceiving and implementing novel algorithms. The author contributed to several publications: The observation and analysis of laser plasma phenomena using a novel

diagnostic technique is reported in [8] and [9]. An overview on recent developments in the field of laser ion acceleration is given by [10].

2 The ion acceleration process

2.1 Laser electron interaction and electron transport

So far, there is no laser that is able to accelerate ions directly. The simple reason is that even the lightest ion – the proton – is much too heavy to be accelerated by the laser light field efficiently. The laser energy needs to be transferred to electrons first and passed on to the ions subsequently.

A single electron in a plane wave

Imagine a single electron located in the electromagnetic field of plane light wave. The Lorentz force acting on the electron equals:

$$\mathbf{F} = -e\left(\mathbf{E} + \mathbf{v} \times \mathbf{B}\right) \tag{2.1}$$

E and **B** denote the time dependent electric and magnetic fields of the light field, e the elementary charge and **v** the velocity of the electron. At first, let us consider the non-relativistic case, i.e. the kinetic energy of the electron will be small compared to its rest mass m. In this case, the influence of the magnetic field can be neglected and (2.1) reduces to:

$$\mathbf{F} = -e\,\mathbf{E} \qquad \Rightarrow \qquad \dot{\mathbf{v}} = -\frac{e\,\mathbf{E}}{m} \tag{2.2}$$

The time dependence of the electric field at the position of the electron is given by:

$$\mathbf{E}(t) = \mathbf{E}_0 \cos(\omega t) \tag{2.3}$$

Here, ω is the angular frequency of the plane wave and $\mathbf{E}_0$ the amplitude of the electric field. Thus, the time dependent velocity of the electron can be obtained by inserting (2.3) into (2.2). Simple integration yields:

$$\mathbf{v}(t) = -\frac{e\,\mathbf{E}_0}{m\,\omega} \sin(\omega t) \tag{2.4}$$

The electron performs sinusoidal oscillations as long as the light wave is present. But when the light wave fades, the electron will give its kinetic energy back to the electromagnetic field and

remains at rest in the end. This behaviour is a general problem. For the relativistic case it is expressed by the *Lawson-Woodward theorem* [11]:

The net energy gain of a relativistic electron interacting with an electromagnetic field in vacuum is zero.

Nevertheless, the Lawson-Woodward theorem implies several assumptions. There are some conditions that lead to a violation of this theorem and among these there is the *ponderomotive force*.

The ponderomotive force

The strange name alone gives us a hint that the ponderomotive force is not an idea that was developed only recently. Originally, this expression denoted the action of force fields on movable bodies and it was already in the 1840s that Kelvin conducted work on this topic [12]. In the following, a narrower definition will be used. Imagine again the electron quivering in the electric field. Using (2.4), the mean kinetic energy of the electron equals:

$$\begin{aligned} \overline{E}_{kin} &= \frac{1}{2} m \overline{\left(-\frac{e \mathbf{E}_0}{m \omega} \sin(\omega t) \right)^2} \\ &= \frac{e^2 \mathbf{E}_0^2}{2 m \omega^2} \overline{\sin^2}(\omega t) \\ &= \frac{e^2 \mathbf{E}_0^2}{4 m \omega^2} \end{aligned} \tag{2.5}$$

The mean kinetic energy is called the ponderomotive potential or – strictly speaking – the ponderomotive potential energy.

At first, we assumed the wave to be infinitely extended. For a focussed laser pulse, this is obviously not the case anymore. The intensity decreases with increasing distance from the beam propagation axis, and thus the ponderomotive potential decreases as well. The gradient of the potential is the ponderomotive force that pushes the electron away from the regions of higher intensity to regions of lower intensity. This effect can be illustrated in the following simplified way: An electron located at a position of high intensity is accelerated out of this region by a half cycle of the electric field. At its new position, the electron encounters a weaker light field whose electric field is not able to bring the electron back to its initial position during the second half cycle. Thus, the electron drifts towards the lower intensity regions while oscillating.

In the framework of this scenario, the electron can only be accelerated perpendicularly to the beam propagation axis. However, high intensity laser experiments show that electrons are accelerated into the forward direction. This can be attributed to relativistic effects.

The relativistic case

As soon as the electron approaches the speed of light, the Lorentz force acting on the electron due to the magnetic field cannot be neglected anymore. The $\mathbf{v} \times \mathbf{B}$ force pushes the electron into the forward direction. In combination with the influence of the electric field, the electron is ejected under a certain angle to the beam propagation axis (cf. Fig. 2.1).

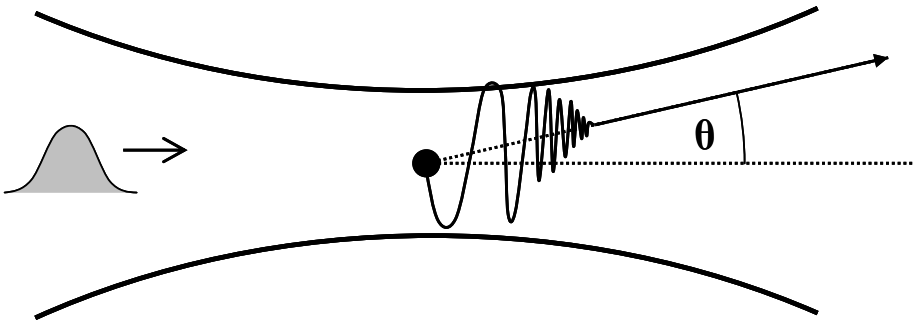

Fig. 2.1: Motion of a relativistic electron located in the focus of a high intensity laser (from [13]).

A simple kinematical approach (see [13]) yields the ejection angle θ:

$$\cos\theta = \sqrt{\frac{\gamma - 1}{\gamma + 1}} \tag{2.6}$$

Here, γ is the Lorentz factor:

$$\gamma = \frac{1}{\sqrt{1 - \left(\frac{v}{c}\right)^2}} \tag{2.7}$$

v and c denote the scalar electron velocity and the speed of light, respectively. From relation (2.6) one can easily see that θ decreases when the electron velocity approaches the speed of light. To get a feeling for the degree to which a laser is able to accelerate an electron to relativistic quiver

velocities, it is useful to define the so-called *normalised amplitude* (or *normalised vector potential* if the vector potential notation is used to describe the light wave) [13, 14]:

$$a_0 = \frac{v}{c} = \frac{e E_0}{m \omega c} = \frac{\lambda e E_0}{2 \pi m c^2} \tag{2.8}$$

In this case, v is the amplitude of the sinusoidal motion of the electron given by (2.4), neglecting relativistic effects. λ denotes the laser wavelength. If a_0 exceeds unity, we enter the relativistic regime.

From (2.8) it follows that:

$$E_0 = \frac{2 \pi m c^2 a_0}{\lambda e} \tag{2.9}$$

Applying concrete values* to the physical constants in (2.9), the laser light intensity I can be written as:

$$\begin{aligned} I &= \frac{1}{2} \varepsilon_0 c E_0^2 \\ &= \frac{a_0^2}{\lambda^2} \frac{2 \varepsilon_0 \pi^2 m^2 c^5}{e^2} \\ &= \frac{a_0^2}{\lambda^2} \cdot 1.37 \cdot 10^{18} \frac{W \, \mu m^2}{cm^2} \end{aligned} \tag{2.10}$$

where ε_0 is the vacuum permittivity. Thus, a laser with a wavelength of 1 μm can be considered relativistic if its intensity exceeds $1.37 \cdot 10^{18}$ W/cm^2.

The relativistic electron rolls down the ponderomotive potential in the forward direction. If this happens in plasma, collective effects cannot be neglected and therefore the ponderomotive potential needs be recalculated [16]. The energy gain of the electron is then given by:

* Values of physical constants in this work are taken from [15].

$$\Delta E = mc^2(\gamma - 1)$$

with (2.11)

$$\gamma = \sqrt{1 + a_0^2}$$

The electrons gain an exponential energy spectrum. Please note that in a real experiment, two different electron temperatures will be encountered. The second, high energy component is called *suprathermal* and represents only small fraction of the electrons. For further information, please refer to [17].

Electron transport

Treating a high power short pulse laser as a Gaussian pulse is a simplification. If one does not take any precautions, the high power pulse itself – the *main pulse* – is preceded by some radiation that is usually called *prepulse* and that contains enough energy to ionise the surface of the target (a more detailed description will be given in Section 5.1). Therefore, the main pulse interacts with a plasma and it is from this plasma that hot electrons are accelerated into the forward direction. The electrons are transported through the plasma and the target, and the non-trivial question that is still subject of investigations is: how? The current of laser-accelerated electrons reaches 10^7 A, exceeding the *Alfvén limit* [18] by several orders of magnitude [39]. Under astrophysical conditions, a current above the Alfvén limit cannot be attained, because the self-generated magnetic field gives rise to instabilities. But fortunately, this limit implies some preconditions that are violated in a dense medium [19]. Electron return currents flowing into the opposite direction partially neutralise the magnetic field and compensate the positive charge left behind by the laser-accelerated electrons. A detailed description of transport mechanisms cannot be given in the scope of this work. For further reading, [20] is recommended.

2.2 Target Normal Sheath Acceleration (TNSA)

Only a small part of the electrons exiting the foil target at its rear side is able to escape immediately. Most of the electrons are kept back by the positive charge that they leave behind in the target. They exit the target in a fountain-like formation that is accompanied by a toroidal

magnetic field [21] and spread over the target surface forming a *Debye sheath*[*] with a typical thickness of the order of 1 µm [5, 22]. This process is depicted in Fig. 2.2. From experimental results (e.g. [23, 24]) it can clearly be seen, that even on time scales of the laser pulse duration the electrons spread over an area that is much larger than the laser spot size. The electron sheath has a diameter that lies in the order of 100 µm while the laser usually is focussed to a spot of about 10 µm in diameter.

The electrons might re-enter the target from the rear side, are transported to the front side and accelerated by the laser again. This recirculation of the electrons is widely discussed and still being investigated [25]. In fact, if the front side of the target is not perturbed by the prepulse one can even show indirectly that on the front side an electron sheath is formed that is almost identical to the one on the rear side [26].

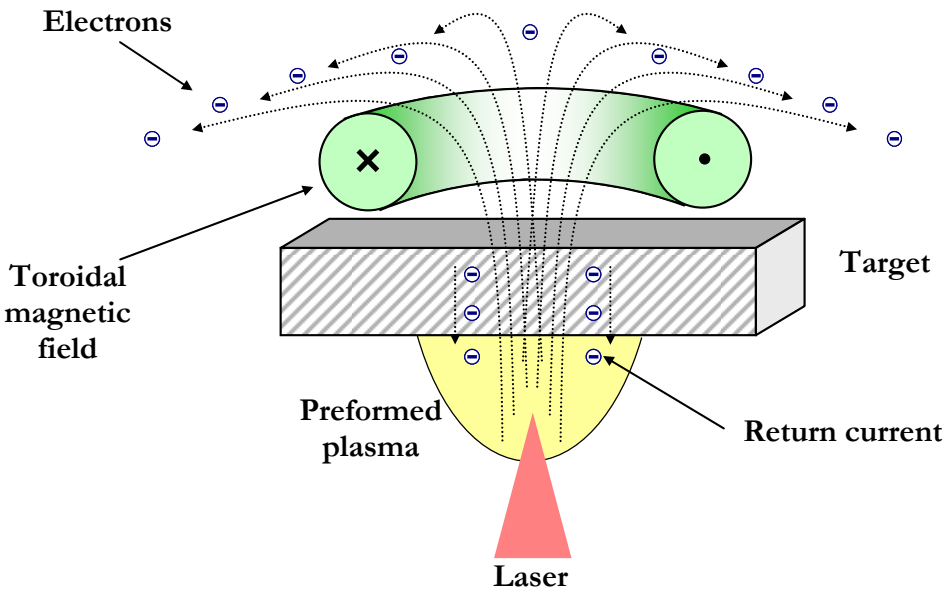

Fig. 2.2: Electrons are accelerated from the preformed plasma, transported through the target and spread over rear side.

On the picosecond time scale, the electrons form a sheath with a Gaussian density distribution [23, 24]. Between the positively charged target and the electron cloud an electrostatic field builds up that attains values of up to 10^{12} V/m, reaching its maximum in the centre of the electron distribution. A field of this magnitude can easily ionise the target surface via field ionisation. The

[*] In a plasma, the electric field of a positively charged particle can act only over a certain distance since it is screened by electrons. This distance is called the *Debye length*. The Debye sheath is a layer of the thickness of the Debye length.

electrostatic field acts on the ions on the surface and accelerates them into vacuum (Fig. 2.3). This process is called *Target Normal Sheath Acceleration* (TNSA).

If the target is not processed before using it, there is a natural layer of contaminants on its surface. This layer mainly consists of water and hydrocarbons. Having the highest charge-to-mass ratio of all ions, protons are accelerated most efficiently. Even if the target is handled with care and installed without touching it, the contaminant layer will dominate the acceleration process. At first sight, this might be surprising taking into account the large number of particles accelerated by this process. Are there really so many of them on an apparently clean surface? Using Rutherford backscattering, Fernández et al. measured the areal densities of H, C and O contaminants on Pd, Zr and W targets to lie in the order of 10^{16} atoms/cm^2 [27]. This seems to be a large number, but actually, 10^{16} protons still correspond to a tiny mass of water (~$1.5 \cdot 10^{-4}$ mg).

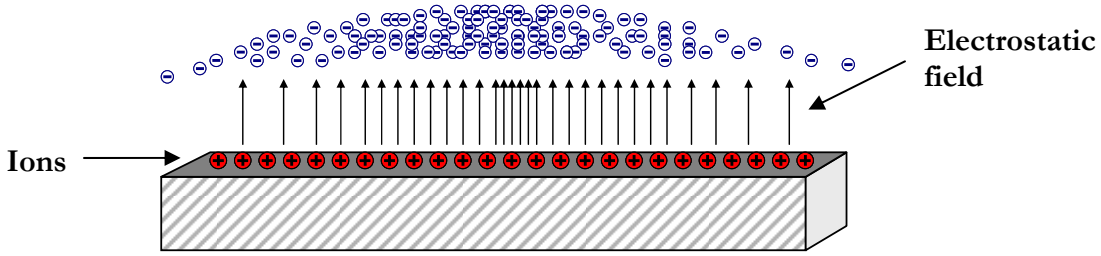

Fig. 2.3: An electrostatic field builds up between the electrons and the ions on the surface.

Please note that other acceleration processes have been discussed in the scientific community to explain the experimental results. In particular, there has been a long term controversy about acceleration from the front side of the target [3, 4]. The authors hold the view that the protons emitted from the rear side actually originate from the laser-irradiated side of the target. Different experiments unambiguously showed both front side [28] and rear side [29, 30] acceleration. Their dependence on experimental parameters was discussed [31]. After all, it could be shown that for a wide range of experimental parameters, rear side acceleration is the dominant process [32].

2.3 Modelling the acceleration process

The simple notion of ion acceleration as described above is useful to get an illustrative picture of the process, but it is not so useful to obtain quantitative information about the electric acceleration field or the maximum energy gained by the protons.

Our starting point will be the model suggested by Patrick Mora in 2003 [33]. It describes the acceleration as the result of charge separation in a plasma that expands into vacuum: An electric field is established between a positively charged region and a preceding negatively charged one. The electric field peaks at a definite position. At this position, the accelerated ions pile up and it is therefore called *ion front*. This ion front propagates with increasing velocity. The results of the model need to be handled with care since it is an isothermal model, i.e. the plasma does not cool down while expanding. Therefore, the model inherently overestimates the ion front velocity. This could be shown experimentally [34] and is consistent with the results obtained in this work. For the corresponding adiabatic model, see [35, 36]. The Mora model uses only one electron temperature. For a treatment of two electron temperatures, please refer to [37].

The initial situation is a plasma with a sharp boundary and a Boltzmann-like electron density distribution n_e:

$$n_e = n_{e0} \exp\left(\frac{e\,\Phi}{k_B\, T_e} \right) \tag{2.12}$$

where n_{e0} denotes the electron density in the unperturbed part of the plasma, Φ the electrostatic potential, k_B is the Boltzmann constant and T_e the electron temperature.

This is a one dimensional model – the plasma is simply located at $x < 0$, the boundary is at $x = 0$, the region $x > 0$ is occupied by vacuum. Knowing the electron density distribution, we have to set up the Poisson equation using Φ and n_e in order to obtain the electric field by integration:

$$\varepsilon_0\, \Delta\Phi = e\left(n_e - Z\, n_i \right) \tag{2.13}$$

where n_i is the ion density distribution and Z is the charge of the ions.

Furthermore, we need the equations of continuity and motion to describe the temporal and spatial evolution of the expansion:

$$\left(\frac{\partial}{\partial t} + v_i \frac{\partial}{\partial x} \right) n_i = -n_i \frac{\partial v_i}{\partial x} \tag{2.14}$$

$$\left(\frac{\partial}{\partial t}+v_i\frac{\partial}{\partial x}\right)v_i=-\left(\frac{Z\,e}{m_i}\right)\frac{\partial\Phi}{\partial x} \tag{2.15}$$

where v_i denotes the ion velocity and m_i is the ion mass.

In [33], a Lagrangian code is used to solve Eqs. (2.12)-(2.15) numerically. As a good approximation of the numerical result for the time-dependent electric field at the ion front, the following equation is provided:

$$E_{front}\approx 2\frac{E_{const}}{\sqrt{2\,e_{math}+\omega_{pi}^2 t^2}} \tag{2.16}$$

where e_{math} is the mathematical constant 2.71828…(the base of the natural logarithm), ω_{pi} is the ion plasma frequency:

$$\omega_{pi}=\sqrt{\frac{n_{e0}\,Z\,e^2}{m_i\,\varepsilon_0}},$$

and E_{const} is:

$$E_{const}=\sqrt{\frac{n_{e0}\,k_B\,T}{\varepsilon_0}}.$$

The ion front velocity and the ion front position can now be obtained by integrating $\frac{dv_{front}}{dt}=\frac{Z\,e\,E_{front}}{m_i}$ and $\frac{dx_{front}}{dt}=v_{front}$ which yields the following:

$$v_{front}\approx 2c_s\ln\left(\tau+\sqrt{\tau^2+1}\right) \tag{2.17}$$

$$x_{front}\approx 2\sqrt{2\,e_{math}}\;\lambda_{D0}\left(\tau\ln\left(\tau+\sqrt{\tau^2+1}\right)-\sqrt{\tau^2+1}+1\right) \tag{2.18}$$

where τ is

$$\tau=\frac{\omega_{pi}\,t}{\sqrt{2\,e_{math}}},$$

c_s is the ion acoustic velocity

$$c_s = \sqrt{\frac{Z k_B T_e}{m_i}}$$

and λ_{D0} is the initial Debye length with

$$\lambda_{D0} = \sqrt{\frac{\varepsilon_0 k_B T_e}{n_{e0} e^2}} .$$

Not only the temporal evolution of the ion front but also the evolution of the whole electric field is of interest. Following the analysis of particle-in-cell (PIC) and magnetohydrodynamic (MHD) simulations* from [23] the spatial distribution of the electric field at a definite time can be divided into an inner and an outer part: an inner electric field which is a plateau region followed by an exponential rise up to the ion front, and an outer field decaying as $(1+x/l_s)^{-1}$ where l_s is the field scale length. Fig. 2.4 shows a sketch of this field. According to [23], the plateau region decays as $(1+t/\tau_s)^{-2}$ while the peak of the electric field decays as $(1+t/\tau_s)^{-1}$, where τ_s denotes the decay time of the electric field.

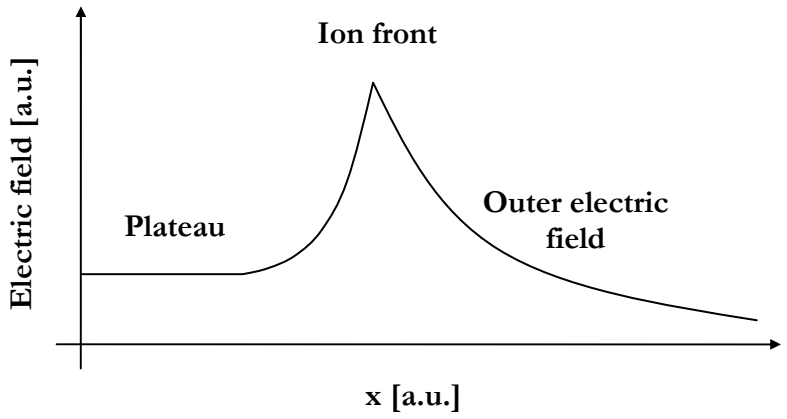

Fig. 2.4: Schematic spatial distribution of the electric field.

* PIC simulations track individual fluid elements in phase space while plasma parameters are calculated on stationary grid nodes. MHD simulations aim at solving the equations describing the plasma as an electrically conducting fluid.

An illustration of the complete temporal and spatial evolution of a typical electric field is depicted in Fig. 2.5.

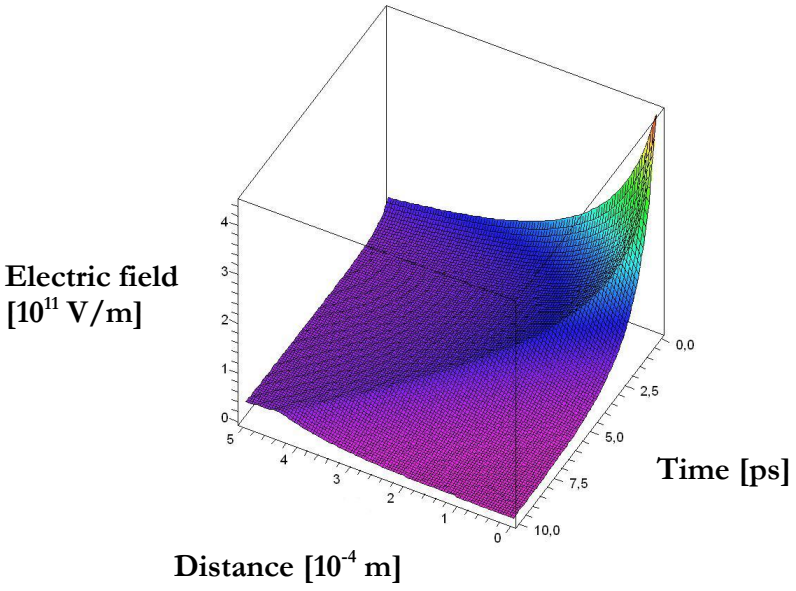

Fig. 2.5: Typical spatial and temporal electric field evolution in an ion accelerating plasma expansion.

The one dimensional model needs to be generalised to three dimensions to be applied to a real experiment. Figs. 2.6 and 2.7 illustrate the procedure.

Let us consider a plane target that lies in the y-z-plane of a Cartesian coordinate system. Let the centre of the interaction be at y = 0 and z = 0. An electron population is assumed to be formed on the target surface. The electron density distribution is usually assumed to be Gaussian. The electrons spread over the surface with a certain velocity. The onset of the expansion at a point (y, z) on the target surface is defined by the distance to the centre of the interaction. The expansion is supposed to start as soon as the electrons reach the point. At each point (y, z) the electric field from the one dimensional model is applied along the x-axis. It is calculated based on the local electron density. Since the electron density decreases with increasing distance from the centre of interaction, the electric field decreases as well. Fig. 2.6 B illustrates the construction of the electric field.

If the target is not plain, the electrons are again assumed to spread over the surface with a certain velocity and to form a defined density distribution on the target surface. In this case, however, the electric field is not applied to the x-axis, but to straight lines normal to the target surface. Fig. 2.7 shows a comparison between a plain and a cylindrical or spherical target.

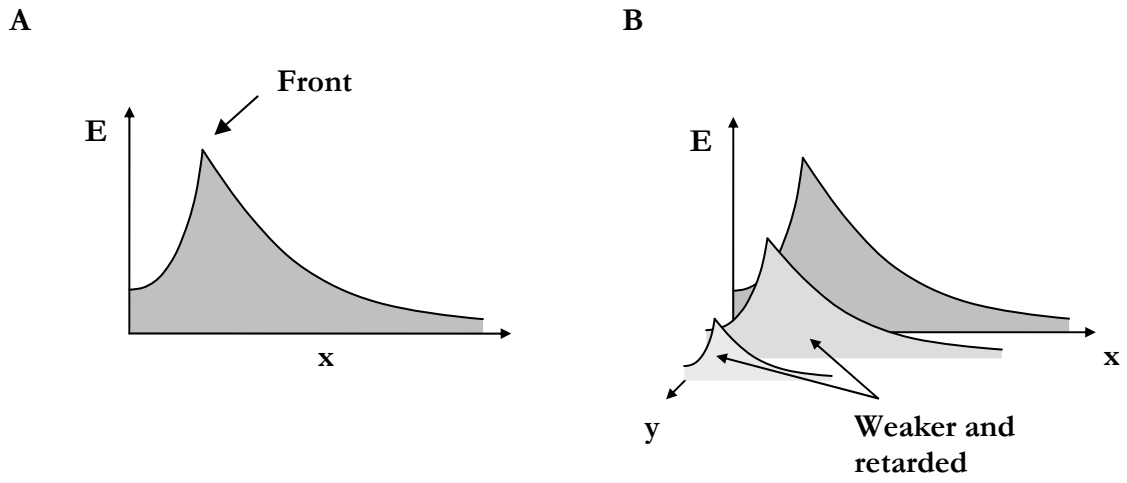

Fig. 2.6 A: The one dimensional electric field distribution. B: Generalisation to two dimensions: The larger the distance to the centre of the interaction, the weaker and the more retarded the electric field is assumed to be.

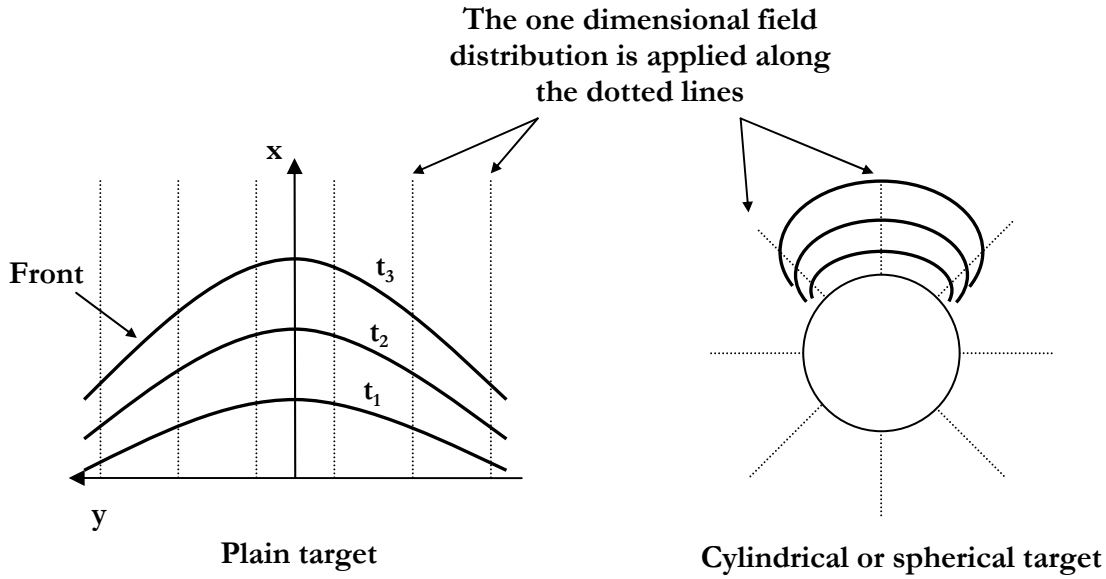

Fig. 2.7: Applying the one dimensional electric field distribution to a plane and to a curved target: The electric field is applied along the dotted lines. The thick curves show the ion front position at three different times.

This procedure provides an easy way to construct electric field scenarios that can be implemented in simulations. However, there are some limitations to this method. It is not applicable to every target geometry. In the interior of a laser-irradiated metal foil cylinder e.g., the field lines would converge and meet in the symmetry axis of the cylinder. The electric field along the field lines becomes unrealistic when the centre of the cylinder is approached. In Section 6.2, the electric field in the interior of a laser-irradiated metal foil cylinder is adopted from a one dimensional PIC simulation.

Violating the Lawson-Woodward theorem, breaking the Alfvén limit and accelerating protons even from targets that do not seem to contain hydrogen, laser ion acceleration incorporates processes that seem to be impossible at first sight. Nevertheless, even the simplified picture presented in this chapter is able to give a proper explanation. To understand all of the appealing properties of laser-accelerated ion beams, one needs to go further into detail though.

3 Particle beam properties

Laser-accelerated ion beams exhibit the shape of a cone whose axis of symmetry is normal to the non-irradiated rear surface of the target. The cone usually has an opening angle of about 30°. The energy spectrum depends on the emission angle: The highest energetic ions can only be found under small emission angles. If the target is not processed before use, an exponential energy spectrum with a sharp high energy cut off is observed (Fig. 3.1). The beam is quasi-neutral because low energy electrons co-move with the ions.

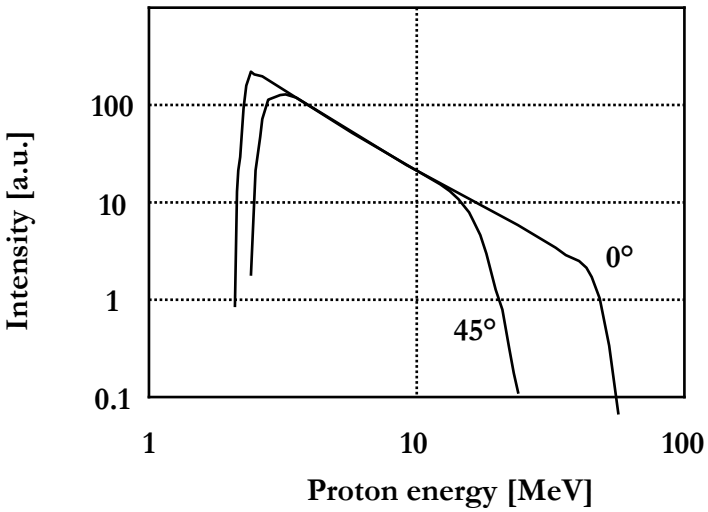

Fig. 3.1: Spectra of laser-accelerated protons (data taken from [2]). These data were recorded at the Nova Petawatt laser that was able to deliver 660 J in 440 fs [38], which is rather exceptional both in energy and power. Although the qualitative emission characteristics are typical for an ion acceleration experiment, one would not expect a strong emission under 45° in a usual experiment.

The emission geometry of the ions is depicted in Fig. 3.2. Taking a close look at the geometry, one can see that the apex of the emission cone is truncated since the emission zone on the target rear surface is spatially expanded. Nevertheless, one can imagine the ions to originate from a virtual source of only a few micrometres size situated in front of the target.

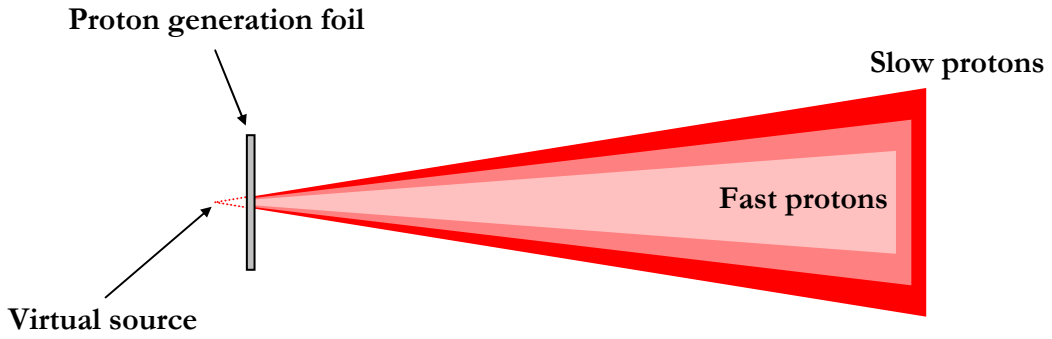

Fig. 3.2: Geometry of the ion acceleration process.

3.1 Emittance, divergence and spatial uniformity

Emittance, divergence and spatial uniformity are ion beam properties that are crucial for many applications: The low emittance of laser-accelerated particle beams will be beneficial for the design of ion injectors for conventional accelerators (cf. Section 4.2). Emittance restrains the focusability of the beam which is important for isochoric heating (cf. Section 4.1), inertial confinement fusion (cf. Section 4.3) and tumour therapy (cf. Section 4.4). Beam emittance limits the resolution of particle probing experiments, and spatial uniformity is of particular interest for proton radiography (cf. Section 5.2).

Emittance

A flow is called *laminar*, if adjacent fluid layers with different flow velocities move in parallel without mixing significantly [15]. It is useful to transfer this term to a particle beam, although a slight modification of the definition is needed. For a particle beam, one can distinguish between transverse and longitudinal laminarity [7], the former meaning that particle trajectories do not cross, the latter meaning that a class of particles having the velocity $v_1 \pm dv$ will never overtake another velocity class with $v_2 \pm dv$ (cf. Fig. 3.3). In fluid mechanics, a flow can either be laminar or not, there is no way of measuring the degree to which a flow is laminar. However, in classical particle accelerator physics this information is provided by the *emittance*, a low emittance indicating a high laminarity. Emittance is a measure for the phase space volume that is occupied by an ensemble of particles. In particle accelerator physics, it is useful to choose phase space

coordinates corresponding to angular and spatial deviations from an ideal particle trajectory instead of absolute position and momentum: if these deviations are small, one can apply linear approximation similar to the paraxial approximation in optics [40]. In phase space, such an ensemble can usually be enclosed in an ellipsoid or in an ellipse if projected to two dimensions (cf. Fig. 3.4). A well collimated or focussed beam exhibits only a small spread of deviations from the ideal particle path and thus corresponds to a small phase space volume. Please mind that a laminar divergent beam as depicted in Fig. 3.3 A also has a low emittance since the angular deviation (i.e. the angle between the actual and the ideal particle trajectory) depends linearly on the transverse particle position and thus, the phase ellipse degenerates to a line. Taking into account Liouville's theorem, one can tell that the volume of the ellipsoid is conserved if no non-linear process is applied. Thus, the emittance of the particle source restrains the possibility to collimate or to focus a beam.

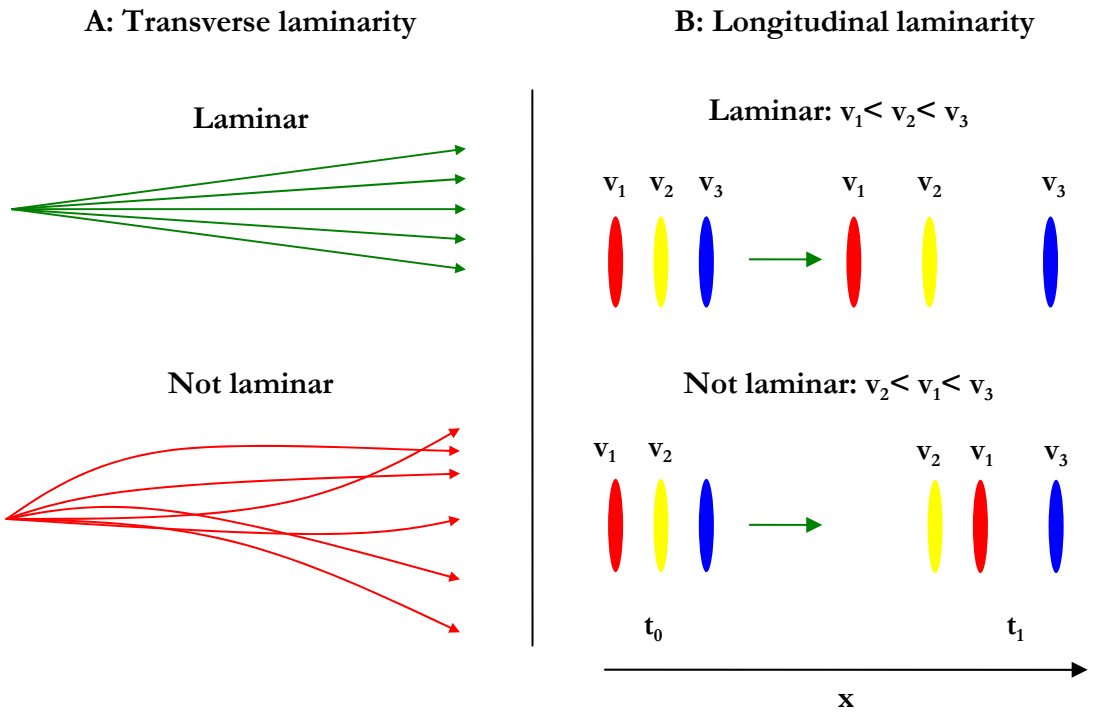

Fig. 3.3 A: The left side of Fig. 3.3 illustrates the transverse laminarity of a particle beam. In the upper drawing, the particle trajectories do not cross (laminar behaviour); in the lower drawing they do cross (non-laminar behaviour). B: The right side exemplifies longitudinal laminarity: Both the upper and the lower image show particle bunches from three different velocity classes (red, yellow, blue) at two different times t_0 (left) and t_1 (right). As indicated by the green arrows, the particles move towards the right side. In the upper image the three different velocity classes are ordered spatially with respect to their velocity at t_0: The fastest particles fly in front of the slower ones. That is why they maintain this order. In the lower image the three velocity classes are not ordered spatially: The slow yellow particle bunch flies in front of the faster red one at t_0. The red bunch overtakes the yellow one and the order of the velocity classes is not maintained at t_1.

To achieve a low emittance, ion acceleration via TNSA mechanism has a great advantage compared to other high energy ion sources: The ions at the rear surface of the target are initially cold. The transverse emittance of laser-accelerated protons could be measured precisely by imprinting a structure to the ion beam already at the source [7]. On the surface of the rear side of a target, equally spaced grooves are micro-machined on the micrometre scale. These grooves are imprinted into the density distribution of the proton beam, thus serving as fiducial marks; the density distribution of the divergent beam shows a magnified image of the target surface. The experiment yielded an almost exactly linear correlation between spatial and angular deviation. This indicates that the electron sheath has a nearly Gaussian density distribution [41]. The magnification of the target surface does not vary with the proton energy. As illustrated in Fig. 3.2, all protons appear to originate from the same virtual source. The transverse emittance is estimated to be <0.004 mm · mrad for 10 MeV protons which is 100 times lower than the typical emittance of a conventional accelerator.

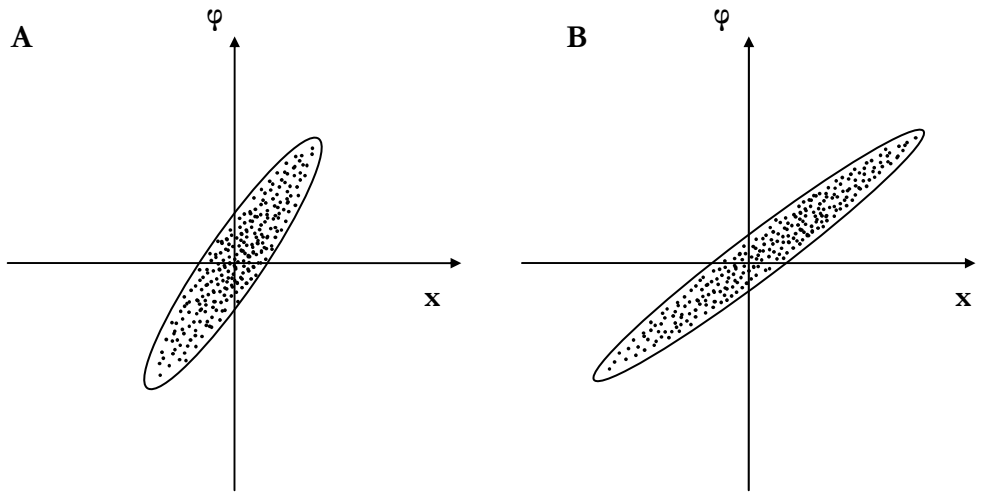

Fig. 3.4: Phase ellipses: x denotes the transversal distance from the ideal particle trajectory, φ denotes the angular deviation. The ellipses show the correlation between spatial and angular deviation. A phase space distribution as depicted in 3.4 A turns into a distribution as depicted in 3.4 B after the particles have drifted for some time. Although the tilt of the ellipse increases, the area enclosed is conserved.

The longitudinal emittance is also supposed to be very low since the acceleration time is thought to be extremely short (below 10 ps). Furthermore, there is some evidence that the protons might be emitted temporally ordered with respect to their energy, i.e. that the fasted protons are emitted at first and the slower ones afterwards [42].

Spatial uniformity

At first sight, the fact that laser-accelerated ion beams are divergent seems to be inconsistent with the model presented in Section 2.2: Target *Normal* Sheath Acceleration should not lead to different emission angles. But actually, the electric field is only normal to the target directly at the target surface. As described in Section 2.3, the acceleration takes place during the expansion of the plasma into vacuum. As soon as the ions leave the target surface, they are affected by an electric field whose divergence is governed by the Gaussian shape of the density distribution of the electron sheath (cf. Fig. 3.5).

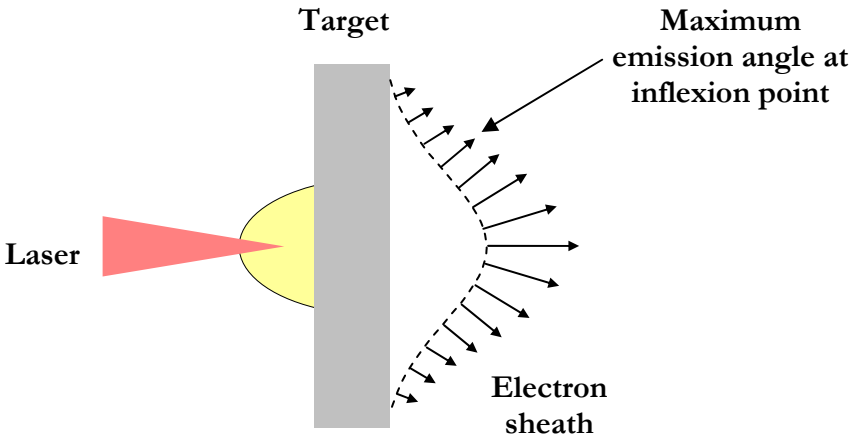

Fig. 3.5: Illustration of the electron sheath formation on the rear side of the target. The inflexion point of the Gaussian distribution defines the maximum emission angle which in turn corresponds to the boundary of the particle beam (adopted from [43]).

Laser-accelerated proton beams show a high spatial uniformity and a sharp boundary [41]: Inside the emission cone, the particle density does not depend significantly on the emission angle and there is a rapid decrease in density to the outside of the cone where no particles are emitted. This again can be explained by the Gaussian density distribution of the electron sheath (cf. Fig. 3.5). There is a maximum emission angle induced by the inflexion points in the bell shape of the electron distribution [43].

Experimental requirements

It has now become clear that laminarity and spatial uniformity of the ion beam depend on the integrity of the rear side of the target and of the formation of a smooth Gaussian-shaped electron

density distribution of hot electrons. Thus, one needs to take some experimental precautions to achieve a high beam quality:

- If the laser prepulse (cf. Section 5.1) launches a shock wave that propagates through the target, the acceleration must take place before the shock wave reaches the rear surface [44]. If an intense prepulse cannot be avoided, a thick target can be used. Then, the shock wave is still propagating through the target when the electrons are accelerated by the main pulse. The latter have time to overtake the shock wave.

- It could be shown experimentally that the intensity distribution of the laser focus on the target is reproduced by the electrons on the rear side and thus, it is imprinted into the density distribution of the ion beam [41, 45]. An at least approximately Gaussian-shaped laser focus is a precondition to obtain a uniform ion beam.

- Instabilities in the electron transport need to be avoided by the choice of target material [41, 46]. Usually, metals yield better results than insulators, high atomic mass ("high Z") material is superior to low atomic mass material.

- If heating the rear surface of the target cannot be avoided, one needs to consider the influence on ion beam parameters through the formation of a plasma gradient on the rear side [47]. This is of importance for the fast ignitor scheme in inertial confinement fusion (cf. Section 4.3).

Focussing

Controlling the beam divergence and in particular focussing could be achieved by different means. Patel et al. [48] used hemispherical shell targets to focus a proton beam as depicted in Fig. 3.6. The aluminium shell target had a diameter of 320 μm and a thickness of 10 μm. It was irradiated on the outer (the concave) side. A 100 fs laser pulse irradiated an area with a diameter of 50 μm with an average intensity of $5 \cdot 10^{18}$ W/cm^2. The inside of the shell imposed a concave shape to the electron sheath and thus, the protons were emitted in a convergent beam. This proton beam was focussed onto a plane 10 μm Al-foil. The heat pattern and the plasma on the rear side of the secondary target both had a diameter of about 50 μm.

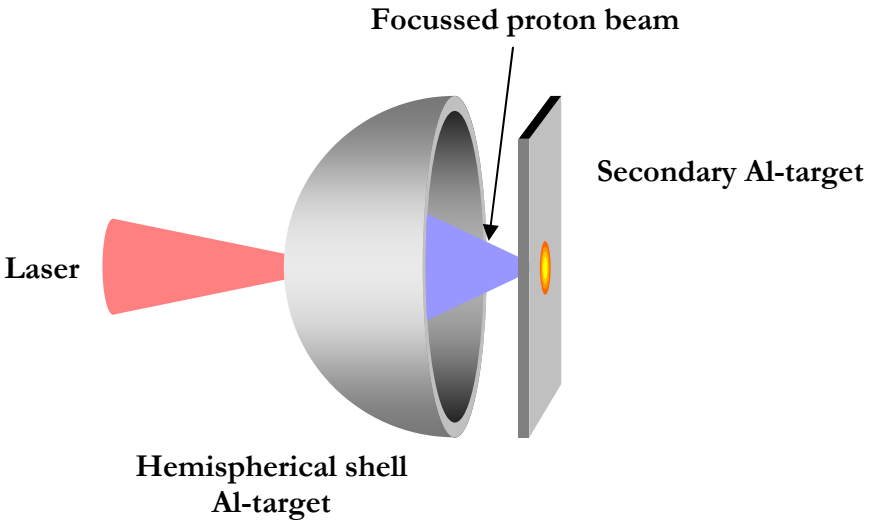

Fig. 3.6: Heating a secondary target with a focussed proton beam from a primary hemispherical shell target as described in [48] and [49].

The disadvantage of this method is the small focal length which is of the order of the shell radius. This makes it difficult to diagnose processes at the secondary target and restrains the design of experiments. This problem could be solved by Toncian et al. [50] by separating acceleration from focussing to the price of a more complex experimental setup (cf. Fig. 3.7).

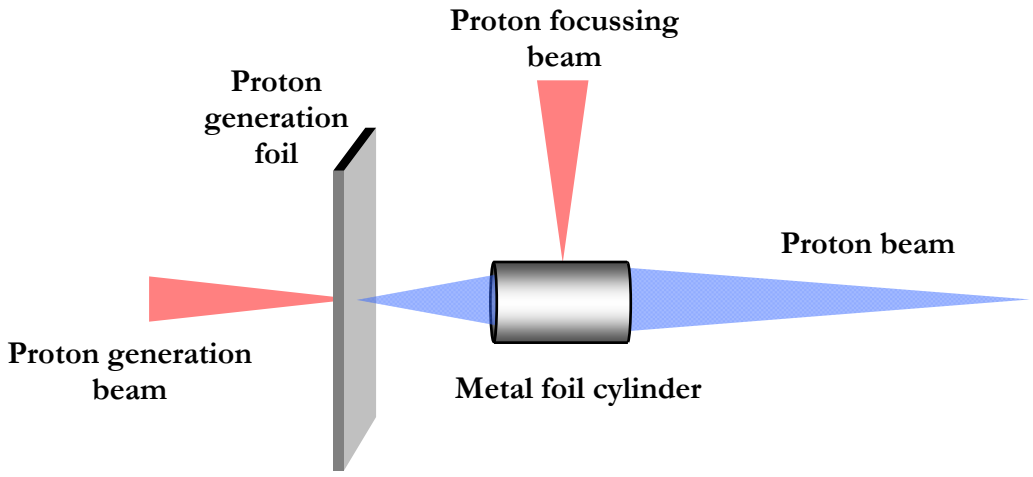

Fig. 3.7: Focussing of laser-accelerated protons using the electric fields in a laser plasma: The protons are accelerated at a plane foil target. As a secondary target, a hollow metal foil cylinder is used. A second laser pulse irradiates the cylinder while the accelerated protons are passing through. The proton beam is focussed by the electric fields in the plasma expanding in the interior of the cylinder.

The setup is composed of a standard proton acceleration experiment using a plain laser-irradiated foil target and a secondary target that is irradiated by another laser pulse that is synchronised to the first one. The secondary target is a hollow metal foil cylinder whose dimensions are of the order of a millimetre. The conical proton beam originating from the rear side of the first target passes through the interior of the second target. At the time when the protons are located inside the hollow cylinder, the second laser pulse hits the outside of the cylinder. Hot electrons spread over the inner surface of the cylinder and induce a plasma expansion with a rotational symmetry. This plasma expansion is accompanied by transient radial electric fields that are able to focus the proton beam. Focal spot sizes of about 200 μm can be obtained [50]. This setup also provides an energy selection of the protons which will be discussed in Section 3.2. The concept is well established for protons; the possibility to focus carbon ions is investigated in the framework of this thesis and will be discussed in Section 6.2.

The cylinder cannot be reused – it is evaporated by the laser energy. This and the fact that it needs to be triggered by a laser synchronised to the proton generation laser make this method experimentally demanding. To overcome these difficulties, Schollmeier et al. used permanent quadrupole magnets in a way similar to the magnetic lenses used routinely in the ion optics of conventionally accelerated particles [51]. In this case, the challenge lies in the fact that the currents occurring in laser acceleration by far exceed those known from conventional accelerators. This problem can be mitigated if the distance between proton source and focussing device is increased. Since the protons show a broad energy spectrum the proton bunch is dispersed while propagating and thus the current decreases. Schollmeier et al. used compact permanent magnets originally developed for laser-accelerated electrons that provide field gradients of 500 T/m [52]. With their setup, they were able to focus 14 MeV protons down to a spot of 286 μm × 173 μm at a distance of 50 cm to the proton source. Fig. 3.8 shows a schematic of this experiment. The proton beam originating from the rear side of a plane copper foil target passes through a hole in a radiochromic film detector that records the proton density distribution before the beam enters the magnet. The diluted and dispersed proton beam then passes through the small aperture (5 mm) of the first magnet which focuses the beam in one direction but defocuses in the other direction. The second magnet then provides the focussing in the direction defocused by the first magnet. Most of the defocused beam is cut at the second aperture. In the end, the transmission of the magnets was only about 0.1%. This might be improved by reducing the distance between the magnets. Since the magnets were not especially designed for this experiment, further progress in this concept is to be expected.

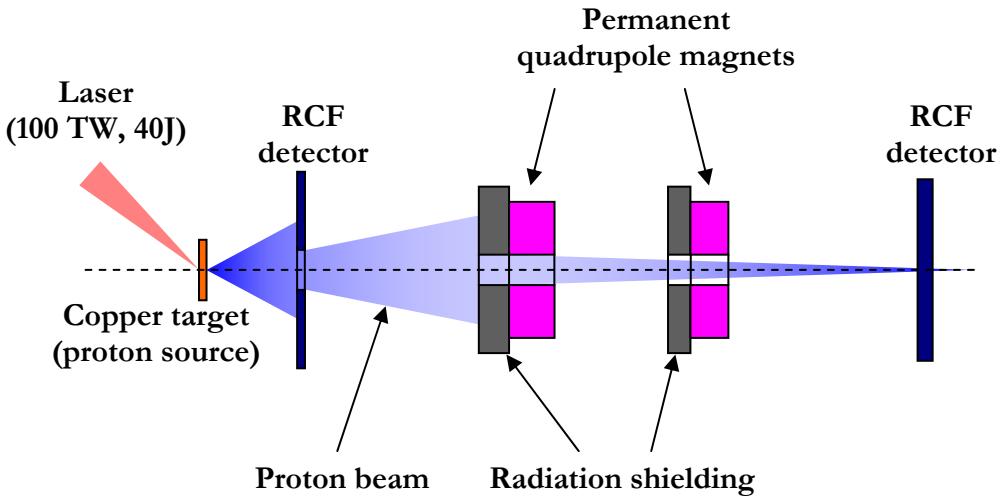

Fig. 3.8: Focussing laser-accelerated protons using two quadrupole magnets [51].

3.2 Energy spectrum and ion species

The exponential energy spectrum with its sharp high energy cut-off is both a blessing and a curse for laser-accelerated ion research. For some applications like proton probing (cf. Section 5.2), a broad energy spectrum can be favourable, for others like tumour therapy (cf. Section 4.4) a reproducible monoenergetic spectrum is a *sine qua non* condition. For some applications like inertial confinement fusion or isochoric heating, even a special shape of the energy spectrum can be advantageous.

The shape of the energy spectrum is a rather qualitative question, but some applications also ask for quantity: What is the maximum particle energy we can expect to achieve in the near future? Cancer therapy for example requires a proton energy of 50 MeV to 200 MeV. This region could hardly be attained so far. That is why we need to know how the particle energy scales with laser and target properties using the well-known TNSA mechanism, and we need to discuss new acceleration mechanisms.

In many experiments, shaping the energy spectrum is connected to the selection of an ion species. Ways to generate beams of a desired ion species are presented and interrelations with the shaping of the energy spectrum are pointed out.

Ion species

To accelerate ions of a desired species one needs to get rid of the protons first. Since protons have the highest charge-to-mass ratio of all ions and a low ionisation energy, they are accelerated most easily by the quasi-electrostatic field and screen other ions from the acceleration field. Thus, in the presence of the contaminant protons, the acceleration of other ions is widely suppressed.

Hegelich et al. successfully removed the contaminant hydrogen by passing a current through a heat resistant target (*ohmic heating*) [65]. 50 µm Tungsten foil targets coated with a 0.3 µm layer of CaF_2 were heated to temperatures of 1200 K. Figure 3.9 shows the F^{7+} spectrum of a heated target compared to the one of an unheated target.

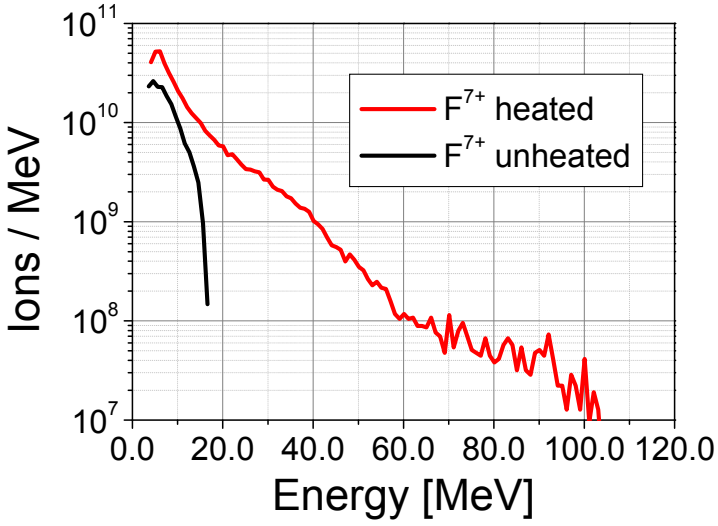

Fig. 3.9: Comparison between a heated and an unprocessed tungsten target coated with CaF_2: Using resistive heating, a significant increase in F^{7+} ion number and energy can be achieved (from [65]).

This method obviously cannot be applied if the target cannot withstand high temperatures or if the layer that is to be removed is not affected by heating. For example, many metal targets form a layer of oxides on their surface. To remove this kind of unwanted atoms the use of an ablation laser was investigated [27]. A 150 ps laser irradiated the rear side of the target with an intensity of about 10^{10} W/cm^2 removing the surface layer. The ablation laser pulse needs to be timed in a way that it cleans the target right before the acceleration laser pulse irradiates the target, so that the ablated material has enough time to leave the interaction zone but recontamination from the interior of the target chamber is avoided. In [66] the authors describe an efficient suppression of protons and a reduction of oxygen and carbon ions using this method.

In Section 6.2, target heating using a continuous wave laser will be presented along with experimental results. This method is not to be confused with laser ablation. In laser ablation, a *surface layer* of the laser-irradiated target *is removed*. Laser heating is applied at lower intensities, but the target is irradiated for minutes. In this case, *contaminants are desorbed*. Laser heating is equivalent to ohmic heating.

Energy selection

There are different ways to create quasi-monoenergetic ion beams. One possibility is the selection of a defined velocity class of particles from an originally broad energy spectrum. An experimental implementation of this idea was already presented in Section 3.1. The use of a hollow metal foil cylinder as a focussing device can also provide an energy selection: The accelerated proton bunch disperses while propagating; the fastest protons are the first to arrive at the cylinder, the slower ones follow temporally ordered with respect to their velocity. When the second laser hits the cylinder and induces the plasma expansion and its transient focussing fields inside the cylinder, only a definite velocity class of protons is affected. Protons of a certain energy can be chosen by setting the delay between the incidence of the first and the second laser. This delay corresponds to the time of flight of the chosen protons from their source to the cylinder. Precisely speaking, the delay needs to be set with respect to the exit of the cylinder [50]; those protons that are just about to leave the cylinder are the ones that are focussed. If we now introduce an aperture at the focal length, we can select the desired energy class of protons and block most of the other particles.

Energy selection also works with a focussing pair of miniature quadrupole magnets as described in Section 3.1. In this case, it is not possible to use the time of flight to distinguish different energies since the focussing field is constant. But actually, every proton energy corresponds to a different focal length [51]. To select a certain energy, one just needs to place an aperture at the focal length of this energy.

Selecting a desired particle energy by focussing could only be shown for laser-accelerated protons so far. The possibility to influence the energy spectrum of carbon ions in a comparable way will be discussed in Section 6.2.

Limitation of the acceleration zone

Other experimental ways to achieve quasi-monoenergetic ion beams aim at influencing the ion acceleration process itself. If the target can be prepared in such way that the spectrum of the accelerated particles is monoenergetic right from the beginning, there is no need to cut parts of the spectrum and thus all particles accelerated can be used.

The cause of the broad energy spectrum is the fact that accelerated ions are affected by different electric fields. The ions originating from edge of the emission zone on the rear side of the target are affected by a weaker electric field than those originating from the centre of the zone (cf. Fig. 2.3). Furthermore, the contamination layer has a certain thickness. Thus, ions buried under the surface and those originating directly from the surface are not accelerated equally.

To obtain a monoenergetic spectrum, one can now reduce the area from which particles are accelerated. This was already proposed in 2002 by Esirkepov et al. [53]: They recommended the use of double-layer targets. The first layer was supposed to consist of high-Z material and the second layer of low-Z material. The first layer was supposed to be a thick layer that was irradiated by the laser, whereas the other layer was supposed to be a thin coating on the rear side. The ions, of course, were supposed to originate from the thin layer only. (Please remember that the acceleration process favours ions with a high charge-to-mass ratio. At the same ionisation stage, the charge-to-mass ratio of a light ion is higher than the one of a heavier ion. Thus, lighter ions are accelerated more easily.) Target designs similar to the one proposed by Esirkepov et al. were implemented in experiments by Hegelich et al. and Schwoerer et al. [54, 55]. The former used thin palladium foils as targets and heated them to 1100 K by passing a current through them. As discussed above, hydrogen contaminants are desorbed from the target material at this temperature. From the hydrocarbon contaminants on the surface, a thin carbon layer on monolayer scale is formed. The authors attribute the formation of this layer to catalytic processes on the palladium surface. The target was irradiated with a 20 TW, 800 fs laser. Quasi-monoenergetic spectra of C^{5+} were obtained. An energy spread of 17% at an energy of about 3 MeV per nucleon was measured. The result cannot be explained by the work of Esirkepov et al. since the latter assume transverse limitation of the target as well. In hybrid code* simulations the experimental results could be reproduced though.

In this thesis, results reproducing the data of this experiment are presented. These results were obtained without the use of catalytic material. This will be discussed in Section 6.2.

* In this context, a hybrid code is a plasma simulation program treating the plasma both as a fluid and as an ensemble of particles.

To limit the emission zone transversely as suggested in [53], Schwoerer et al. used micro-structured targets: They coated thin (5 µm) titanium foils with a 500 nm layer of polymethyl methacrylate (PMMA). This layer was then partially ablated leaving 20 µm × 20 µm dots of PMMA behind. PMMA contains a large amount of protons (molecular formula: $(C_5O_2H_8)_n$). The dotted side served as the rear side of the target. Contaminants were desorbed by a Nd:YAG laser irradiating the rear side of the target. The front side was irradiated by a 10 TW 80 fs laser – aligned in such way that the laser spot was exactly opposite to a PMMA dot. The size of the electron sheath exceeds the size of the PMMA dot. That is why protons are supposed to be accelerated only from the centre of the sheath where the electric field is approximately homogeneous (cf. Fig. 3.10). The protons were supposed to be accelerated evenly.

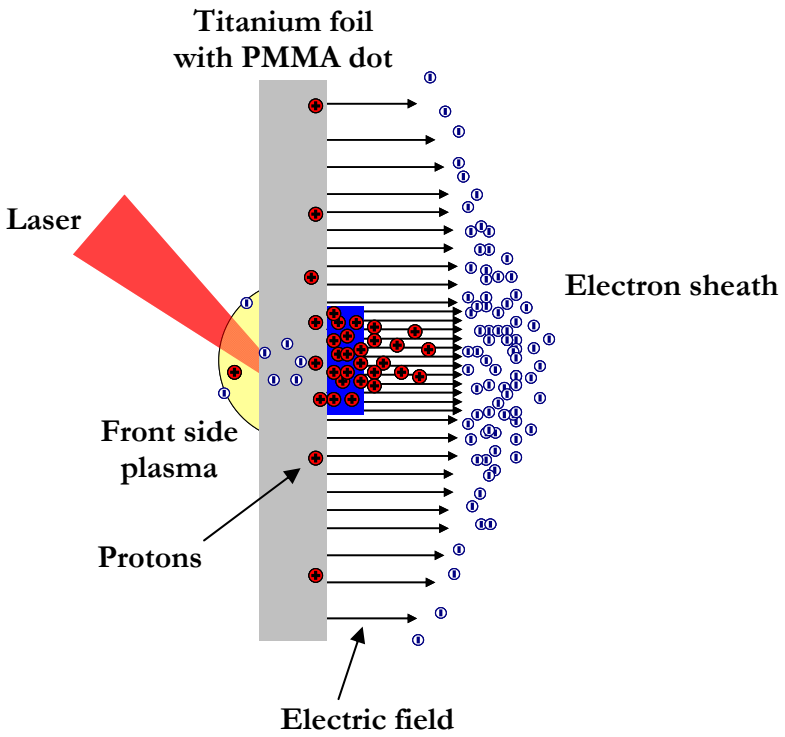

Fig. 3.10: Schematic of the acceleration of quasi-monoenergetic protons using a dotted target (according to [55]).

In the first proof-of-principle experiment, an energy spread of 25 % at 1.2 MeV was achieved with this method. By improving the micro-structured targets, the energy spread could be reduced to 10 % at an energy of 2 MeV [57]. Particle-in-cell simulations reproduced well the measured energy spectrum. But please mind that the dots used in this experiment are thick (500 nm)

compared to the region protons are accelerated from, the latter being only of the thickness of a few nanometres. Thus, there is no longitudinal limitation of the acceleration zone. In the standard experiment with a simple plane foil, protons coming from the central region of the acceleration zone show the well-known exponential spectrum with a high energy cut-off. It is not obvious how they are affected, if the transverse size of the acceleration region is reduced. Advanced theoretical considerations are presented in [56] arguing that the dot thickness is not necessarily a crucial parameter.

In the appendix of this thesis, the production of targets with thin dots is presented. These could be used in future experiments to investigate the dependence of the acceleration process on the layer thickness.

Droplet targets

Another possibility to create quasi-monoenergetic ions is the use of small spherical targets as described by Ter-Avetisyan et al. [58] and Brantov et al. [59]. The authors used a commercial nozzle system ejecting a water jet that decomposes into droplets of approximately 20 μm diameter. This system was also used in experiments conducted in the framework of this thesis and will therefore be described more thoroughly in Section 7.2. Both heavy water and normal water droplets were used. These droplets were irradiated by a 40 fs 750 mJ Ti:sapphire laser. When the prepulse was reduced to a certain level (a contrast ratio of 10^{8*}) to prevent the target from being perturbed before the incidence of the main pulse, quasi-monoenergetic peaks could be observed both in deuterium and proton spectra. In the case of deuterium an energy of 2 MeV with an energy spread of 15 % was achieved. The size of the targets automatically limits the acceleration zone in transverse direction. According to [59] the formation of a quasi-monoenergetic peak can be explained by the separation of ion species: The lighter ions (in this case hydrogen) form a bunch in front of the heavier ions (in this case oxygen). The heavy ions push the light ions into the forward direction and thus, the velocity of the light ions is defined by the maximum velocity of the heavy ions. The model explains the experimental observation that the deuterium energy was about twice the proton energy meaning that their velocity was the same. But actually, there were no oxygen ions observed at the expected energies, which would be crucial to support this theory. The appeal of the model originates from its applicability to heterogeneous targets; e.g., it easily explains the observation of quasi-monoenergetic ions from dotted targets.

* For an explanation of prepulse and contrast ratio, see Section 5.1.

Since the target has a spherical shape and the influence of the prepulse can be considered to be low, one would expect the electron sheath to cover the whole surface of the droplet and the particle emission to be isotropic. However, this is not the case: As in the case of a plane foil target the particles are accelerated into the forward direction. Using an advanced pump probe technique, the interaction processes will be investigated in Section 7.2.

Table 3.1 provides an overview on the experiments described above.

Table 3.1: Overview on experiments concerning the selection of ion species and the shaping of the energy spectrum.

Author	Ref.	Method	Focus-sing	Protons	Deute-rons	Carbon ions	Fluorine ions	Mono-energ.
Hegelich et al.	**[65]**	CaF_2 layer, ohmic heating					✓	
Toncian et al.	**[50]**	Laser-irradiated cylinder	✓	✓				✓
Schollmeier et al.	**[51]**	Quadrupole magnets	✓	✓				✓
Hegelich et al.	**[54]**	Heating, C-layer on Pd-foil				✓		✓
Schwoerer et al.	**[55]**	PMMA dots		✓				✓
Ter-Avetisyan/ Brantov et al.	**[58, 59]**	Water droplets		✓	✓			✓

Energy scaling

Knowledge on energy scaling is crucial to transfer today's experimental results to future applications. On the one hand, the influence of changes in laser parameters (like intensity increase or prolongation of pulse duration) needs to be considered. On the other hand, target properties like thickness, shape or mass need to be evaluated. In the first case, it is quite hard to predict the effect of new laser parameters on particle energy spectra exactly, even if well-known acceleration mechanisms are assumed to stay dominant. In the second case, lots of different

targets are conceivable, but fabrication and experimental implementation of exotic targets can be quite demanding.

In [34] energy scaling is presented based on the one dimensional model described in Section 2.3, assuming that acceleration time is limited (this is not included in the model, but it is necessary to introduce a limitation since the isothermal model predicts infinite acceleration). The model is compared to various experimental results. Fig. 3.11 shows the dependence of the maximum proton energy on the laser pulse duration and the laser intensity and the dependence of the number of particles per MeV on $I \cdot \lambda^2$ (I being the laser intensity and λ the laser wavelength).

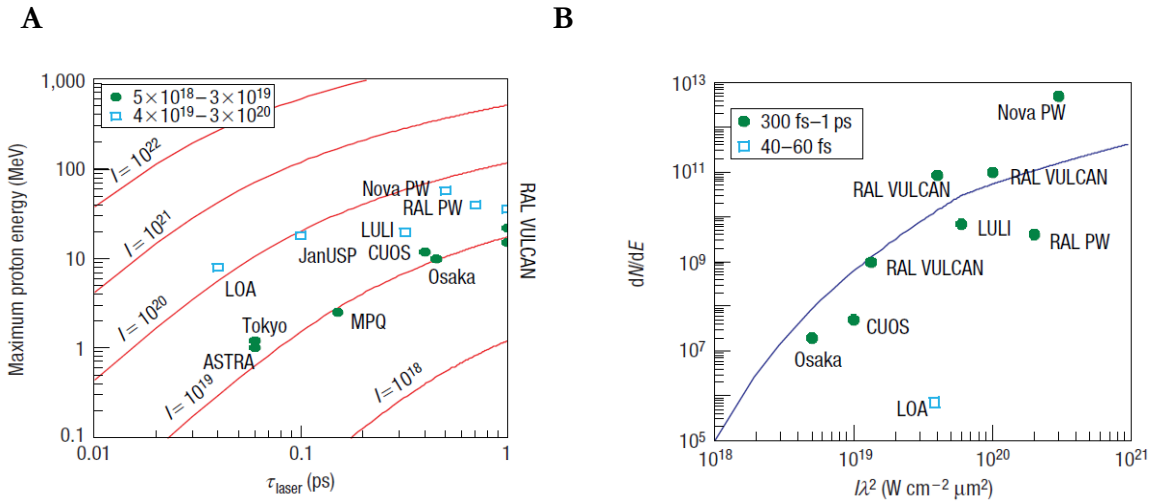

Fig. 3.11 A: Maximum proton energy against laser pulse duration. The red curves show the dependence for different laser intensities as calculated using the model. The blue squares and green dots mark experimental results from different laser facilities at two different intensity ranges. B: Number of particles per MeV (at 10 MeV) against $I \cdot \lambda^2$ (I being the laser intensity and λ the laser wavelength). The blue curve shows the modelled dependence, green and blue marks separate two different experimental pulse duration regimes. Both taken from [34], for references to individual experiments, see ibid.

The authors also provide energy scaling for the target thickness. At the beginning, the maximum proton energy increases when the target thickness is reduced, but if the thickness is reduced below a certain limit, the maximum energy conversely starts decreasing. This limit is set by the level of the prepulse that perturbs the target before the arrival of the main pulse. By enhancing the contrast ratio (the main-pulse-to-prepulse ratio) Ceccotti et al. were able to reduce this limit to a target thickness of 100 nm [26].

Recently, significant advances in maximum energy, particle number and laser-to-ion-energy coupling by the use of specially shaped mass-limited targets were reported in [60]. The nano-

fabricated targets consisted of a hollow cone with a small disk on its apex (cf. Fig. 3.12). The laser irradiates the interior of the cone. The cone serves as a guide for the hot electrons in a way that was already described by Kodama et al. [61]. Additionally, the cone prevents plasma from the front side from spreading around the edges of the small target and reaching the rear surface (an issue that will again be of importance in Section 6.1). The electrons are guided to the disk that is located on the apex of the cone and form a transversely limited sheath on the rear side. Guidance and confinement of the electrons led to a fourfold increase in laser-to-ion-energy conversion efficiency and a few times increase in maximum ion energy.

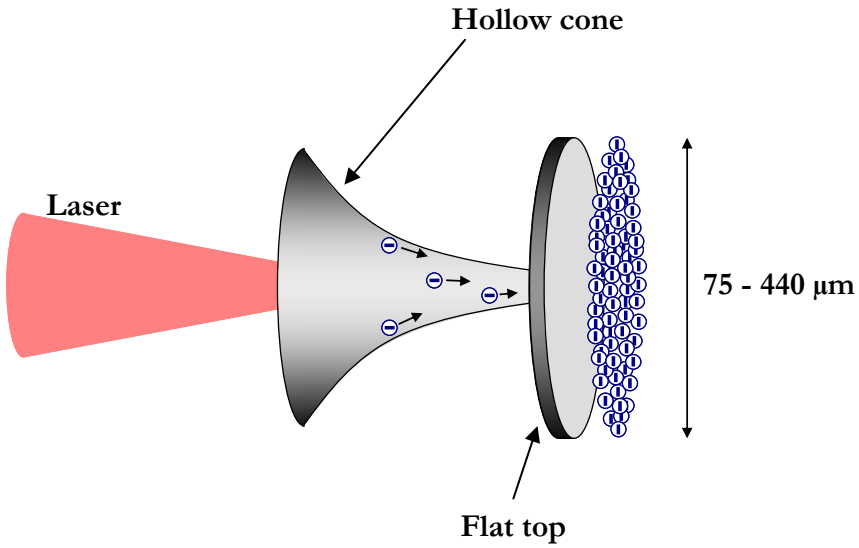

Fig. 3.12: Flat-top cone target experiment. The laser irradiates the interior of the hollow cone. The electrons heated by the laser are guided to the disk on the apex of the cone where they form a transversely limited sheath (according to [60]).

In this thesis, the possibility of improving ion beam properties by the use of mass-limited targets will be treated in Section 6.1 along with experimental results obtained.

New paths to energy and beam quality increase

For reasons of completeness, proposed future acceleration mechanisms will shortly be mentioned.

In 2004, Esirkepov et al. proposed an acceleration scheme in the *radiation pressure dominated* regime [62]: For extremely high laser intensities of about 10^{23} W/cm^2 the laser is able to push forward *all* the electrons located in the interaction zone causing the electrons to be completely separated

from the ions. Subsequently, the ion layer follows the electron layer. The laser is now reflected by the moving plasma surface which acts as a perfect plasma mirror. Therefore, the laser energy is transferred to the particles by the light pressure. This makes the mechanism extraordinary efficient. According to the authors, ion energies of up to 100 GeV per nucleon might be attained.

To reduce the intensity threshold for the entrance into the laser pressure dominated regime, the use of circularly polarised light is discussed. The circular polarisation inhibits electron forward acceleration by the oscillating light wave and thus suppresses the competing TNSA mechanism. For an introduction and recent theoretical results, please refer to [63].

Another scheme includes the use of a high contrast laser providing an intensity of about 10^{21} W/cm^2 and thin plain targets of about 30 nm thickness [64]. The scheme starts like the TNSA mechanism with the acceleration of electrons and a formation of an electron sheath on the rear side of the target. But then, electron recirculation and further heating takes place until the electrons are removed and the target becomes transparent to the laser. Now, the laser can interact directly with the electron sheath on the rear side and causes a second stage of acceleration. That is why the authors curiously named the process *laser break-out afterburner* (BOA). Carbon ion energies of up to 2 GeV are predicted.

4 Applications

This chapter provides an overview on the applications of laser-accelerated protons and heavier ions. An established application of laser-accelerated protons, the use of proton beams as a diagnostic tool, will not be described here but in Chapter 5 since this method was used to obtain experimental results presented in this thesis.

4.1 Isochoric heating

Isochoric heating (heating at constant volume) is a way to produce the so-called warm dense matter (WDM) – matter with approximately solid state density at temperatures of a few tens of eV. Occurring in the interior of giant planets or brown dwarfs, this state of matter plays an important role in astrophysics [72]. Furthermore, an object passes the state of WDM, if it is instantly heated to a high temperature. Despite of its importance, only little is known about its physical properties such as opacity and equation-of-state. The problem is that it is hard to produce a piece of matter at solid state density that is uniformly heated to more than 10^6 K. Attempts to produce WDM by volumetric heating using energy sources such as conventionally produced ion beams, x-rays or laser-driven shocks suffer from the heating time (10^{-9}-10^{-6} s) that is much longer than the typical expansion time (~10^{-12} s) [48]. Short pulse lasers provide a short heating time, but they cannot heat a large volume of matter uniformly, since they are unable to penetrate dense matter beyond the skin depth. Laser-accelerated protons however exhibit a short pulse duration in the order of picoseconds and favourable energy deposition properties. The characteristic energy deposition is depicted in Fig. 4.1.

The energy deposition curve shows an almost plateau-like region that is followed by a distinct peak near the end of the particle path – the so-called Bragg peak. The thickness of the heated target is chosen in such way that it completely lies in the plateau region for most of the laser-accelerated protons. That is why an almost uniform temperature can achieved.

Patel et al. [48] used the setup depicted in Fig. 3.6 – a hemispherical shell target for the generation of a convergent proton beam that is focussed onto a secondary Al foil target. They were able to heat an area of 50 μm in diameter to a temperature of 23 eV. More recently, a temperature of 81 eV was reported using a similar setup – with a higher laser energy though [73].

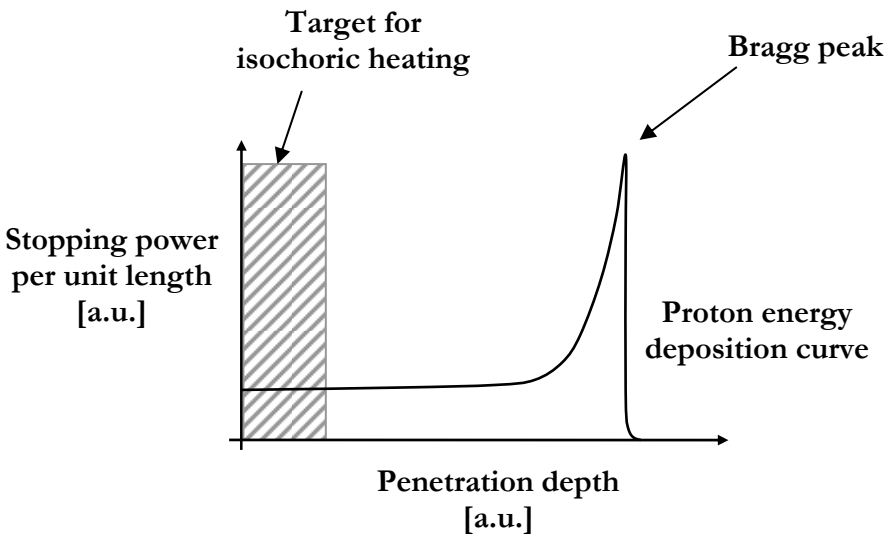

Fig. 4.1: Characteristic curve of the energy deposition of a proton in matter. The energy deposition curve shows a distinct peak (the Bragg peak) near the end of the particle path. For isochoric heating, the target thickness is chosen to ensure uniform energy deposition.

4.2 A new particle source for conventional accelerators

The low emittance of laser-generated proton beams could also be beneficial to conventional accelerators. To reduce the emittance of a conventional accelerator, laser acceleration could be used as a particle source instead of plasma discharges. Removing co-moving electrons without significantly increasing the emittance has been shown [7] and the suitability of a focussing system for the injection into a post-accelerator has been discussed [50, 51]. If no sufficient energy selection is applied, the compensation of the energy spread could be provided by coupling the beam to the field gradient of the post-accelerator [43]. Recently, a complete simulation of the injection of a laser-accelerated proton beam into a drift-tube linear accelerator was conducted [74], showing the feasibility of the scheme.

4.3 Proton-assisted fast ignition

One possible path to controlled nuclear fusion is *inertial confinement fusion* (ICF)[*]. A spherical target containing the deuterium-tritium fuel is irradiated homogenously to be compressed and heated to fusion conditions. Achieving these conditions throughout the volume of the compressed fuel (the so-called *volume ignition*) is far out of reach of today's technical possibilities. In the *hot-spot concept*, only a small area in the compressed target will attain fusion conditions. Once this spot ignites, the rest of the fuel will be burned subsequently. To reduce the energy requirements for the driver of the compression and to increase the over-all energy gain, it might be possible to separate compression from ignition. The main driver compresses the target and an additional beam triggers ignition in the core of the compressed target. This is the so-called *fast ignitor* (FI) concept [76]. Laser-accelerated protons are a candidate for such an ignition beam [77]. They are able to penetrate deeper into dense material than heavier ions and they suffer less from straggling and instabilities than electrons. Furthermore, most of the proton energy is deposited in the Bragg peak. This allows the localization of the heated area. Fig. 4.2 shows a schematic of a possible setup. High energy short pulse lasers irradiate a large area on the front side of a target that is shaped to focus the protons to the core of the compressed fuel.

However, proton-assisted fast ignition faces several problems [43, 78]. First of all, the focal spot size needs to be much smaller than the one achieved so far (cf. Section 3.1). On the one hand, irradiating a large area on the front side of the proton generation target flattens the electron sheath on the rear side – this might improve the focus. On the other hand, even a small deficiency in neutralisation of the proton beam would give rise to Coulomb forces hampering the formation of an emittance limited focus. Another point is that in the vicinity of the fusion target, the rear side of the proton generation target could suffer from being heated, but Fuchs et al. state that this would not influence the proton beam properties to a critical degree [47].

A narrow energy spectrum is not necessarily the best choice for protons used in the FI concept. Using a broad energy spectrum, the most energetic protons could start heating the target, increasing the penetration depth of the less energetic ones that follow. Thus, all protons could have their Bragg peak at the same place [78].

[*] For further reading on ICF, please refer to [75].

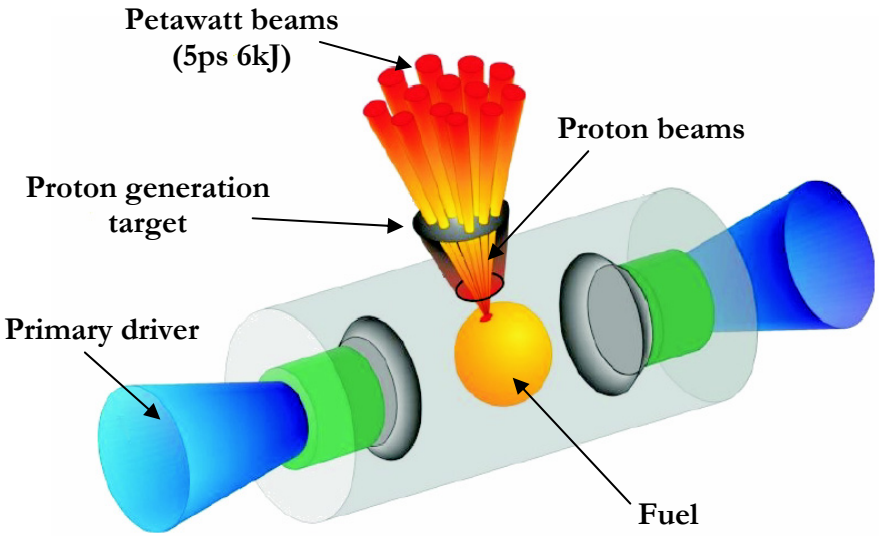

Fig. 4.2: Schematic of proton-assisted fast ignition. Laser beams irradiate target that is shaped to focus the protons into the core of the fuel (taken from [77]).

The energy required to be deposited in the fuel in a simple FI scheme is quite high – about 10 kJ. A concept using two proton beams was presented to reduce the energy requirement down to 8 kJ [79]. If only one of those beams has a uniform profile and the other one has an annular profile, even a reduction down to 6 kJ might be achieved [80].

4.4 Medical applications

In this section, examples of possible medical applications are given. These are some of the most appealing, but also some of the most demanding applications of laser ion acceleration.

Radio-isotope production for positron emission tomography

Positron emission tomography is a diagnostic method in medicine. A substance that is metabolised by tissue that needs to be located and investigated (e.g. a tumour) is marked with a radioactive tracer. This tracer emits positrons that are stopped in the tissue and combine with electrons. The annihilation yields two counter-propagating 511 keV photons. A ring of coincidence detectors is placed around the patient. If two photons are detected simultaneously, they can be assumed to originate from the annihilation process. Now that both of them are located, one can obtain their

flight path. Measuring many of these signals the radiation source can be reconstructed. The β^+ emitter needs to be short-lived to prevent the patient from being exposed to an unnecessarily high dose. Furthermore, it needs to be compatible to the carrier substance. The most popular isotope is ^{18}F but it is also possible to use ^{11}C. These isotopes are usually produced via (p, n) or (p, α) reactions using cyclotrons.

Experiments using laser-accelerated protons could demonstrate the production ^{18}F and ^{11}C [81, 82]. Ledingham et al. were even able to produce the marked carrier substance, thus showing that laser accelerators could be one day an alternative to conventional accelerators in the production of short-lived isotopes [83]. Nevertheless, the activity of ^{18}F and ^{11}C produced in this experiment was too low by a factor of a few thousands and one hundred, respectively. Furthermore, in this case the appeal of laser accelerators lies in the fact that they have potentially low costs of purchase and a compact design. The proof-of-principle experiment, however, needed to be performed at a large facility. Therefore, further progress in laser development and proton flux increase (using mass-limited targets, e.g.) will be needed to compete with conventional accelerators in isotope production.

Cancer therapy

In radiotherapy, a tumour located inside a patient is irradiated by ionising radiation. The dose deposited in the tumour causes the malignant tissue to die off. However, the most commonly used x-rays deposit their energy throughout the material they pass through, thus affecting sound tissue as well. On the contrary, ions deposit their energy mainly in the Bragg peak (cf. Section 4.1). In ion radiotherapy, the dose can be located much more precisely than in x-ray radiotherapy. By varying the energy of the ions the dose can be spread over a certain distance. Fig. 4.3 shows a diagram of the dose absorption for different types of radiation.

Most ion radiotherapy facilities use proton beams. Carbon ions offer several advantages like lower lateral straggling, higher biological effect and the possibility of in-vivo range localisation using positron emitting beam fragments [85]. However, due to the higher energy requirement for carbon beams, carbon ion radiotherapy facilities are more expensive than proton beam facilities.

The high cost is the main disadvantage of ion radiotherapy. The overall costs of a facility lie in the order of 100 million Euros. That is why only few facilities exist all over the world. Laser ion acceleration might offer a significant cost reduction in the future, thus allowing a wider use of ion radiotherapy. Although the costs of the accelerator itself amount only to 10-20 % of the facility [86], laser accelerators could also lead to the design of less expensive gantries [87]. The gantry is

the part of the facility that guides the beam to the patient. Today's ion radiotherapy facilities incorporate enormous rotatable machines (the gantry of the *Heidelberg Ion-Beam Therapy Center* HIT weighs 600 tons [84]) that consume the largest part of the budget. Guiding light requires less effort than guiding a highly energetic particle beam. That is why laser acceleration inside the treatment room is envisioned.

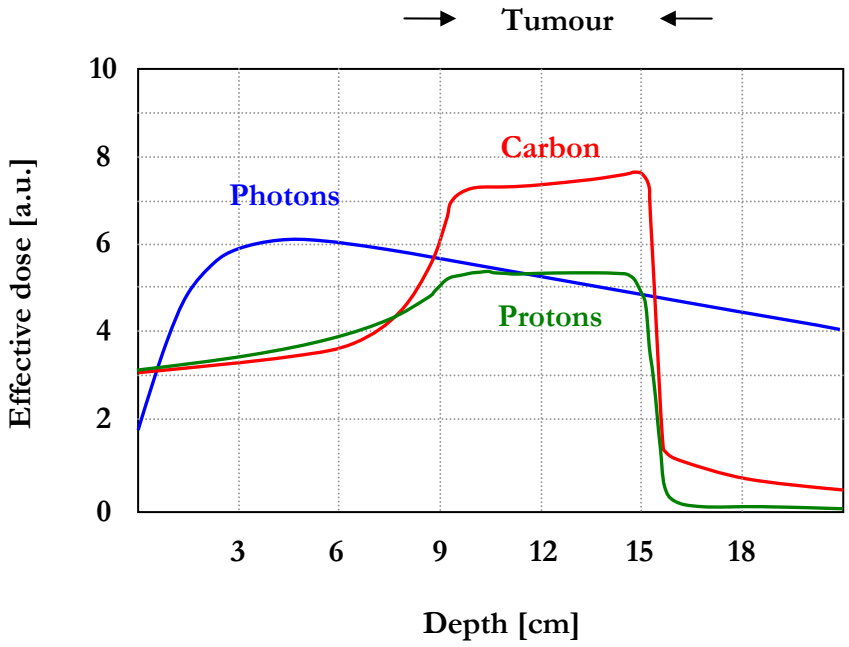

Fig.: 4.3: Biologically effective doses for x-rays (photons), protons and carbon ions (from [84]). The dose deposition of protons and carbon ions can be controlled by varying the particle energy over a defined range – the Bragg peak is shifted over the region where the tumour is located.

The beam parameter requirements for ion radiotherapy are extremely high: energy spread and shot-to-shot variation need to be in the order of a few percent, the beam needs to be well collimated, the dose needs to be controllable and the proton energy required ranges from 50 MeV for eye tumours to more than 200 MeV for deeper situated tumours. Carbon ion therapy even requires energies of up to 400 to 430 MeV per nucleon. Furthermore, high repetition lasers need to be developed. For an overview on beam requirements, please refer to [86].

5 Experimental methods

5.1 High power short pulse lasers

This section gives a short overview on the functional principle of the lasers that were used to conduct the experiments presented in this thesis. For a more detailed description, please refer to [88]. A short introduction can be found in [13]

Basic setup

Almost all high power short pulse lasers comprise the following parts:

- Oscillator: a laser system that provides high quality short pulses at a low energy and a high repetition rate
- Stretcher: an optical system that stretches the laser pulse in time
- Amplifier stages: a sequential system of light amplifiers
- Compressor: an optical system performing the inverse operation of the stretcher

The oscillator produces laser pulses that are a superposition of light modes. To obtain a pulse length in the order of femtoseconds, the spectral range of the waves that are superimposed needs to be extremely high: The minimum pulse length Δt_{min} is inversely proportional to the bandwidth $\Delta\nu$, since their relation is governed by the Fourier transform. Therefore, a material with a spectrally broad lasing transition is to be used. An ideal gain medium for the production of femtosecond laser pulses is titanium-doped aluminium oxide (Ti:sapphire). Ti:sapphire exhibits an emission spectrum ranging from 670 nm to more than 1100 nm with a maximum around 800 nm [89]. The superposition of the modes is achieved by mode-locking, a technique that is thoroughly described in [88].

The pulse leaves the oscillator with an energy of only a few nJ. To be amplified, it needs to be stretched at first. After having been amplified it is compressed again. This procedure – known as *chirped pulse amplification* (CPA) [90] – is necessary, because the optical components in the

amplifiers would not withstand the high intensity of the compressed amplified pulse. By stretching the pulse, the intensity is reduced.

The length of the light path through the stretcher depends on the wavelength. If a longer wavelength takes a longer way through the stretcher than a shorter one, the pulse duration is increased and the pulse leaves the stretcher with a spectral chirp, i.e. the colours of the pulse are spatially and temporally sorted. The most popular stretcher configuration is a pair of diffraction gratings.

At first, the stretched pulse usually enters a regenerative amplifier. The regenerative amplifier works like a normal laser cavity except for the fact that it is seeded by the laser pulse from the oscillator. It provides most of the amplification lifting the pulse energy to the mJ level. The pulse is coupled out of the cavity by a Pockels cell (a fast electro-optical switch). Subsequently, the pulse passes further amplification stages without cavity.

If Ti:sapphire crystals are used as gain medium in the amplifiers, the final energy of the pulse usually amounts to a few J at maximum. If higher energies need to be attained, neodymium-doped glass is used as gain medium. But this, of course, is to the price of a narrower bandwidth and thus a longer pulse duration. Nd:glass can be pumped with flash lamps. Compared to the frequency-doubled Nd:YAG lasers that are used to pump Ti:sapphire, flash lamps deliver a lot more energy. But since they have a broad spectrum, the Nd:glass gain material is unintentionally heated. The heat pattern in the gain medium changes its optical properties. This might cause unwanted effects like focussing, e.g. That is why a Nd:glass laser needs to cool down after every shot. In consequence, all experiments at Nd:glass lasers are single shot experiments.

After amplification, the pulse is recompressed. The compressor performs the inverse operation of the stretcher, but usually the original pulse duration cannot be achieved. One reason for this is the so-called *gain-narrowing*: The amplification process favours central wavelengths so that the central part of the pulse spectrum gains more energy than the wings. The spectrum becomes narrower and thus, the pulse length increases. Inevitable non-linear dispersion that cannot be compensated by the compressor is another factor that contributes to pulse lengthening.

Prepulse and contrast ratio

The short laser pulse is accompanied by a pedestal of a comparatively long duration. The radiation that precedes the pulse is often called *prepulse*. The prepulse mainly originates from:

- Pockels cell leakage: In the regenerative amplifier, the pulse runs to and fro while being amplified. In every cycle, the Pockels cell leaks a small part of the pulse that is emitted into the subsequent amplifier chain.

- Imperfections in the pulse spectrum: The spatial shape of the pulse is Gaussian only if the spectrum is Gaussian as well. If a real (non-Gaussian) spectrum is Fourier transformed, peaks can occur in the spatial distribution preceding the main pulse.

- Amplified spontaneous emission (ASE): In the gain material, a particular energy level is populated by the pump to induce a population inversion. This permits stimulated emission to take place, but it also causes spontaneous emission which is a result of the limited lifetime of the energy level. This incoherent emission is amplified by the amplifier chain before the main pulse arrives, taking advantage of the population inversion in the gain medium.

There are techniques to reduce the intensity of the prepulse (cf. [91], e.g.), but it cannot be avoided completely. As a measure for the degree to which the prepulse is suppressed, the *contrast ratio* is defined as the main-pulse-to-prepulse ratio.

Focussing optics

After having left the laser system itself, the laser pulse is guided into the target chamber where it is focussed onto the target by a parabolic mirror. The mirror is a cut-out of a whole paraboloid focussing the beam *off-axis* (cf. Fig. 5.1).

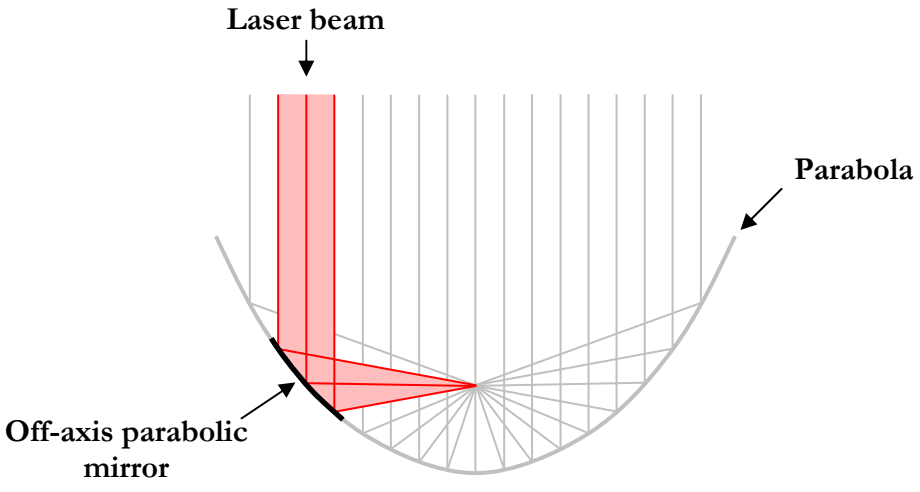

Fig. 5.1: The parabolic mirror is only a cut-out of a whole paraboloid. The beam is focussed off-axis.

This prevents the beam from being focussed back on its own path leaving the experimentalists enough space for their target support and diagnostics. The focal spot typically has a size of about 10 μm full width at half maximum.

Laser systems

Table 5.1 gives an overview on the laser systems used for the experiments presented in this thesis.

Table 5.1: Parameters of the laser systems used for experiments presented in this thesis.

Laser system	Laboratory	Type	λ [nm]	Energy [J]	τ [fs]	Power [TW]
Vulcan TAW	**Rutherford Appleton Laboratory**	**Nd:glass**	**1054**	**100**	**1000**	**100**
LULI 100 TW	**LULI, École Polytechnique**	**Nd:glass**	**1057**	**25-30**	**320**	**~100**
MBI Ti:Sa	**Max-Born-Institut Berlin**	**Ti:sapphire**	**800**	**~0.7**	**40**	**~20**
MBI Nd:glass	**Max-Born-Institut Berlin**	**Nd:glass**	**1053**	**7**	**1500**	**5**

5.2 Plasma diagnostics

Among the possible applications of laser-generated ions, the use of proton beams as a diagnostic tool is the most mature one. Although it is still a sophisticated technique that can be applied only in few laboratories, it has become an established method in the repertoire of a laser plasma physicist.

The technique was extensively used to obtain the results presented in this thesis. That is why it will be described in detail.

Proton radiography

The idea of proton radiography was developed already in the 1960s [67] – on the basis of conventional accelerators at that time. The technique was seen as an alternative to x-ray radiography which is (still today) used to image the interior of objects via point projection. Proton point projection images show a high contrast even if the imaged object is thin. The resolution of point projection with a light source is of course limited by the source size. Transferred to a particle beam the resolution is limited by its emittance or its virtual source size. That is why laser-accelerated low emittance proton beams provide significant advances in resolution. This opportunity was recognized only shortly after the discovery laser proton acceleration via TNSA [68]. Fig. 5.2 shows an example of a proton radiography experiment. This experiment will be described in detail in Section 7.2.

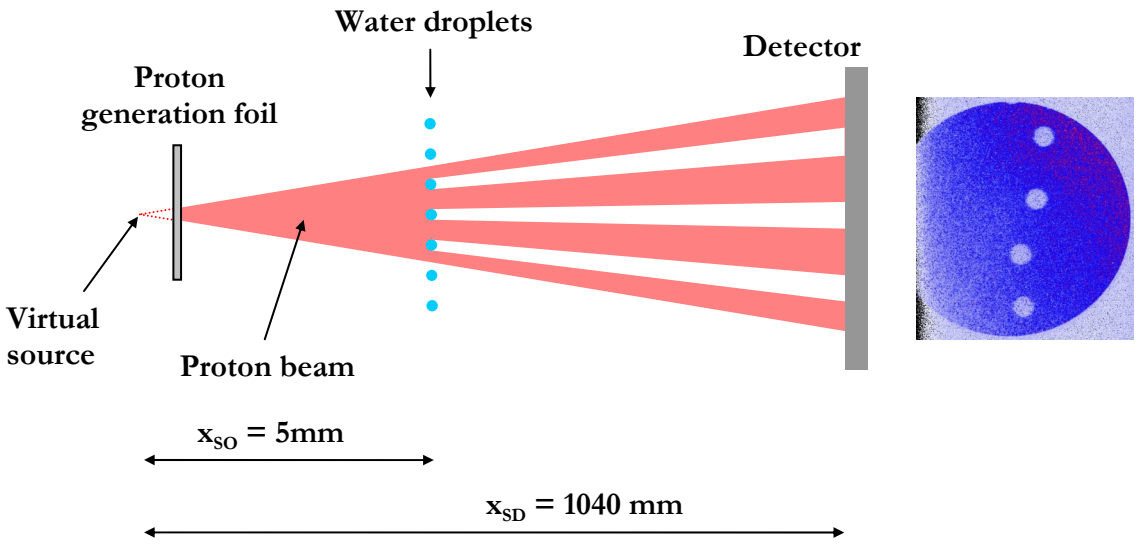

Fig. 5.2: Point projection using laser-accelerated protons. The highly laminar proton beam projects a shadow of the investigated object (a water droplet jet) onto the detector plane. In this case, the magnification was about 200 fold.

A jet of water droplets is imaged using laser-accelerated protons of about 2 MeV. Let x_{SO} be the distance from the virtual source to the object and x_{SD} the distance from the virtual source to the detector. Then, the magnification of the droplets is given by the ratio x_{SD}/x_{SO}. Knowing x_{SD} and x_{SO} the diameter of the droplets could be measured to be 16 μm. At first sight, it is quite surprising that the water droplets are even visible on the detector, since 2 MeV protons can easily

penetrate 16 µm of water. But actually, the protons are scattered in the water and lose their laminarity. Protons having passed the water deviate from their original trajectory within a cone with a small opening angle. There is a certain probability that these protons hit the detector outside of the geometrical shadow of the droplet. Thus, the intensity detected within the shadow is reduced. For a detailed discussion of proton radiography of thin objects, see [69].

Temporal resolution

As described in Chapter 3, laser-accelerated proton beams exhibit a broad energy spectrum and a low emittance. The protons originating from the rear side of the laser target are ordered with respect to their velocity: Faster protons fly ahead of the slower ones – they never overtake each other. If an object is imaged by the protons, each velocity class of protons needs a definite time of flight to reach the point where the object is located. Imagine now an expanding object as illustrated by Fig. 5.3.

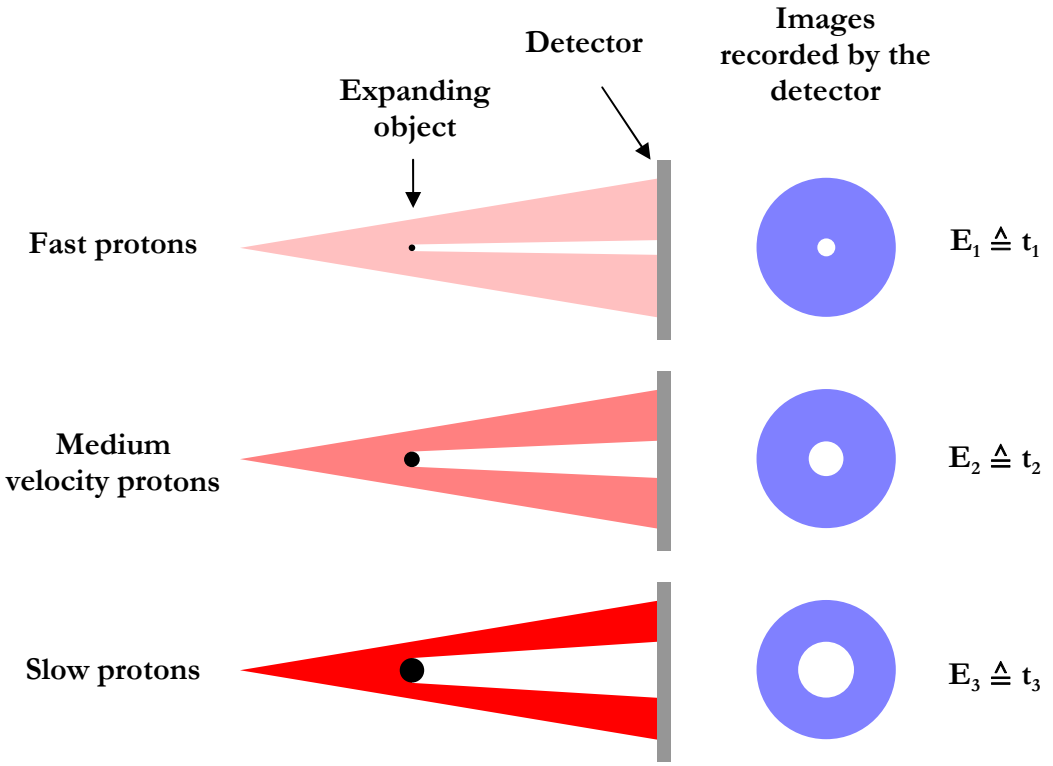

Fig. 5.3: Mapping the temporal evolution of an object with laser-accelerated protons: Highly energetic protons arrive at the object before lower energetic ones. The protons project an image of the object. Each proton energy corresponds to a certain time in the evolution of the object. Thus, the temporal evolution can be mapped with an energy sensitive detector.

The fastest protons will arrive at the object at first, thus producing a shadow of the object at an early time. Slower protons arrive at the object at a later time where the object has already expanded. These protons then produce a shadow of the expanded object. Each proton velocity (and in consequence each proton energy) corresponds to a definite time of the evolution of the object. Using an energy sensitive detector, the temporal evolution of the object can be mapped. Because of the low emittance of the proton beam, the temporal resolution can be of the order of picoseconds.

Proton probing

Since protons are charged particles, they are affected by electric and magnetic fields. Laser plasma physicists take advantage of this property by using laser-accelerated protons to probe electric and magnetic fields. Fig. 5.4 illustrates the principle of proton probing.

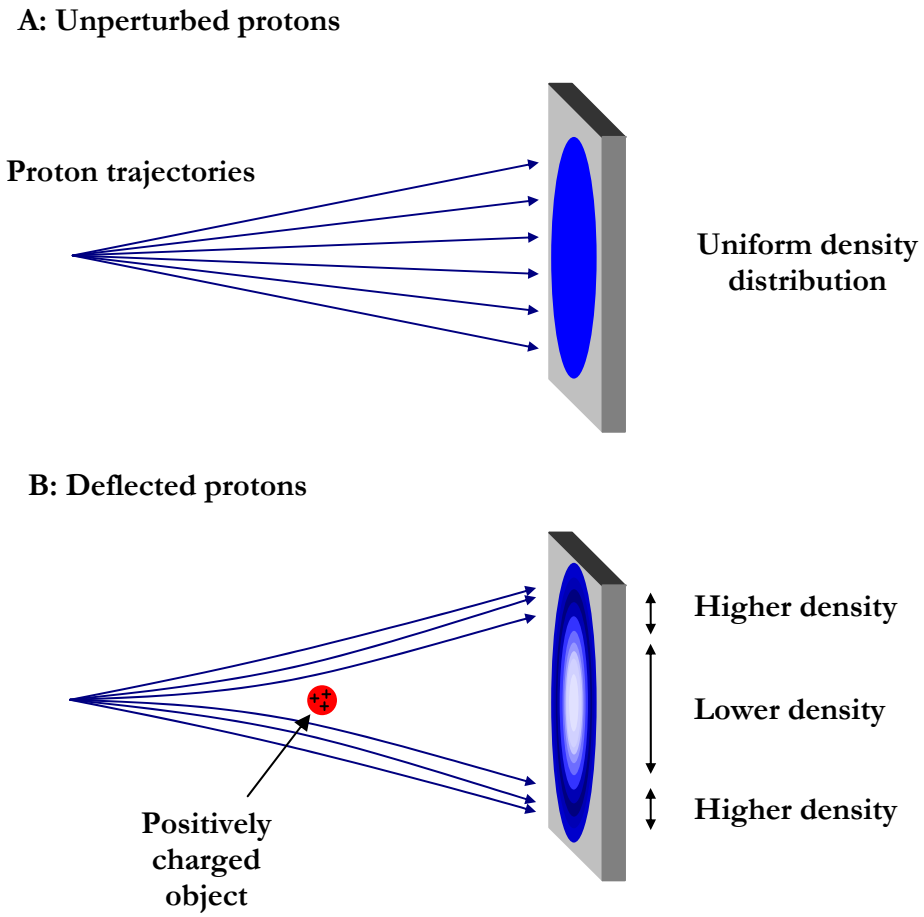

Fig. 5.4: Probing an electric field. A: The unperturbed proton beam yields a uniform density distribution on the detector. B: If the proton beam is deflected by a charged object, a characteristic density distribution can be observed on the detector. Conclusions on the electric field can be drawn.

As mentioned in Section 3.1, the unperturbed proton beam exhibits a great uniformity as shown in Fig. 5.4 A. The effect of an electric field on the proton density distribution is exemplified by Fig. 5.4 B. In the outer regions, the proton density is increased; in the central region, it is reduced. If the areal density distribution of the protons is recorded with spatially resolving detector, conclusions concerning the electric field distribution can be drawn.

Proton probing can of course be performed with temporal resolution, if an energy sensitive detector is implemented as described above. Thus, the temporal evolution of deflecting fields can be investigated.

Proton deflectometry

In Fig. 5.4 one can see that the protons are deflected by the positively charged object in a specific way. The proton trajectories are bent under the influence of the electric field. The detector records the change in proton density distribution, but it cannot measure the effect of the electric field on the individual trajectories. In proton deflectometry [68], a mesh is introduced into the proton beam (Fig. 5.5 A). A shadow of this mesh is projected onto the detector. The position of each grid point of the image on the detector is recorded. If we now introduce an object that is accompanied by electric or magnetic fields (a laser-generated plasma, e.g.), the proton beam is deflected, but individual grid points of the mesh can still be identified on the detector (Fig. 5.5 B). Knowing now the position of a given grid point before and after the introduction of the deflection fields, the displacement of the protons can be measured.

Both the measurement of the areal proton density distribution and the measurement of the displacement of the protons via proton deflectometry enable us to draw conclusions on the fields deflecting the protons. However, it is not possible to reconstruct the fields directly. There are many different fields conceivable that lead to the same image recorded on the detector. That is why one needs to model the electric field, simulate the deflection of the protons and vary the parameters of the model to fit the simulated to the experimental data. The analysis will be described in detail in Section 7.1.

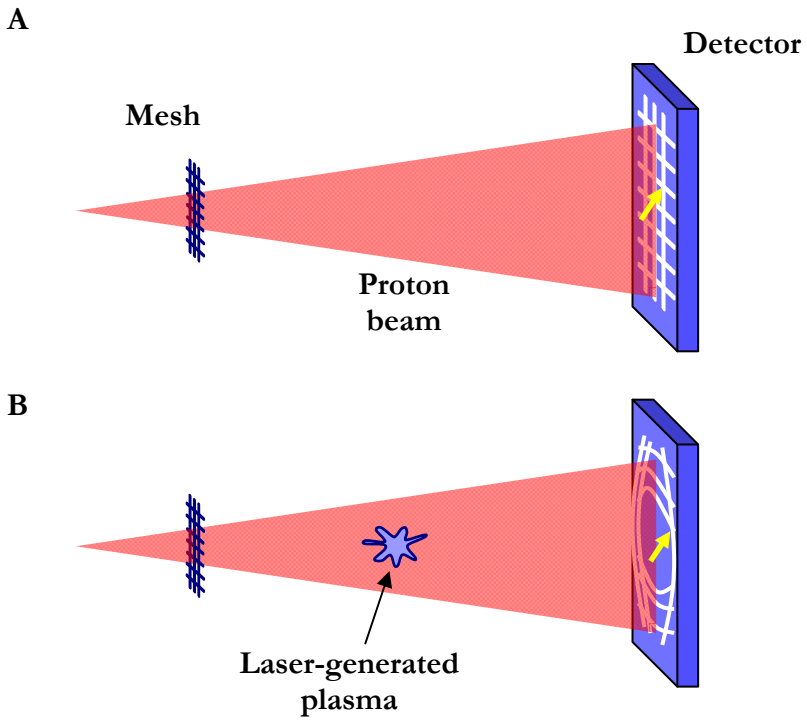

Fig. 5.5: Proton deflectometry: A mesh is introduced into the path of the proton beam. A: The mesh projects a shadow onto the detector. The yellow arrow indicates an individual grid point. B: The proton beam is deflected by the fields of a laser-generated plasma. The yellow arrow shows the new position of the grid point identified in A. The displacement of this grid point can be measured.

Achievements and future prospects of proton probing

Using proton probing, many transient laser-generated plasma phenomena can be investigated, even the TNSA process itself can be imaged (cf. Fig. 5.6) [23].

Proton probing is a promising candidate for diagnostics in inertial confinement fusion, where an implosion is planned to be driven to conditions required for nuclear burn and transient processes in highly dense media need to be accessed. Preliminary experiments have already been performed [70, 71]. (For more information on inertial confinement fusion, cf. Section 4.3.)

Proton probing experiments presented in this thesis offer new perspectives in the investigation of transient plasma phenomena and will be described in Chapter 7.

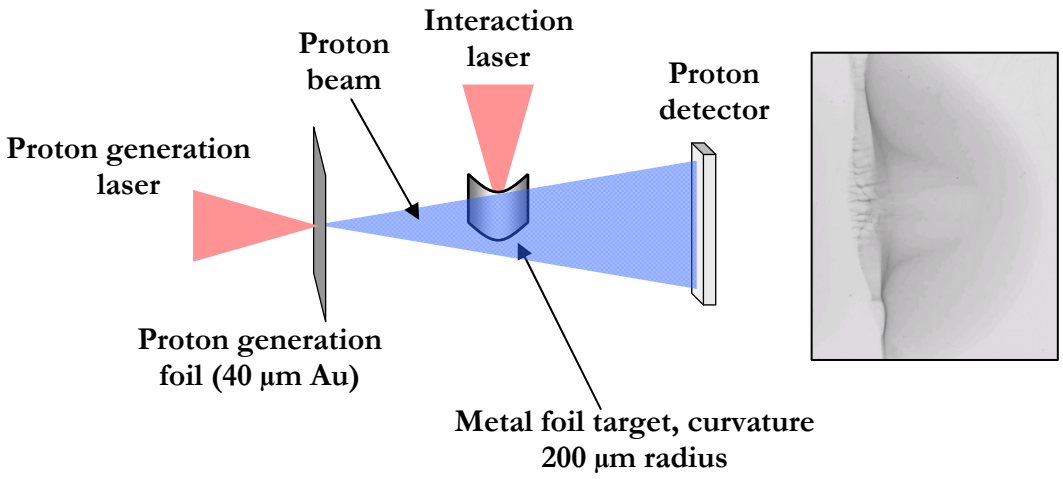

Fig. 5.6: A laser-generated proton beam is used to probe the electric field evolution on the rear side of a laser-irradiated curved foil target. The image on the detector shows the Gaussian-shaped electric field front (detector image taken from [23]).

5.3 Detectors and spectrometers

Radiochromic films

Radiochromic films (RCF) are detectors originally developed for spatially resolved dosimetry in medical applications. Their radiation sensitive component is a microcrystalline monomer that is dispersed in gelatine and coated on a polyester film as a thin layer. Before use, they are completely transparent. But when they are exposed to ionising radiation, the monomer undergoes a polymerisation reaction and turns into a dye polymer. As a consequence, the exposed area darkens. The optical density of the exposed film is a measure for deposited dose. The polymerisation reaction does not spread from one microcrystal to another. Thus, a high spatial resolution can be achieved. To measure the optical density, a flatbed scanner can be used.

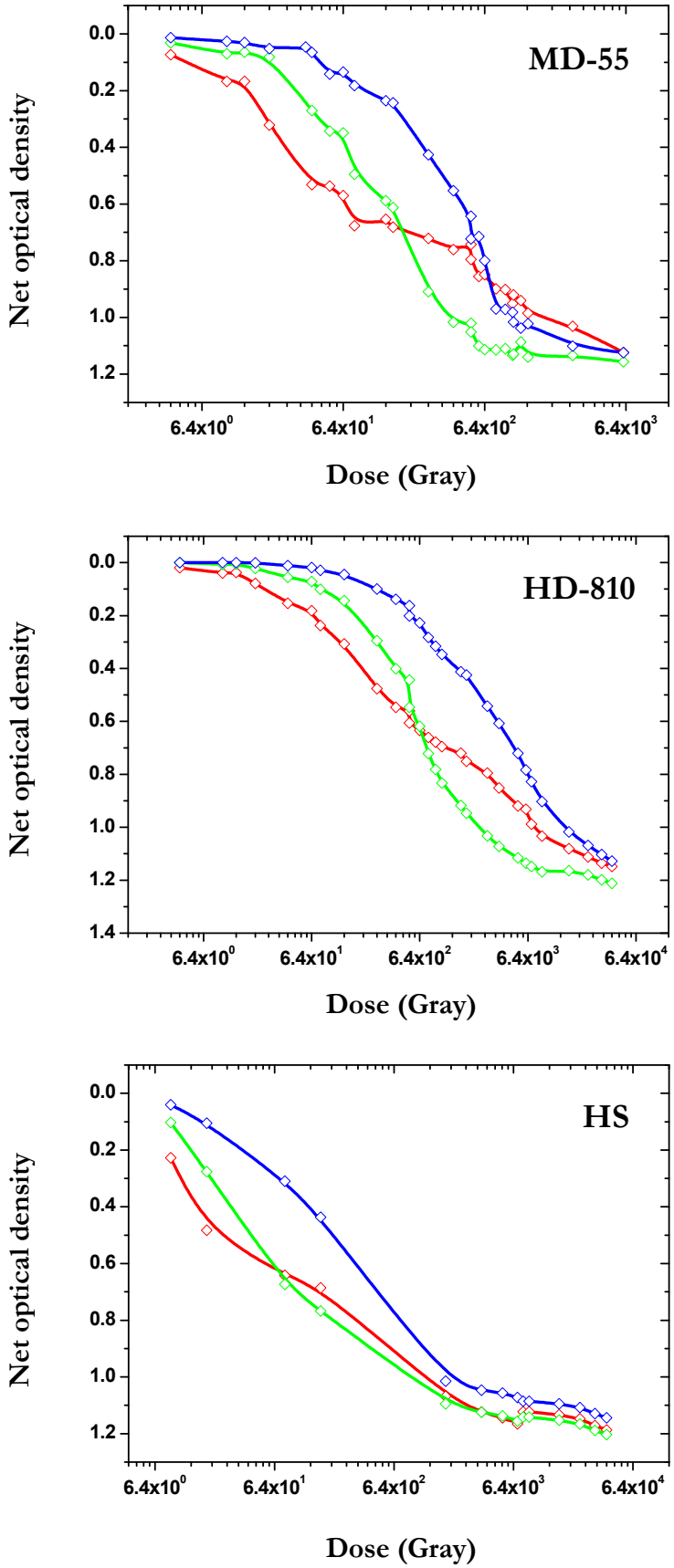

Fig. 5.7: Optical density against dose deposited by 8 MeV protons for different kinds of radiochromic film. Calibration curves for the three channels of the scanner are depicted in the corresponding colour.

Different types of radiochromic film are available. Among these are:

- MD-55: two radiation sensitive layers between two polyester foils carrying and protecting the sensitive layers
- HD-810: one sensitive layer on a polyester carrier
- HS: a highly sensitive film consisting of one sensitive layer protected by polyester from both sides

Further information provided by the manufacturer can be found under [92]. Unfortunately, calibration data for highly energetic protons are not provided by the manufacturer. That is why calibration was done at the tandem Van de Graaf accelerator at the *Max-Planck-Institut für Kernphysik* in Heidelberg. Samples of radiochromic film were irradiated by 8 MeV protons. For the three films described above, the dependence of the optical density on the deposited dose was recorded. The particle number was monitored by a Faraday cup[*]. The optical density was measured using a Microtek Artix scanner (1800 dpi): Let I_0 be the intensity recorded when scanning an unexposed film and I_{exp} the intensity for an exposed film. The net optical density is then given by $\log(I_0/I_{exp})$. Thus, the optical density is a measure for the darkening of the film. The scanner maps the absorption of the material on three optical channels (red, green and blue). The absorption of the polymer strongly depends on the wavelength of the light and thus, the three channels yield different results. The results are depicted in Fig. 5.7. The calibration data needs to be handled with care, because using another scanner, slightly different results could be obtained.

Radiochromic films in laser ion acceleration experiments

As already described above, many laser ion acceleration experiments require detectors that are able to record the areal density distribution of an ion beam. Furthermore, energy sensitive detectors are desired for proton imaging experiments (cf. Section 5.2). Radiochromic films meet both requirements. Imagine a stack of radiochromic films positioned in a proton beam as depicted in Fig. 5.8. As mentioned in Section 4.1, most of the energy of the protons is deposited in the Bragg peak. The penetration depth of the protons in solid material depends on their kinetic energy and so does the position of the Bragg peak. Protons of the same particular energy will deposit most of their energy in the same layer, while higher energetic protons penetrate deeper into the material and deposit their energy in another layer. Thus, each layer of the RCF stack

[*] A Faraday cup collects charged particles. The current from the cup is measured and integrated over time. Thus, the total charge of the particles collected is obtained.

shows the density distribution of a particular energy class of protons. If we use an RCF stack detector in a proton probing experiment, each layer will show a particular time in the evolution of the probed object.

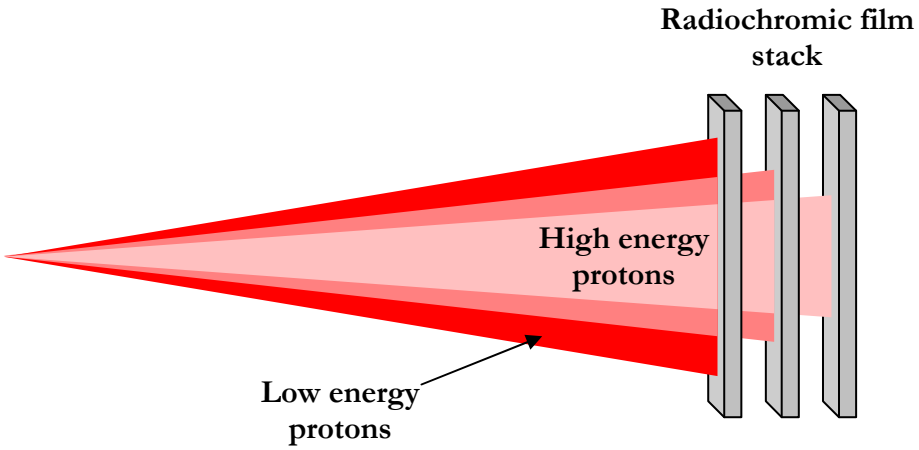

Fig. 5.8: Energy sensitive RCF detector: High energy protons penetrate deeper into the stack than low energy protons, both depositing most of their energy in the Bragg peak.

Imaging Plates

Radiochromic films are easy to handle since they are self-developing and almost insensitive to visible light; the result can be viewed by eye immediately. However, in many cases their sensitivity is not sufficient to detect a small number of particles. Imaging Plates (a product of *Fujifilm*) exhibit a higher sensitivity to the price of a more complicated readout procedure. In addition, they cannot be stacked.

Imaging Plates are coated with a photo-stimulable phosphor layer consisting of Eu^{2+} doped barium fluorobromide. If this layer is exposed to ionising radiation, it stores excitation energy by forming electronic colour centres in lattice defects. This energy can be released as fluorescence when the Imaging Plate is exposed to visible light. To be read out, the exposed Imaging Plate is scanned by a laser and the emitted light is collected. Subsequently, the Imaging Plate can be erased completely within approximately half an hour by the use of conventional fluorescent lamps.

For further information on Imaging Plates, please refer to [93].

Solid state nuclear track detectors

Solid state nuclear track detection (SSNTD) takes advantage of the fact that a high energy ion penetrating a non-metal solid state material usually leaves a track along its path by damaging the local molecular or lattice structure of the material. In the case of a polymer e.g., the ion cuts the long molecular chains by ionisation. These tracks are not visible in the first place. However, the material is sensitive to corrosion along the tracks. In a corrosive solution, the tracks can be etched out to small conical caves. This process is not applicable to every material, and for each material that can be used for SSNTD there are restrictions concerning ion species and energy. Since the possibility to etch the latent tracks depends on the energy deposition in the material, nuclear track detectors are more sensitive to heavy ions than to light ions and more sensitive to lower energy ions than to higher energy ions. Therefore, protons with an energy above 500 keV can only be detected by the most sensitive of all known track detector materials – a polymer called *CR-39*. CR-39 is manufactured as an industrial product and used mainly for eyeglass lenses. Since tracks of individual particles are recorded by nuclear track detectors, plates of CR-39 can be used to detect even small numbers of protons. Automated readout systems are commercially available. The readout yields the coordinates of each detected proton.

CR-39 is not available as a thin foil. As a consequence, it cannot be stacked. There have been several attempts to produce thin foils of CR-39 by etching or by mechanical treatment [94]. These techniques, however, are either extremely complex, time-consuming or yield unsatisfactory results.

For further reading on SSNTD including recipes for etching, [95] is recommended.

Micro-channel plates (MCP)

Radiochromic films, Imaging Plates and nuclear track detectors need to be exchanged after every laser shot. High power short pulse laser experiments are usually conducted under vacuum. Using radiochromic films or Imaging Plates, the target chamber or at least a part of it needs to be vented and pumped after every shot – a procedure particularly undesired for experiments at a high repetition rate laser. This problem can be solved using micro-channel plates (MCP). An MCP mainly consists of a plate that is perforated with channels like a sieve. These channels have a diameter of a few micrometres and are ordered in a hexagonal pattern. A voltage in the order of 1 kV is applied to the sides of the plate, so that the electric field acts along the channels. Then, each micro-channel acts as an electron multiplier: If an energetic ion hits the inner wall of a channel, electrons are emitted from the irradiated surface. While being accelerated by the electric

field, the electrons hit the wall of the channel and release further electrons that undergo the same process. The electrons leave the MCP on the other side and hit a phosphorous screen whose luminance can be recorded by a simple CCD-camera. The principle is depicted in Fig. 5.9. For further reading, [96] is recommended.

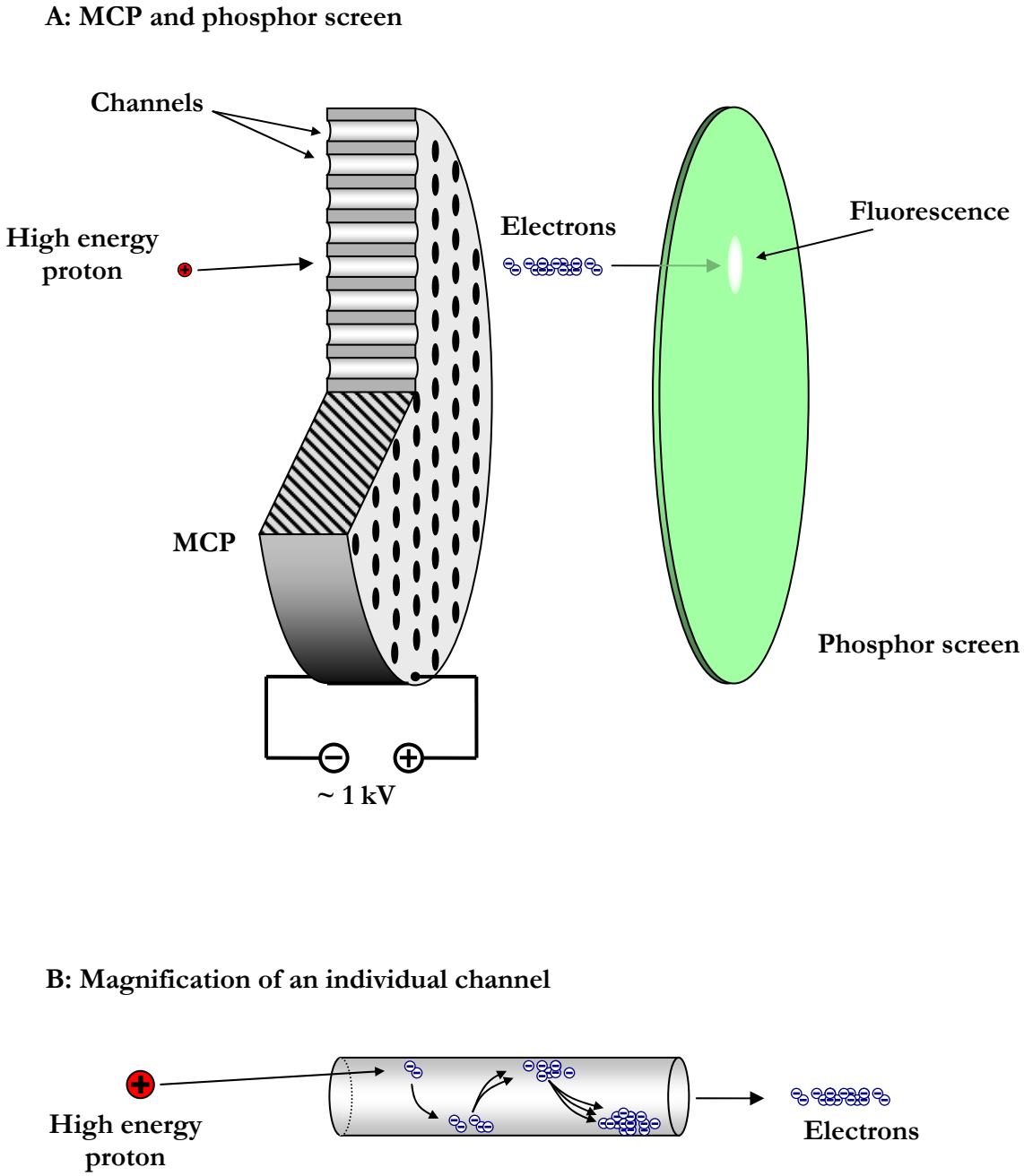

Fig. 5.9 A: Schematic of a micro-channel plate. The MCP converts single energetic protons into a large number of electrons that are accelerated onto a phosphor screen. On the phosphor screen, the electrons induce a fluorescence pattern that reproduces the proton density distribution. B: A magnified channel of the MCP. The proton hits the inner wall of the channel releasing electrons. While being accelerated, the electrons hit the wall and release further electrons.

Thomson spectrometer

The Thomson mass spectrometer (colloquially also known as Thomson parabola) was firstly described in 1911 by J. J. Thomson [97]. Because of its simple and robust setup and the variety of information that can be retrieved from the recorded spectra, it is still today a commonly used diagnostic tool. A schematic of the setup is shown in Fig. 5.10.

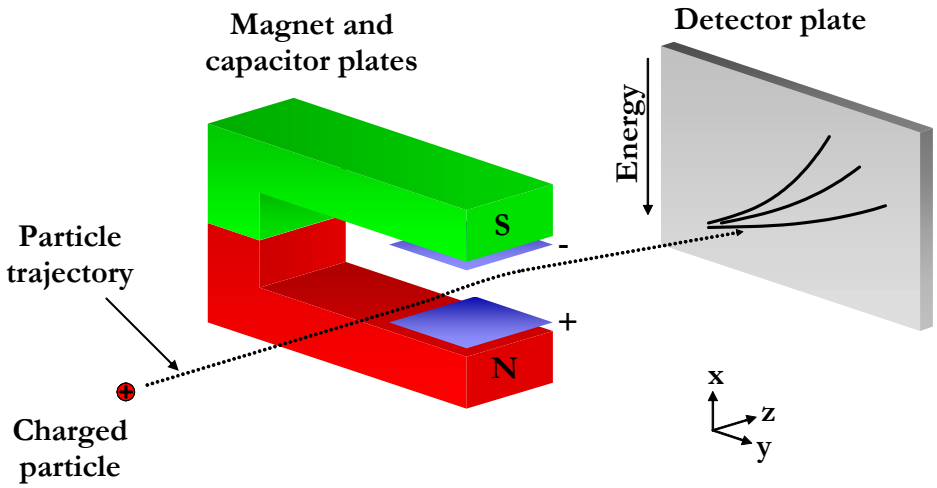

Fig. 5.10: Thomson spectrometer. Charged particles pass a region of an electric and a magnetic field that are parallel to each other. The particles are deflected by the fields in a specific way: They are sorted with respect to their charge-to-mass ratio and dispersed with respect to their energy. Each group of particles having the same charge-to-mass ratio hits the detector plane on an individual parabola. Each point of a parabola corresponds to a particular particle energy.

A magnet provides a homogenous magnetic field along the x-axis. This field is superimposed by a homogenous electric field pointing in the same direction. A beam of charged particles flying along the z-axis passes through these fields. After being deflected by the fields, the particles are detected on a plate.

The equations of motion of the particles can be solved by relatively simple means [98]. Then, the x- and the y-coordinate of a particle in the detector plane are given by:

$$x\left(z_{detector}\right) = \frac{qEL}{mv^2} z_{detector} \tag{5.1}$$

$$y\left(z_{detector}\right) = \frac{qBL}{mv} z_{detector} \tag{5.2}$$

where $z_{detector}$ denotes the distance between the centre of the fields and the detector plane, q is the charge of the particle, L is the length of the field region in z-direction and E and B denote the electric and the magnetic field, respectively. From these two equations one can infer that the deflection in y-direction is inversely proportional to the momentum of the particle while the deflection in x-direction is inversely proportional to the kinetic energy of the particle. To obtain the relation between $x(z_{detector})$ and $y(z_{detector})$, one can insert Eq. (5.2) into Eq. (5.1):

$$x = \frac{m}{q}\frac{E}{B^2 L z_{detector}} y^2$$
$$or \qquad (5.3)$$
$$x = \frac{m}{q} a\, y^2$$

where a is a device constant for the Thomson spectrometer. Eq. (5.3) shows that ions having the same charge-to-mass ratio hit the detector on a parabolic curve. The particle density on the detector can be read out along the parabolic curve. Since the x-position corresponds to the energy of the particle (Eq. 5.1), an energy spectrum for each ion species can be obtained.

Proton streak deflectometry

As described above, stacks of radiochromic films provide a temporal resolution when probing the evolution of an object using laser-accelerated protons. Radiochromic films, however, offer only a few snapshots of the temporal evolution of the object. The number of these snapshots is limited by the maximum energy of the protons. Furthermore, radiochromic films exhibit only a mediocre sensitivity in comparison to other detectors. Thus, RCF stacks are applicable only at laser facilities that are able to generate large numbers of high energy protons. To overcome these problems, proton streak deflectometry was developed. This diagnostic technique was applied for the first time in an experiment presented in Section 7.1. To explain the functional principle, the setup is depicted in Fig. 5.11. It resembles the setup of a standard proton deflectometry experiment as described in Section 5.2 except for a slit and a magnet that are introduced into the beam behind the object that is to be probed. The slit cuts out a horizontal cross section of the beam. Subsequently, this part of the beam passes through a magnetic field that vertically disperses the protons with respect to their velocity; the faster protons are deflected less than the slower ones. As usual, the proton distribution is recorded by a detector. Since the velocity of the protons corresponds to their time of flight to the probed object, the vertical axis on the detector corresponds to the time in the evolution of the object. The horizontal axis provides one dimensional spatial information.

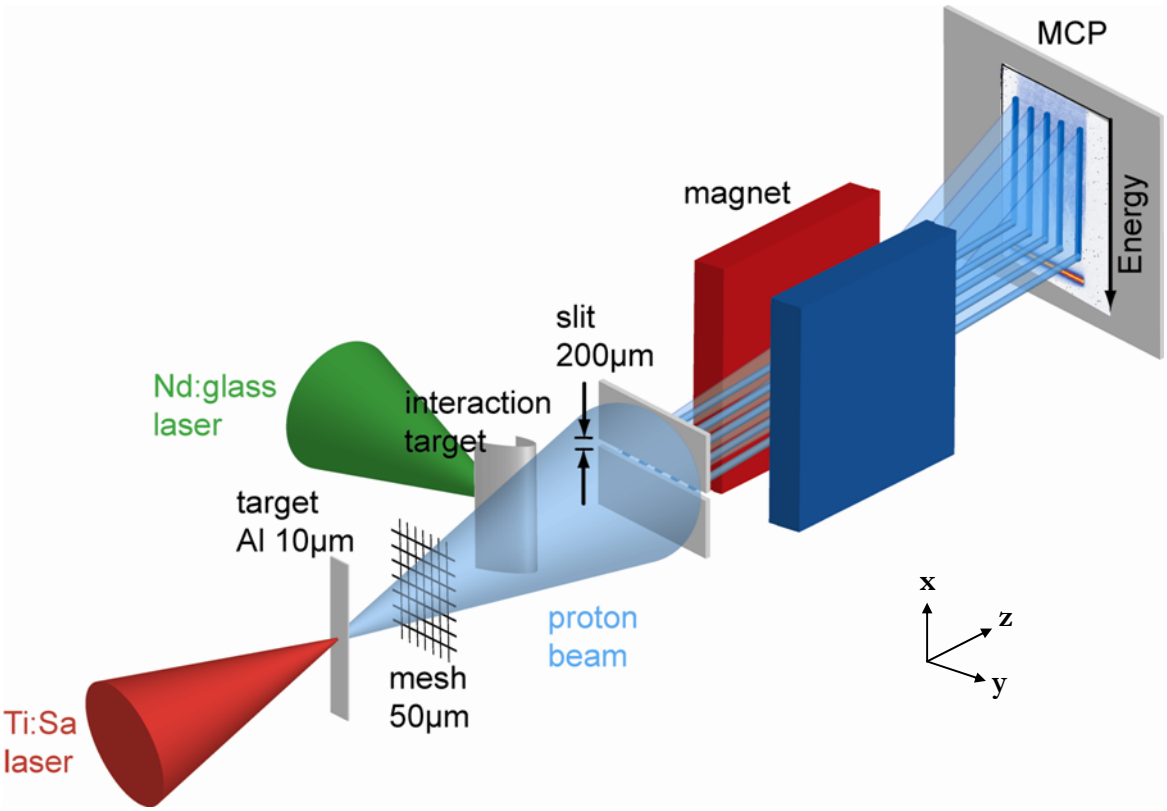

Fig. 5.11: Proton streak deflectometry: The temporal evolution of the interaction target can be mapped continuously (from [8]).

In the experiment depicted in Fig. 5.11, the probed object is a plasma expanding on the rear side of a laser-irradiated target. The plasma expansion is accompanied by electric fields deflecting the protons. In the detector plane, the x-axis corresponds to the time, while the y-axis corresponds to the proton deflection. Thus, the temporal evolution of the y-component of the electric field can be mapped continuously.

6 The controlled generation of proton and carbon ion beams

This chapter addresses the challenges of the production and control of proton and carbon ion beams. The design of advanced particle sources is described. Their benefits are investigated and discussed.

6.1 Beam optimisation using mass-limited targets

Mass-limited (i.e. small and isolated) targets have the potential to show significant advantages compared to large plain foils. In the standard laser proton acceleration experiment, the hot laser-generated electrons cannot be prevented from spreading over the whole rear surface of the target. The electron cloud dilutes while expanding, the electron density decreases and so does the electric field in the Debye sheath. Since this electric field is responsible for the acceleration of protons and heavier ions, an increase in energy and number of the accelerated particles is to be expected, if the electrons can be confined. On a small and isolated target, hot laser-generated electrons can spread only over a limited surface. As in the case of a large foil, only few electrons can escape from the surface, the others are kept back by the electric field that builds up between the electrons and the positive charge on the target.

The experiment described in the following was carried out at the LULI, École Polytechnique. Thin foil targets of different sizes are irradiated by a frequency-doubled Nd:glass laser. Foils of two different thicknesses are used (2 μm and 10 μm). A standard millimetre-sized foil target is compared to small rectangular foil targets that are attached to a glass stalk and a circularly shaped target on a silicon stalk. The proton beam originating from the rear side of the targets is recorded by a radiochromic film stack. A hole is bored into the RCF stack. The central part of the proton beam passes through the stack and is analysed using a magnetic spectrometer.

As described in Section 5.1, every laser pulse is preceded by a significant amount of radiation, the so-called prepulse. This prepulse is able to induce the formation of a plasma on the surface of the target. The plasma flows over the surface of the target. In the case of a small target, the plasma flows around the edges of the target and perturbs the rear surface. Thus, the formation of plasma on the target surface inhibits an efficient laser-acceleration of protons and heavier ions from the rear side of a small target. The laser was frequency-doubled to reduce the influence of the

prepulse: A second harmonic is generated in a nonlinear crystal. This is a nonlinear process; the efficiency of the frequency conversion strongly depends on the light intensity. Thus, low intensity parts of the laser pulse – such as the prepulse – are suppressed at the doubled frequency.

An overview on the results of the experiment is depicted in Fig. 6.1.

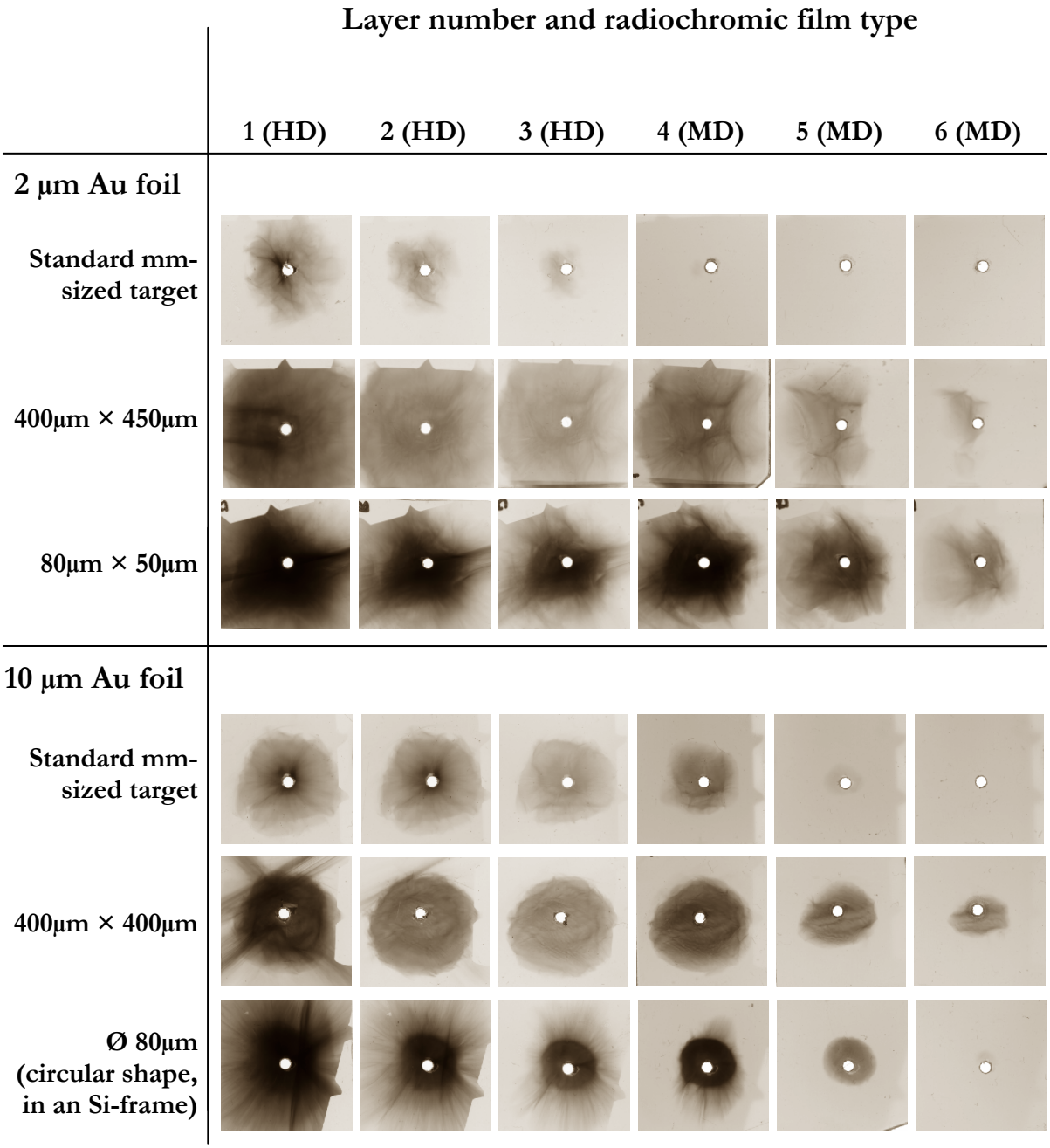

Fig. 6.1: Variation of the target size – layers of the RCF stacks (details).

The reduction of the target size leads to a reduction of the beam divergence and an increase of the number of accelerated protons. Additionally, the maximum energy of the protons is increased. This behaviour is observed both for the 2 µm and the 10 µm gold foils.

Fig. 6.2 shows a comparison of the energy spectra from the large 2 µm Au foil target and the 80 µm × 50 µm × 2 µm Au foil target.

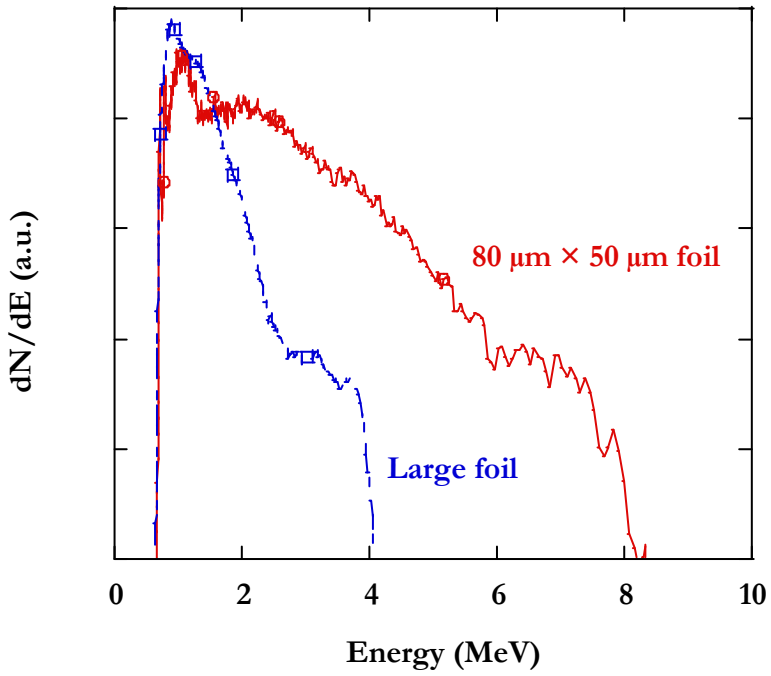

Fig. 6.2: Comparison of the energy spectra from a large 2 µm Au foil target and a 80 µm × 50 µm × 2 µm Au foil target.

Compared to the proton beam from the large foil target, the beam from the mass-limited target shows an extension of the spectrum to higher energies. The maximum proton energy from the mass-limited target exceeds the one from the large foil by a factor of two.

On a large foil, the electrons spread over an area that has a diameter of about 100-200 µm (cf. Sections 2.2 and 5.2). The small foil targets used in this experiment confine the electrons on a much smaller area. This results in an increase of electron density. The relation of the electron density and the acceleration field is given by Eq. (2.16). For the beginning of the plasma expansion (at $t = 0$), Eq. (2.16) can be written as:

$$E_{front} \approx \sqrt{\frac{2 n_{e0} k_B T}{e_{math} \varepsilon_0}} \tag{2.16}$$

(where E_{front} is the acceleration field, n_{e0} is the electron density, k_B is the Boltzmann constant, T is the electron temperature, e_{math} is the base of the natural logarithm and ε_0 is the vacuum permittivity.) The acceleration field is proportional to $\sqrt{n_{e0} T}$. The electron temperature mainly depends on the parameters of the laser pulse and on the target thickness and material. Therefore, the electron temperature can be considered constant when varying only the lateral extension of the target. In this case, the increase of the acceleration field is directly connected to the electron confinement.

This experiment shows the advantageous properties of mass-limited targets separated from other effects occurring in experiments with more complicated mass-limited targets as described in Section 3.2, e.g.

Due to the recent progress in laser development, commercial high contrast laser systems are now available. Size reduction of the targets is a simple way to improve the properties of laser-accelerated proton beams at theses laser systems. Furthermore, the investigation of more sophisticated mass-limited targets can be envisioned.

A special kind of mass-limited targets – laser-irradiated water droplets – will be investigated in Section 7.2. As described in Section 3.2, these targets have been shown to be the origin of quasi-monoenergetic protons and deuterons. The processes connected to the interaction of a short pulse high power laser with these targets are widely unknown and will be studied by the use of proton probing.

6.2 The control of laser-accelerated carbon ion beams

Most laser ion acceleration experiments concentrate on laser-accelerated protons. In the standard experiment, a thin foil target is irradiated by a short pulse high power laser. If no special treatment is applied to the target, the beam emitted on the rear side of the target will mainly consist of protons. Protons have the highest charge-to-mass ratio of all ions and are therefore accelerated most efficiently. For some applications, however, the use of carbon ions might be favourable. The advantages of carbon ions in cancer radiotherapy e.g., are pointed out in Section 4.4. Another example is the use of carbon ions for isochoric heating (cf. Section 4.1). Since the energy loss of a nucleus penetrating solid matter is proportional to Z^2 (Z being the

atomic number), heating matter with carbon ions is potentially much more efficient than heating with protons. Both applications require beam focussing or collimation. Furthermore, monoenergetic beams are required for radiotherapy. Focussing techniques have been presented in Section 3.1. However, they were so far only demonstrated for protons. In the following, the possibility to focus laser-accelerated carbon ions will be discussed. Furthermore, an easy way to generate quasi-monoenergetic carbon ions will be presented. The experiments concerning carbon ions were conducted at the LULI 100 TW facility.

The carbon ion focussing experiment

The experiment that aims at focussing carbon ions is depicted in Fig. 6.3. The setup is similar to the proton focussing setup by Toncian et al. [50] described in Section 3.1.

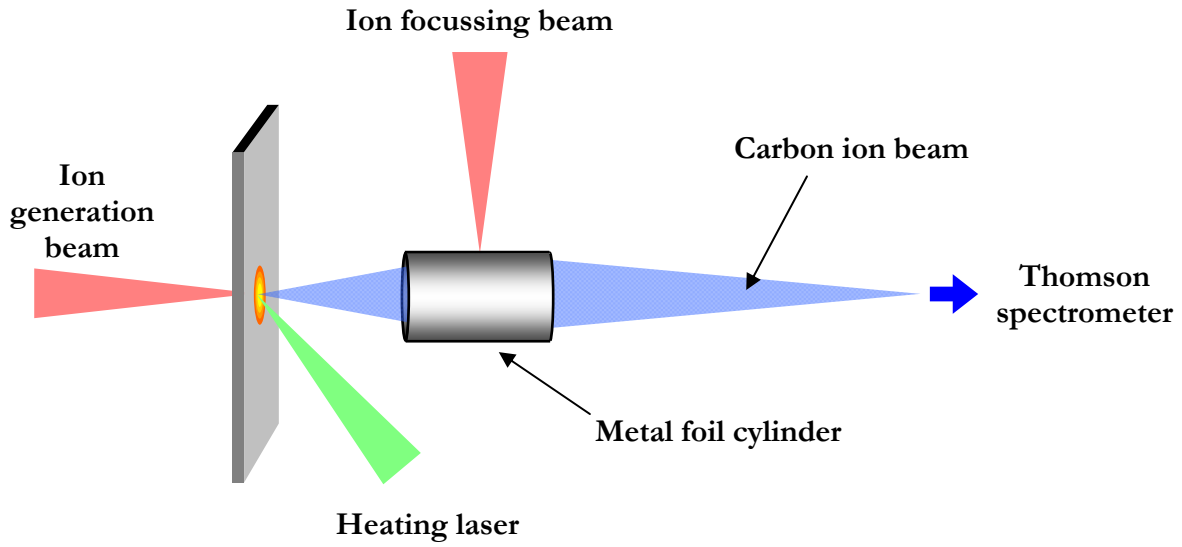

Fig. 6.3: Carbon ion beam focussing using a laser-irradiated hollow metal foil cylinder. The cylinder has an outer diameter of 810 µm, a wall thickness of 51 µm and a length of 2 mm. The material is Dural (95% Al, 4% Cu, 1% Mg). The proton generation beam delivers an energy of ~15 J within 320 fs. The ion focussing beam delivers an energy of ~10 J within 400 fs.

The particle beam originates from the rear side of a plain laser-irradiated foil target and passes through a hollow metal foil cylinder. The cylinder is irradiated by another laser pulse that is synchronised to the first one. Hot electrons spread over the inner surface of the cylinder and induce a plasma expansion with a rotational symmetry. This plasma expansion is accompanied by transient radial electric fields that are supposed to focus a part of the particle beam. Only those particles are affected that are located inside the cylinder when the second laser pulse hits the

outside of the cylinder. By setting the delay between the two laser pulses, a velocity class of particles that is to be focussed can be chosen. The delay between the laser pulses corresponds to the time-of-flight of this velocity class of particles to the exit of the cylinder. The carbon focussing experiment differs from the proton focussing experiment: It additionally includes a continuous wave laser that irradiates the rear side of the plain foil target. The laser heats up the part of the foil that is the source of accelerated particles. It drives off the hydrogen contaminants leaving the more heat resistive carbon contaminants behind. The electric field that drives the ion acceleration is no longer screened by the protons and thus, carbon ions can be accelerated efficiently. The particle beam is analysed using a Thomson parabola spectrometer (cf. Section 5.3). An aperture limits the number of particles that enter the spectrometer. For the velocity class that is chosen to be focussed, a significant increase of the particles passing through the aperture is to be expected (since the ions are focussed into the spectrometer.) In the corresponding proton focussing experiment, a peak in the energy spectrum of the protons could clearly be observed [50].

Fig. 6.4 shows the result of an experiment where the lasers were synchronised to focus 12 MeV carbon ions. The figure shows a detector image from the Thomson spectrometer. The carbon ions are identified. The parabolic traces of C^{4+}, C^{5+} and C^{6+} show modulations indicating an influence of the laser-irradiated cylinder. The particle density was read out along the traces and transformed into energy spectra.

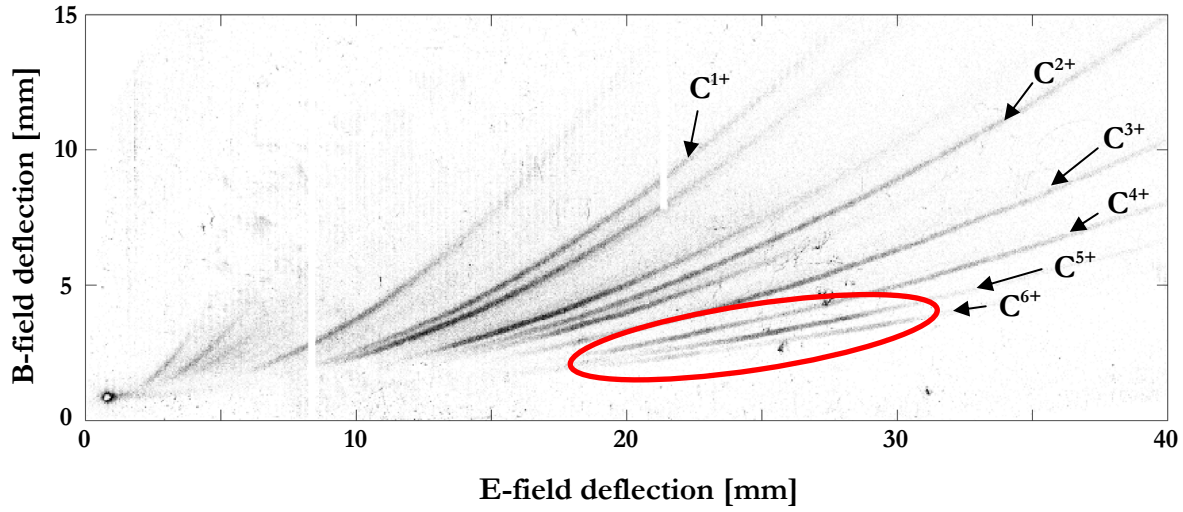

Fig. 6.4: Parabolic traces of different ions detected by the Thomson spectrometer. The traces of the six carbon ions are identified. The traces of C^{4+}, C^{5+} and C^{6+} show modulations within the range that is marked by the red ellipse. The image is a particle density plot that was composed of individual particle track coordinates from the readout of the CR-39 detector in the Thomson spectrometer.

The energy spectra are depicted in Fig. 6.5. The three spectra show an interesting feature around the energies of 5 MeV and 12 MeV: The ion number detected at these two energies seems to break down. For the 5 MeV region this can clearly be seen in the spectrum of C^{4+}. For the 12 MeV region the effect is visible in the spectrum of C^{6+}. The spectrum of C^{5+} seems to be affected both on the rising and the trailing edge of the curve.

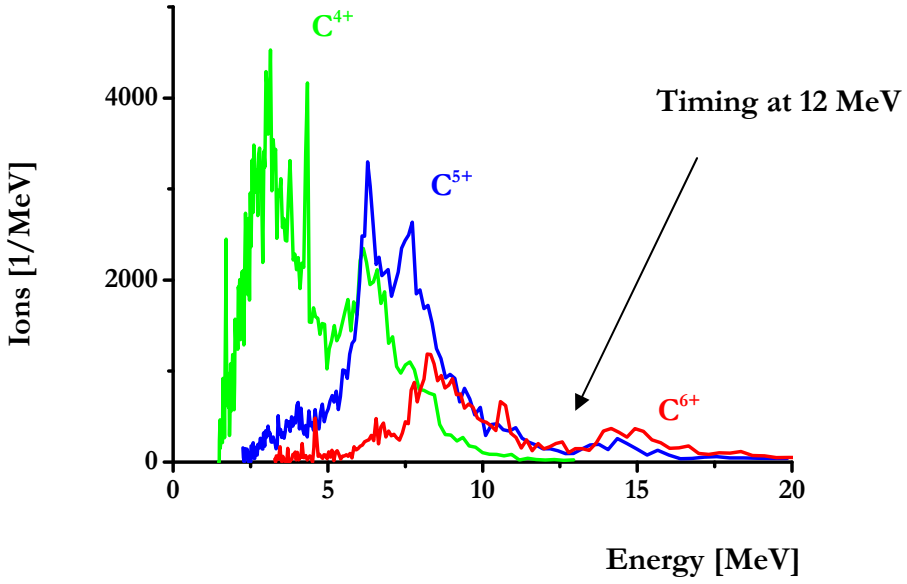

Fig. 6.5: Spectral readout from the traces of C^{4+}, C^{5+} and C^{6+}.

Fig. 6.6 shows a comparison between the spectrum of C^{5+} and a reference spectrum that was taken without the metal cylinder. Due to shot-to-shot fluctuations, the particle number of the reference spectrum is much lower than the particle number in the spectrum obtained when using the metal foil cylinder. To make both spectra comparable, the reference spectrum was smoothened and scaled up to the total particle number of the other spectrum. The comparison unambiguously shows a narrowing of the spectrum. It is not so clear, however, if a part of the spectrum is enhanced (as expected in the case of a focussing effect) or if parts of the spectrum are simply cut, leaving behind a narrowed spectrum.

To investigate the formation of the peak in the C^{5+} spectrum, particle tracing simulations are conducted. Modelling the electric field as described in Section 2.3 *in the interior* of the laser-irradiated cylinder is not advisable: If the one dimensional electric field is applied along field lines normal to the surface of the target, the field lines converge and meet at the symmetry axis of the

cylinder – the model becomes more and more unrealistic when approaching the centre of the cylinder. Thus, the temporal evolution of the electric field in the interior of the cylinder is extracted from a one dimensional PIC simulation that assumes rotational symmetry.

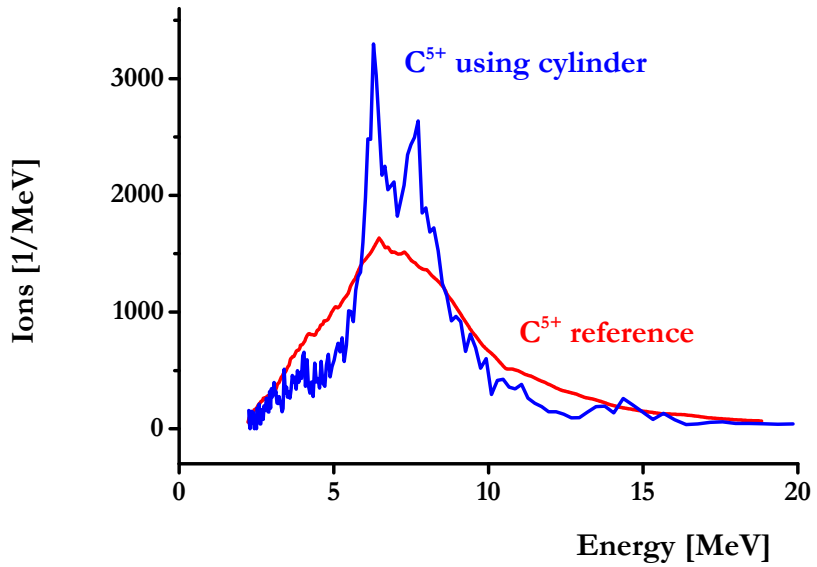

Fig. 6.6: Comparison between the spectrum of C^{5+} influenced by the laser-irradiated metal foil cylinder and the unperturbed C^{5+} spectrum as a reference. The reference spectrum was smoothened and scaled up.

The data is implemented into the particle tracing code described in the appendix. The program simulates the trajectories of C^{5+} ions with an energy distribution that corresponds to the reference spectrum. After having passed the cylinder, the ions are collected by a virtual spectrometer. Fig. 6.7 shows a simulated spectrum in comparison to a scaled reference spectrum.

The simulated output spectrum shows a shape that is qualitatively in good agreement with the experimental one. A breakdown of the signal around 5 MeV and around 10 MeV can be observed. Between these two regions, a peak is visible. The width of the peak in the simulated spectrum was fitted to the width of the experimental spectrum by varying the ratio between the aperture size of the entrance of the spectrometer and the distance between the exit of the cylinder and the entrance of the spectrometer. It was found that the aperture of the spectrometer needed to be closer to the cylinder or larger than in the experiment to reproduce the width of the peak. Please note that the electric field data is based on a one dimensional PIC simulation that cannot reproduce the processes in the real experiment completely.

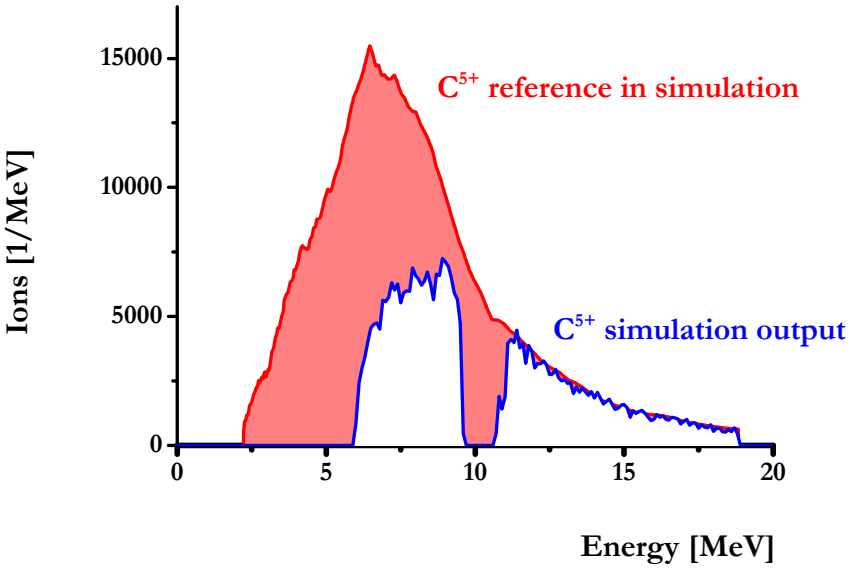

Fig. 6.7: Electric fields from a PIC simulation are implemented into a particle tracing code. The reference spectrum was used as the input energy distribution of the simulated carbon ions. The blue curve shows the output energy distribution of the simulation.

Comparing the input spectrum to the output of the simulation, one can see that parts of the input spectrum were cut or suppressed leaving behind a peak similar to the one observed in the experiment. An overshoot of the spectrum as expected for focussing cannot be observed. The formation of the peak in the C^{5+} spectrum is an effect caused by the laser-irradiated cylinder but it does not seem to be focussing. The focussing method does not seem to be easily transferable from protons to heavier ions.

When the electric fields in the cylinder build up, particles are deflected into the aperture of a spectrometer only within a short time interval. All particles that follow are deflected stronger – they are defocused. Their energy is suppressed in the spectrum. This is of course desired to obtain a quasi-monoenergetic signal. In the case of the carbon ion experiment, however, this might be a problem: Having a mass that is approximately 12 times the mass of the proton, a carbon ion is much slower than a proton at a comparable energy. Furthermore, the total number of C^{5+} ions is much lower than the number of protons in a usual proton acceleration experiment. Thus, the flux of carbon ions through the exit of the cylinder is tiny compared to the flux of protons in a proton focussing experiment. Within the short time that the focussing field is active

at the exit of the cylinder, only few carbon ions are affected – not enough to form a visible peak in the spectrum.

The problem becomes evident when regarding the result of a repetition of the experiment using Imaging Plates (cf. Section 5.3) instead of CR-39 as a detector in the Thomson spectrometer. A detail of a detector readout is depicted in Fig. 6.8. In this case, the suppression of protons via laser heating is incomplete. A residual proton trace and a carbon ion trace are visible. Both traces show the characteristic gap that is caused by the deflection fields of the cylinder. Due to the higher charge-to-mass ratio of the protons and the correspondingly higher energy dispersion of the spectrometer, the gap on the proton trace is broader than the one on the carbon trace. The focussing peak is expected to appear just before the gap and indeed, an enhanced signal is visible on the proton trace. On the carbon ion trace, an enhancement of the signal cannot be observed. Although the dispersion of the spectrometer is lower in the case of carbon ions, the trace is even fainter than the one of the protons. There are probably not enough carbon ions to form a detectable peak.

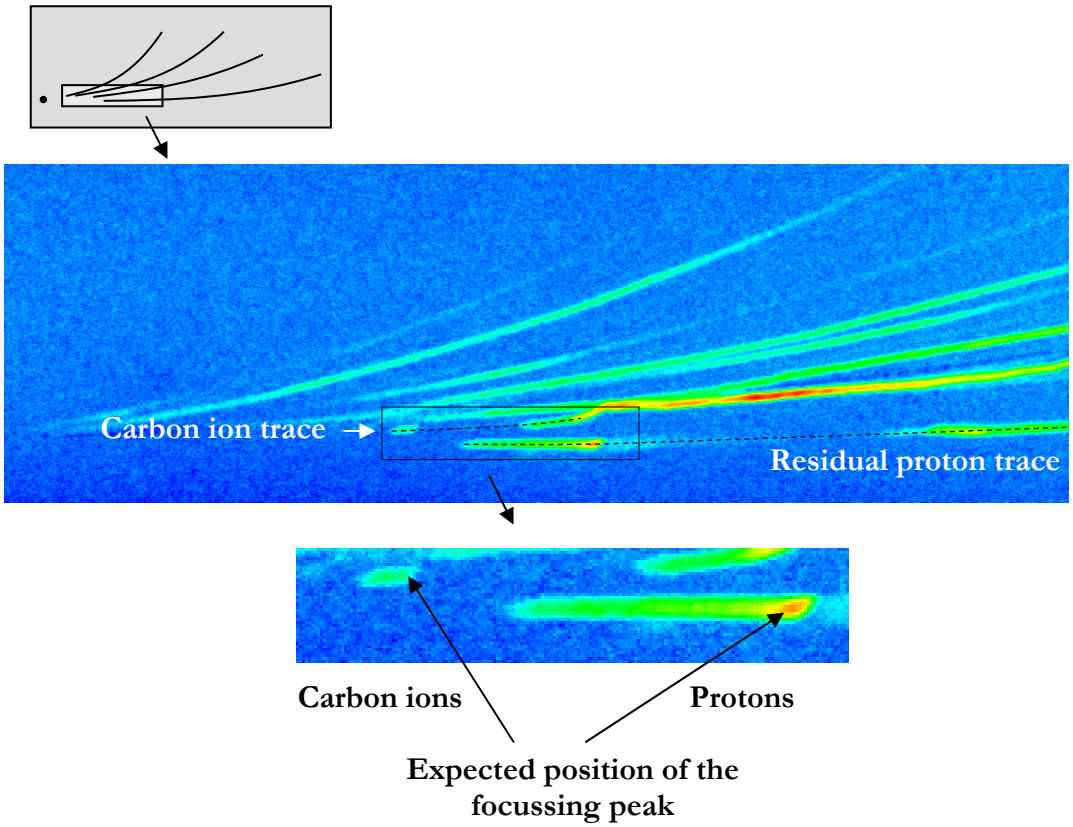

Fig. 6.8: Detail of the detector readout from an ion focussing experiment. The carbon ion trace and the residual proton trace are marked with a dotted line. (The carbon ion trace shows wiggling at a low energy. This is caused by a fluctuation of the voltage applied to the Thomson spectrometer and does not effect the energy range that is of interest.)

New acceleration techniques such as the use of mass-limited targets (cf. Sections 3.2 and 6.1) have the potential to generate significantly higher amounts of carbon ions at higher energies. As soon as improved carbon ion beams are available, carbon ion focussing using a laser-irradiated hollow metal foil cylinder is likely to become feasible.

Quasi-monoenergetic carbon ion beams

As described above, hydrogen contaminants can be removed from the target by laser heating. In the previous subsection, carbon ion beams exhibit a broad energy spectrum. In the experiment described in the following, the effect of a long heating time at a high heating power is investigated. The experiment was conducted at the LULI 100 TW laser (cf. Table 5.1). The setup is depicted in Fig. 6.9.

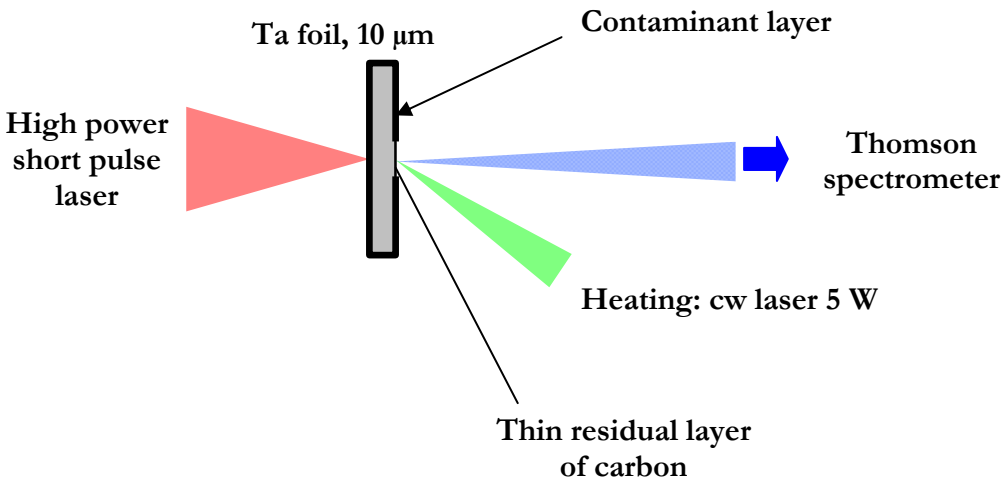

Fig. 6.9: The rear side of the target is irradiated by a 5 W continuous wave laser. The ion beam emitted from the rear side is analysed using a Thomson spectrometer.

The rear side of a 10 µm tantalum foil is irradiated by a 5 W continuous wave laser for a few minutes. Subsequently, a 320 fs beam with an energy of ~15 J irradiates the front side of the foil target. An ion beam is emitted from the rear side of the target. It is analysed using a Thomson spectrometer. In Fig. 6.10, the result of an experiment without heating is compared to the result after heating for 11 min.

From the unheated target, an ion beam consisting mainly of protons is emitted. All ions exhibit a broad energy spectrum. On the traces from the heated target, however, one can clearly see a

narrowing in the spectrum of the ions. A quasi-monoenergetic feature forms at a high energy. Protons are not visible at all.

This behaviour can be explained by the formation of a thin residual layer of carbon contaminants on the target surface. Such a phenomenon has been reported before by Hegelich et al. (cf. Section 3.2 or [54], respectively). In their experiment, the authors heated a palladium foil by passing a current through it (ohmic heating) and found quasi-monoenergetic features in the carbon ion beam emitted from the heated target. They attributed the formation of a thin carbon layer to the catalytic properties of palladium. This restricted the applicability of this method to catalytic material.

Although tantalum is not likely to show any catalytic behaviour on its surface, the formation of a quasi-monoenergetic feature is observed. A broad application is now possible.

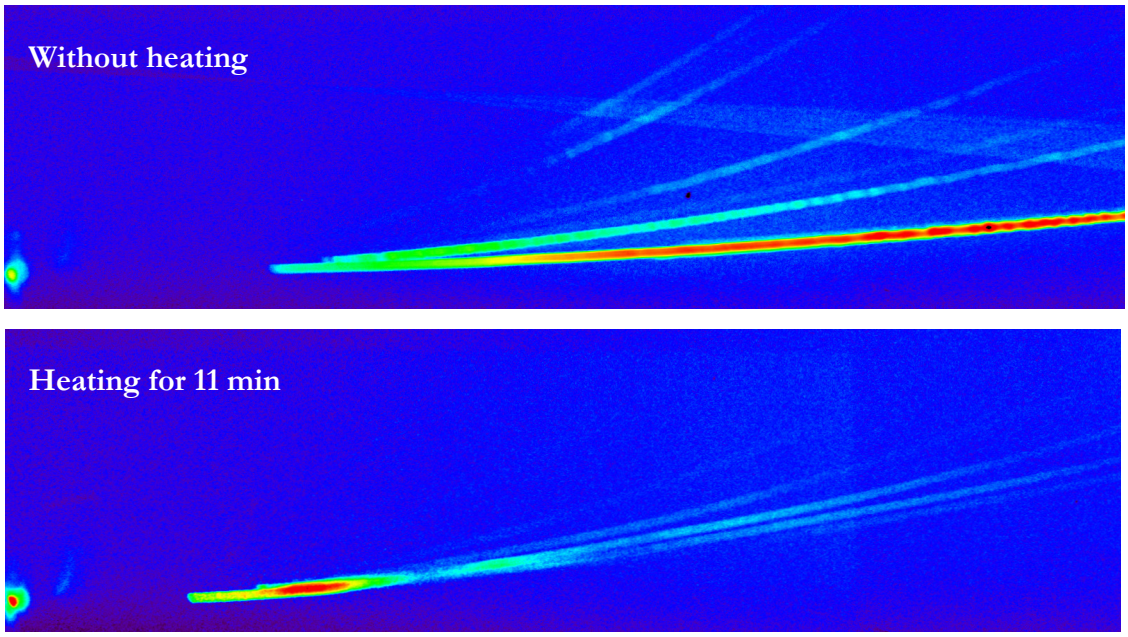

Fig. 6.10: The Imaging Plate readout from an experiment without heating compared to the result after heating for 11 min. Please note that the colour scale of the two images is different: The number of particles detected without heating is much higher than the number of particles detected after heating.

7 Analysing laser-generated plasmas using proton probing

This chapter provides insight into the physical processes that are connected to the generation and the control of laser-accelerated protons and other ions. Proton probing is employed to investigate the electric fields evolving in the vicinity of a laser-irradiated target.

7.1 Investigation of the electric fields in expanding plasmas

Beyond their role in the acceleration process itself, plasmas expanding from laser-irradiated targets play an important role in the control of the beam properties of laser-accelerated protons. The electric fields accompanying these plasmas can be used to displace, focus or collimate proton beams on the picosecond timescale (see Section 3.1). Using these fields to select a particular velocity class of protons, a quasi-monoenergetic spectrum can be obtained (see Section 3.2). Due to their transient nature, their strength and the high initial density of the expanding plasma, investigating these fields is not a trivial task.

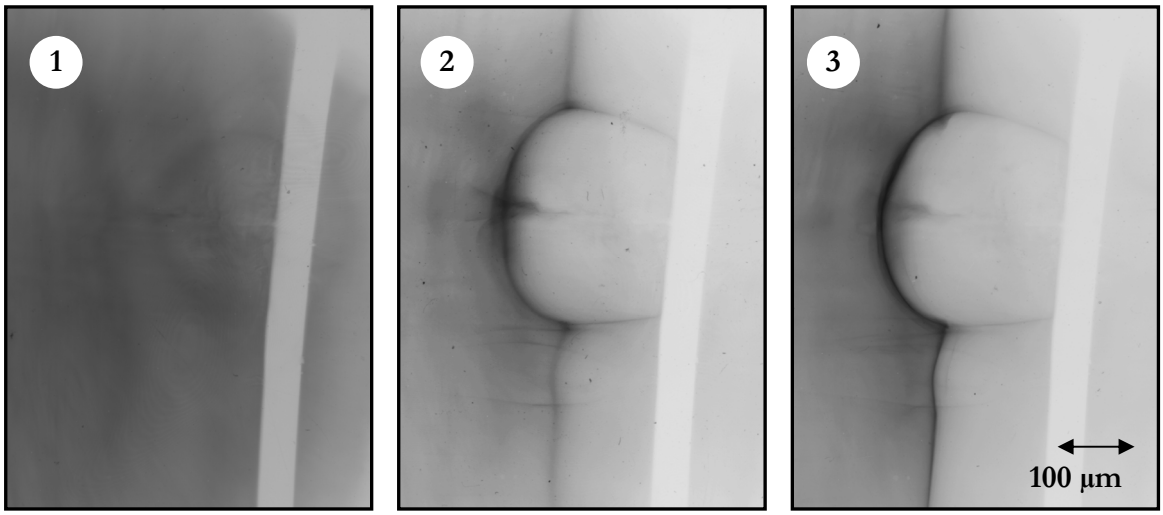

Fig: 7.1: A tantalum wire (diameter: 50 µm) is irradiated by a 10 J 400 fs laser and probed by a laser-generated proton beam. The RCF stack layers show snapshots of the temporal evolution of the irradiated wire. Please note that the radiochromic film showing the beginning of the interaction is an MD-55 type film and thus comprises two sensitive layers (see also Section 5.3). That is why it shows a superposition of two different times (0 ps/3.0 ps).

Our starting point will be the following experiment: A thin wire is irradiated by a short pulse laser and the electric field evolution in the vicinity of the wire is probed by a laser-accelerated proton beam. An RCF stack records the proton density distribution behind the wire. The result of such an experiment conducted at the LULI 100 TW laser is depicted in Fig. 7.1. The RCF stack layers show snapshots of the temporal evolution of the wire. Please mind that these pictures are not to be interpreted like shadowgraphs produced with light. The caustics that are clearly visible on films No. 2 and 3 are an effect of the deflection fields in the vicinity of the wire. These fields can be attributed to a plasma expansion around the laser-irradiated wire. One can easily see that this expansion spreads over the wire very fast and extends to an area of millimetres. The result of such an experiment is well-known for years. However, it is not very helpful in understanding the general behaviour of the plasma expansion fields. The experiment allows different interpretations. Caustics in the proton density distribution could also be attributed to a positive laser-induced charge up of the wire [99]. The experiments described in the following deliver a deeper insight into laser solid interaction.

Probing the plasma expansion on the rear side of a laser-irradiated target

The plasma expansion on the rear side of a laser-irradiated foil is investigated using a setup that resembles the one described in Section 5.2: The rear surface of a bent foil is probed with a laser-generated beam. The radius of the curvature of the foil and the observed region are larger than in the experiment presented by Romagnani et al. in [23]. Fig. 7.2 shows a schematic of the setup.

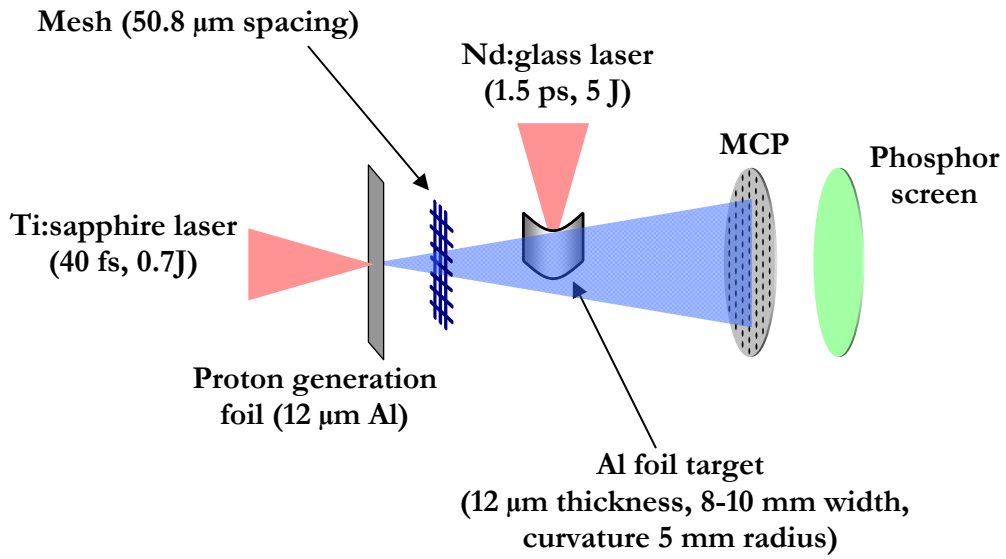

Fig. 7.2: Probing the rear surface of a laser-irradiated target using proton deflectometry.

The experiment was conducted at the *Max-Born-Institut* in Berlin, where two short pulse high power laser systems were available that could be synchronised with an accuracy of about 3 ps.

In the experiment, the MCP and the phosphor screen are gated in time, i.e. they are switched on and off. Gating the detector provides an energy selection of the protons used to probe the plasma expansion. Thus, the MCP can be used to take snapshots of the evolution of the plasma expansion. However, the gating time cannot be reduced arbitrarily. In this case the energy interval of the selected protons ranges from 1.4 MeV to 2.0 MeV. The result is depicted in Fig. 7.3.

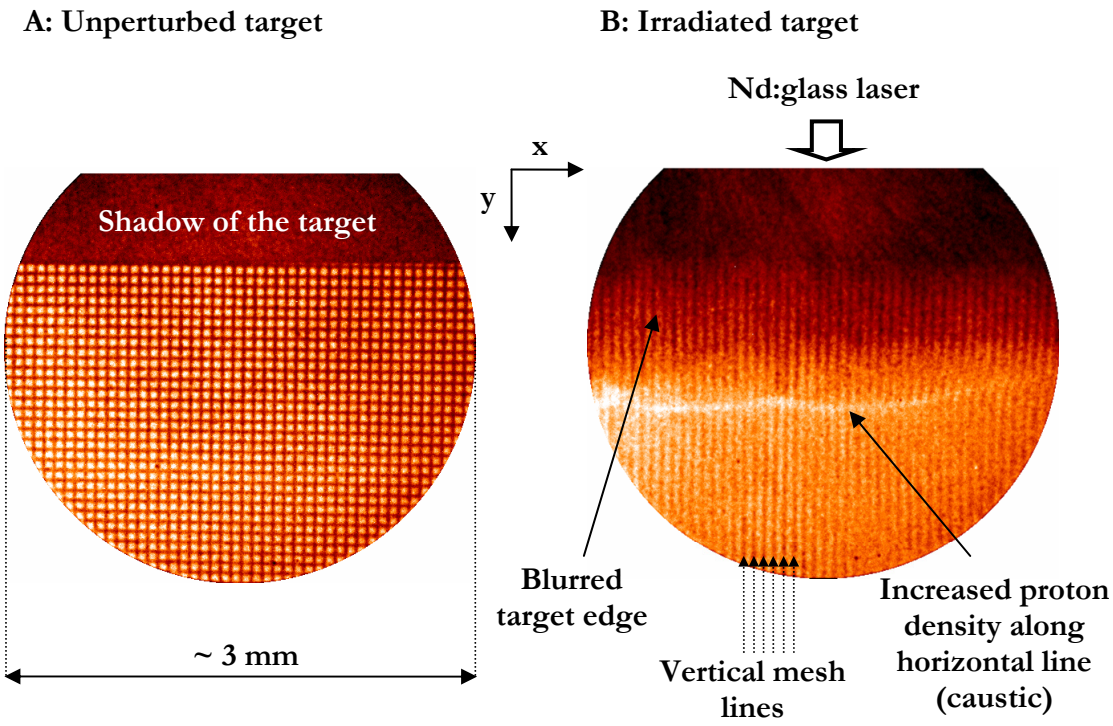

Fig. 7.3: A – The unperturbed target. The picture shows the shadows of the target and the mesh. An area with a diameter of about 3 mm is imaged. B – The target is irradiated by a 1.5 ps 5 J laser pulse. The shadow of the target edge is blurred in the y-direction and a horizontal line of an increased proton density is clearly visible. (Contrast enhanced in both images)

Fig. 7.3 A shows the image of the unperturbed target as a reference. The shadow of the mesh and the bent foil with its sharp edge are clearly visible. The detector records an image that corresponds to an area with a diameter of 3 mm at the target. In Fig. 7.3 B the target is irradiated by a 1.5 ps 5 J laser pulse. The laser irradiates the concave side of the target and the rear side of the target is imaged. The curvature of the foil and a thin (3 µm) Al filter in front of the MCP prevent direct laser light from disturbing the measurement. First of all, one can see that the target

edge is blurred downwards (i.e. in positive y-direction). The mesh is blurred in the same direction: The mesh lines along the y-direction are still visible, while the lines along the x-direction are wiped out. Furthermore, a horizontal line of an increase proton density is visible.

The blurring can be explained as follows: The proton deflection in the y-direction depends on their time-of-flight to the target. The detector integrates the signals of all protons within an energy range from 1.4 MeV to 2 MeV. The detector image is a superposition of all the proton images produced by the individual velocity classes of protons. From the result of this experiment, however, one cannot obtain information on the temporal dependence of the deflection.

The horizontal line of an increased proton density can be seen as a caustic similar to the one that is observed when probing a laser-irradiated wire (cf. Fig. 7.1). In this case however, this caustic cannot be attributed to a simple positive charge up of the target, since such a caustic can only be induced by an electric field that varies significantly along the y-direction: If the field decreases with increasing distance to the target surface, protons passing the target near by are deflected more than those passing the target in great distance. Thus, they can pile up along a line. In the case of a charged foil that is bent only slightly, the electric field can be assumed to be rather homogenous. Then, the deflection of the protons does not depend on their distance to the target surface. The effect of a homogenous electric field would be a displacement of the whole proton image on the detector, leaving the image itself unchanged.

Proton streak deflectometry

To investigate the temporal evolution of the electric field in the vicinity of the laser-irradiated target, proton streak deflectometry as described in Section 5.3 is applied. Therefore, a slit and a magnet are introduced into the proton beam. The setup is depicted in Fig. 7.4. The slit cuts out a cross section from the image depicted in Fig. 7.3 B. As indicated by Fig. 7.4, the cross section of the 2D image is cut out in the y-direction. After having passed the slit, the beam is dispersed with respect to the proton velocity along the x-axis. Fast protons are deflected less than slow protons. The cross section is therefore projected to an x-position on the detector that depends on the proton velocity. Since the velocity of the protons corresponds to their time of flight to the target, the x-axis on the detector corresponds to the time in the evolution of the cross section.

The mesh lines along the y-direction are parallel to the slit; they are blocked completely when the proton beam passes the slit. The mesh lines along the x-direction, however, are perpendicular to the slit. Let us first consider the case of a proton beam that is neither influenced by a deflection field nor by a target clipping parts of the beam. After having passed the slit, the profile of the

unperturbed proton beam looks like a dashed line, since it is interrupted by the shadow of the mesh lines in x-direction. This dashed line profile is now dispersed in the x-direction by the magnet; the individual dashes are dispersed to stripes that are recorded by the detector. If the target is inserted into the beam and irradiated by the second laser, the proton beam is deflected along the y-direction. Depending on the deflection field and its temporal evolution, the stripes on the detector appear shifted, widened or compressed.

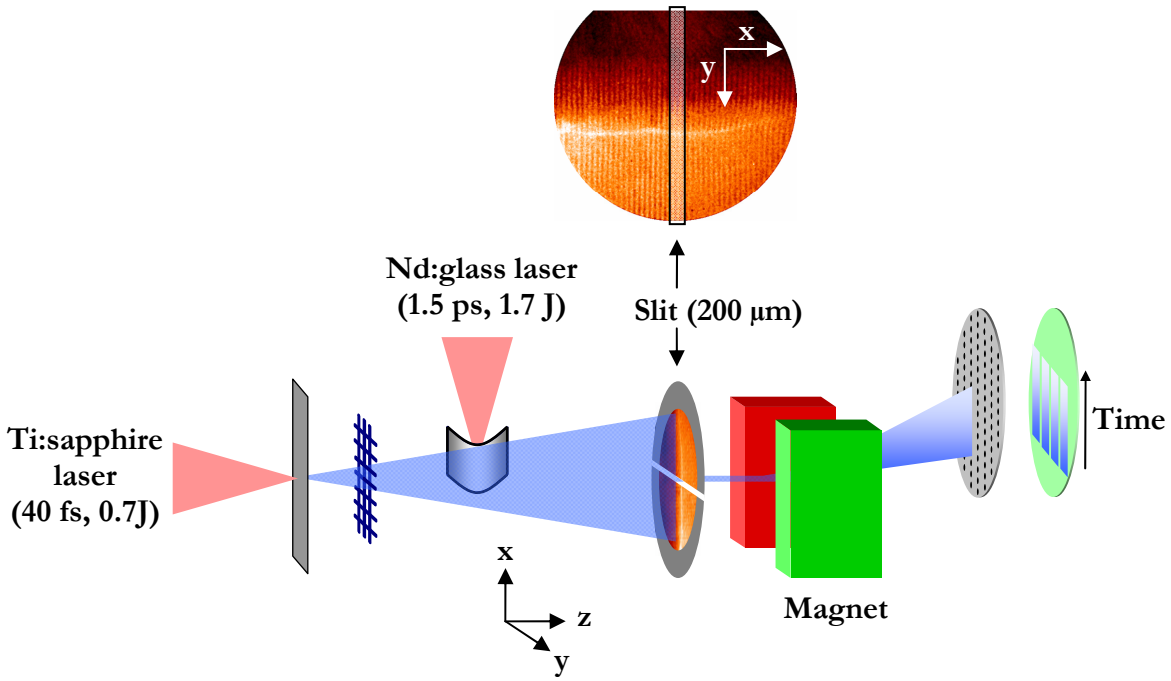

Fig. 7.4: Proton streak deflectometry – a magnet and a slit are added to the setup.

The result of the experiment is depicted in Fig. 7.5. The interaction starts with a strong and sudden deflection lasting for a short period of time as indicated by Δt_1. During this interval, the protons are piled up at the peak of the deflection and the stripes are compressed. A spot of an increased proton density is formed at the deflection peak. As indicated by the yellow dotted line, a perturbation moving away from the target is observed: The perturbation starts to be observable at the peak of deflection. As time proceeds, protons that pass the target in greater distance start to be influenced by the perturbation.

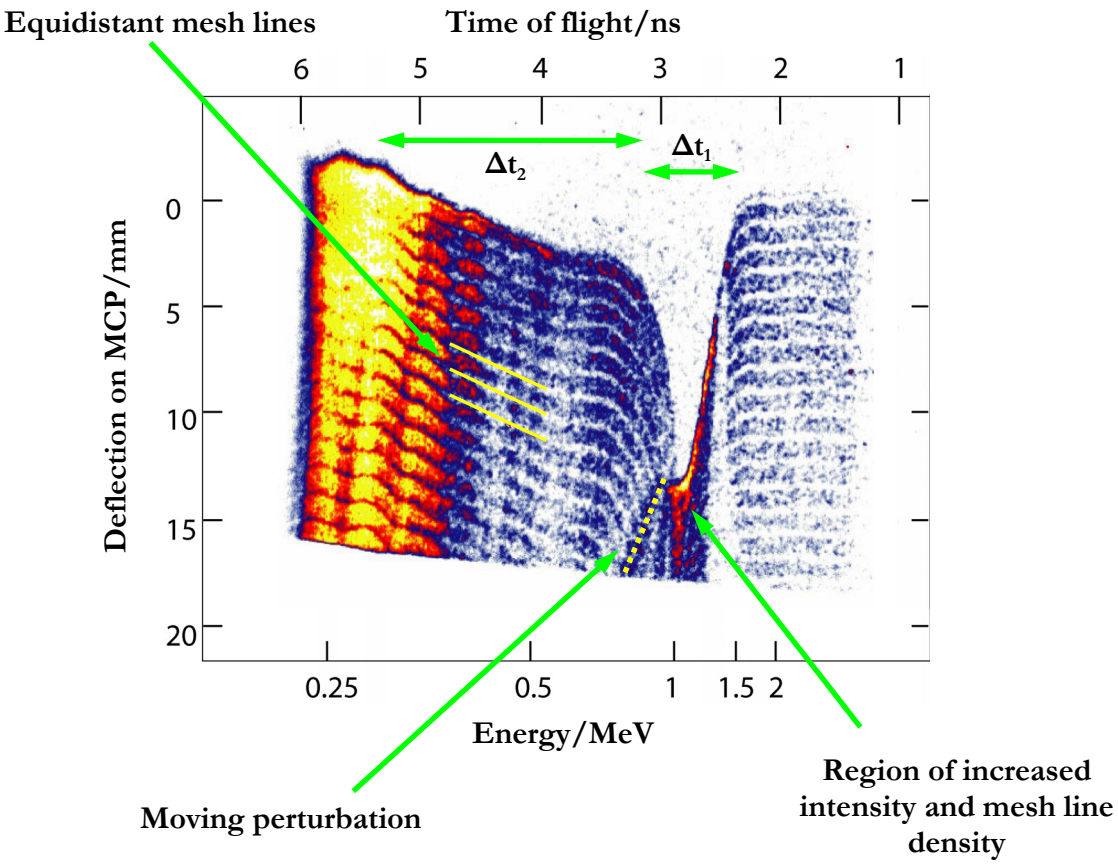

Fig. 7.5: Proton streak deflectometry image of the rear side of a laser-irradiated target (see also [8]).

The time interval Δt_1 is followed by a time interval Δt_2 that is dominated by a rather weak deflection that declines over a comparatively long time. During this time, the stripes are not compressed at all. The image is simply shifted in y-direction, i.e. away from the target.

The connection between the results observed in this experiment and those observed with two dimensional imaging (Fig. 7.3 B) can be explained as follows: Since proton streak deflectometry takes out a cross section from the two dimensional image, the bright horizontal line that can be seen in Fig. 7.3 appears as a bright spot in the proton streak deflectometry image depicted in Fig. 7.5. This is the region of increased proton density at the peak of the deflection. The assumption that the varying deflection is responsible for the blurring of the target edge and for wiping out the horizontal mesh lines in Fig. 7.3 B is confirmed by the observations in the proton streak deflectometry experiment.

Proton streak deflectometry simulation

To understand the physical processes causing the proton deflection measured in the experiment, the electric field in the vicinity of the laser-irradiated target is modelled. Due to the symmetry of the experiment, the influence of magnetic fields is assumed to be negligible.

When modelling the electric field in the proton streak deflectometry experiment, the laser-induced charge up of the target is taken into account: The laser interacting with the curved foil is supposed to accelerate electrons from the target. These electrons leave behind a positive net charge on the target. The laser-irradiated foil charges up positively on the picosecond timescale. Subsequently, the charge decays exponentially within hundreds of picoseconds. The target is curved only slightly and thus, the electric field caused by the positively charged target acts similar to a homogenous field. The field results in a deflection that does not depend on the distance to the target surface. The proton image is simply shifted and the spacing of the shadow lines of the mesh is constant. This can be observed during the slow decay of the deflection in the time interval that is marked as Δt_2 in Fig. 7.5.

The short deflection peak that appears during the time interval Δt_1, however, cannot be explained by a charge up of the target. The deflection strongly depends on the distance to the target surface: As indicated in Fig. 7.5, the strong deflection field piles up the protons at the deflection peak. This can be seen by the increase of the proton density at the peak and the reduced spacing of the shadow lines of the mesh. Furthermore, the deflection peak is much too narrow to be caused by a charge up field: The target is relatively large; it has a width of 8-10 mm. The protons need a certain time to travel along the target surface. That is why protons from a broad energy interval are located in front of the target *at the same time* and are influenced by the charge up field simultaneously.

The strong deflection occurring immediately after the laser incidence is attributed to a charge separation in a plasma expanding on the rear side of the target. The electric field in such an expanding plasma can be modelled as described in Section 2.3. The model describes the electric field in one dimension: A plateau region is followed by an exponential rise up to the peak of the electric field, which is in turn followed by a decay of the field. The peak is often called the *ion front* since the ions accelerated by electric field gather at the position of the peak. When the laser hits the target, the ion front starts at the target surface and propagates away from the target as the plasma expands into vacuum. The electric field decays rapidly while propagating; the energy of the field is transferred to the accelerated particles. The one dimensional model is applied to the three dimensional geometry of the target.

The electric field that accompanies the plasma expansion is superimposed by the charge up field. The charge up field is assumed to be screened by the electrons in the plasma expansion. In the model, it acts only between the target surface and the front.

The model is implemented into a particle tracing code. The code simulates the trajectories of individual protons in the geometry of the experimental setup. The simulated particles are collected by a virtual detector, and an image is rendered. This image can be compared to the experimental detector image. The particle tracer code developed in the framework of this thesis will be described in the appendix.

The model contains a set of parameters. The values of theses parameters can be varied to fit the simulation to the experimental result. After each simulation run, one of the parameters is changed to improve the fit. When the simulation agrees with the experiment, the set of simulation parameters contains information on the actual electric field. Fig. 7.6 shows the experimental result of the proton streak deflectometry experiment and the corresponding simulation. Fig. 7.7 shows the one dimensional field distribution at different times.

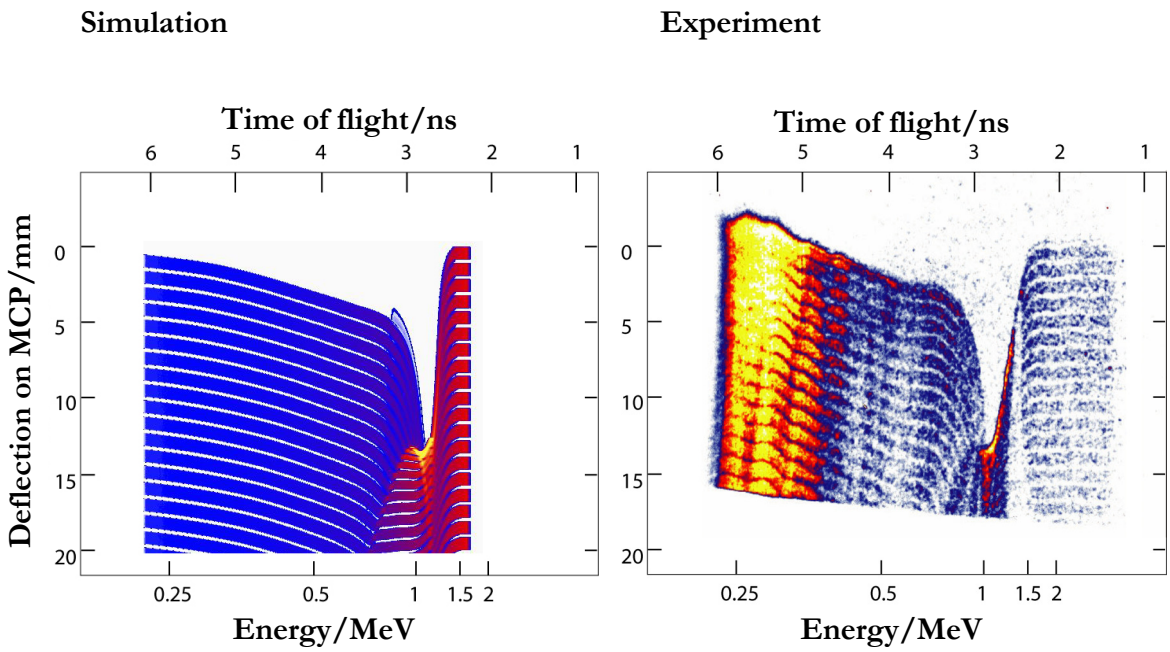

Fig. 7.6: Experiment and simulation: The main features of the experiment are reproduced (see also [8]).

A: Electric field evolution – plasma expansion

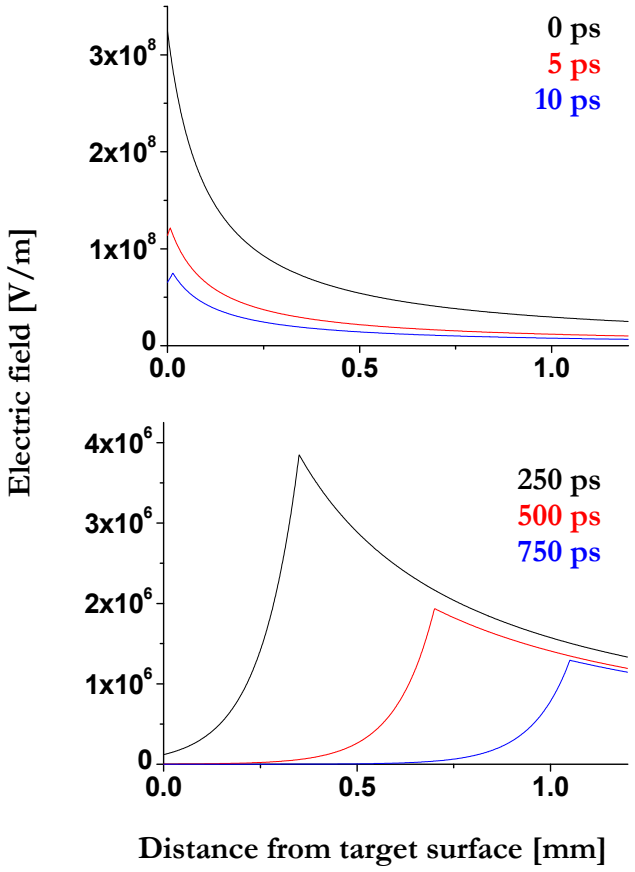

B: Electric field evolution – charge up

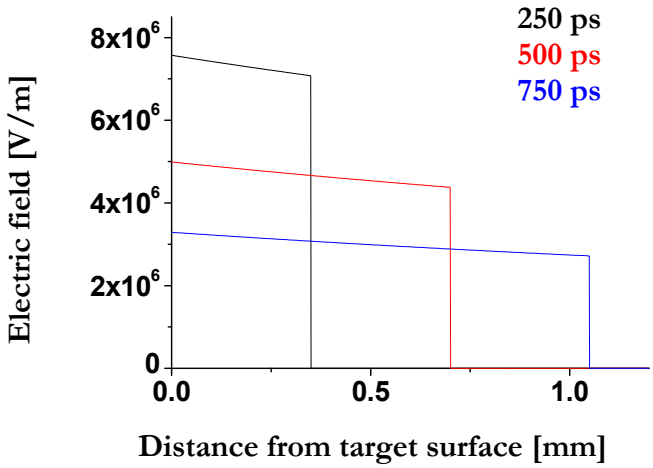

Fig. 7.7: Temporal evolution of the electric field in the simulation.

The main features of the experiment are reproduced. After fitting the simulation to the experimental result by varying the parameters of the model, the simulated evolution of the deflection is in good agreement with the experiment. The increase of the proton density at the peak and the reduced spacing of the shadow lines of the mesh are clearly visible. The maximum electric field is determined to be $3.8 \cdot 10^8$ V/m. At first, the field caused by the plasma expansion is dominant. This field decreases significantly within a few picoseconds and persists on a lower level over a period of several hundreds of picoseconds (cf. Fig. 7.7). The front leaves the observable region after about one nanosecond. Then, the field caused by the positive charge of the target becomes dominant. An areal charge density on the target of 10^{-4} C/m^2 and an exponential decay time of 600 ps are obtained from the simulation. The influence of perturbation moving away from the target (indicated by the dotted line in Fig. 7.5) is also reproduced in the simulation. The perturbation can now be interpreted as the electric field front. Each velocity class of protons encounters the front at a different distance from the target. The high energy protons encounter the front early, when it is still close to the target surface. The lower energetic protons encounter the front later, when it has already propagated away from the target. Using the propagation velocity of the front as a free parameter in the simulation, the front velocity from the experiment can be quantified. The fit yields a value of $1.4 \cdot 10^6$ m/s. This is far below the value predicted by the isothermal model described in Section 2.3 since this model inherently overestimates the propagation velocity of the front.

Plasma expansion on a laser-irradiated hollow metal foil cylinder

The plasma expansion on the outer surface of a laser-irradiated hollow metal foil cylinder is investigated using the setup depicted in Fig. 7.8. The experiment aims at an improved understanding of the plasma expansion and the electric fields accompanying the expansion in proton focussing experiments. The target is of the same kind as the cylinders that are used to focus laser-accelerated protons as described in Section 3.1 with an outer diameter of 810 μm, a wall thickness of 51 μm and a length of 3 mm. The material is Dural, an aluminium alloy (95% Al, 4% Cu, 1% Mg). The cylinder is probed using laser-accelerated protons. The images of the expanding plasma on the surface of the cylinder are recorded by an RCF stack detector as described in Section 5.3.

The cylinder is tilted by 45° in order to provide additional temporal information on the evolution of the plasma expansion on the target surface. To understand the way the temporal information is obtained, let us assume the plasma expansion to be cylinder-symmetrical. In this case, the electric field that accompanies the plasma expansion depends only on time and on the distance to

the symmetry axis of the cylinder. Let us now regard only one energy class of protons from the proton beam. Since the cylinder is tilted, a part of this monoenergetic bunch of protons arrives at the cylinder early – at the side of the cylinder closest to the proton source. The other parts of the monoenergetic bunch of protons arrive at the surface of the cylinder one after another. Thus, every part of the beam probes a different stage in the evolution of the expanding plasma. All protons of this energy class end up in the same layer of the radiochromic film stack detector. The layer shows an image of the plasma expansion whose early stage can be seen on one side of the cylinder and a more advanced stage can be seen on the other side of the cylinder. Thus, information on the temporal evolution of the plasma expansion is provided from the one side to the other side of the image.

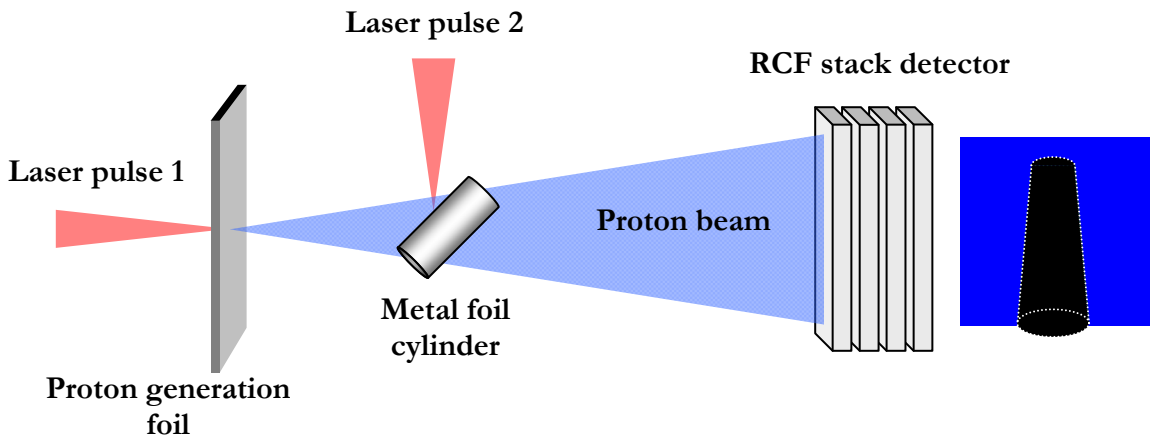

Fig. 7.8: A laser-irradiated hollow metal foil cylinder is probed. The cylinder is tilted by 45° to provide additional temporal information on the evolution on the plasma expansion of the target surface.

The experiment was conducted at the Rutherford Appleton Laboratory at the Vulcan TAW laser (see also Table 5.1). The beam was split into two parts, one part irradiating the proton generation foil, the other part irradiating the metal foil cylinder. The delay between the two pulses can be adjusted precisely by varying the optical path difference between the two pulses. The cylinder was irradiated by a focussed laser pulse of an energy of 20 J and a pulse duration of 1.2 ps. The result is depicted in Fig. 7.9. The beginning of the plasma expansion can be observed on the left side of the cylinder first, since this part of the cylinder has the greatest distance to the proton source. Every single detector image shows different stages of the plasma expansion, each covering a different time window.

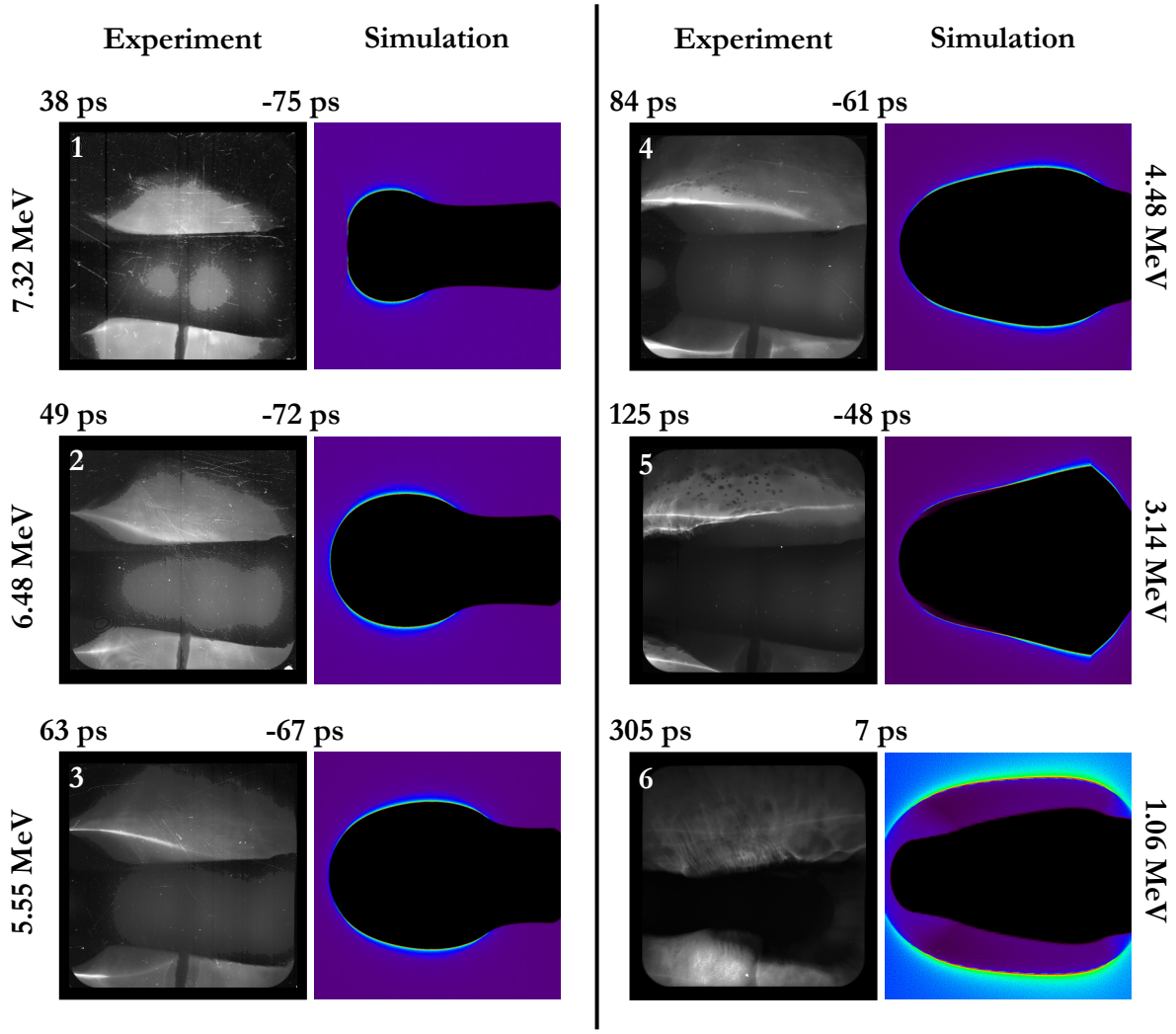

Fig. 7.9: Plasma expansion on the surface of a laser-irradiated metal foil cylinder: calibrated layers of the radiochromic film stack detector and the corresponding particle tracer simulation. The kinetic energy of the protons probing the expansion is given for each layer of the RCF stack. The time interval that is covered by each layer is displayed above the experimental result.

To model the electric field, the field configuration from the simulation described in the previous subsection was used. Parameters like the propagation velocity of the electric field front, that could only be determined using proton streak deflectometry, were transferred to the case of the laser-irradiated cylinder. Fig. 7.9 shows a comparison of the experimental data and the simulation. The simulation is in good agreement with the experiment. This shows the general applicability of the field scenario. The maximum electric field is determined to have a value of $1.1 \cdot 10^{10}$ V/m. At late times, filamentation occurs in the plasma in the vicinity of the cylinder. This, of course, cannot be explained by the model used in the simulation. A detailed discussion of the instabilities in the plasma of a laser-irradiated hollow metal foil cylinder can be found in [101].

The results show that the electric field model yields an adequate description of the plasma expansion in the experiments described in this section. The influence on the proton beam passing the laser-irradiated target is reproduced by the simulation. The model can now contribute to the design of new targets: For a given geometry, the evolution of the electric field in the vicinity of a laser-irradiated target can be obtained. Its effect on a proton beam can be predicted. Thus, a laser-irradiated target can be designed to influence a proton beam in a desired way. The proton beam could be displaced, collimated or focussed.

7.2 Imaging laser-irradiated water droplet targets

Water droplet targets have been shown to be the origin of quasi-monoenergetic proton and deuterium ion beams (see Section 3.2). The processes taking place when a water droplet is irradiated by a short pulse high power laser are still being discussed. The following experiment aims at the elucidation of theses processes. The setup is depicted in Fig. 7.10. A laser-irradiated water droplet is probed by a laser-generated proton beam. The MBI Ti:sapphire laser (cf. Table 5.1) is split into two beams. One beam irradiates the proton generation foil (a 5 µm titanium foil) with an intensity of 10^{19} W/cm^2 and a pulse duration of 40 fs. The other beam irradiates a single droplet from a water droplet jet with an intensity of $2 \cdot 10^{18}$ W/cm^2 and a pulse duration of 60 fs. The water droplet jet is generated by a commercial nozzle system [100]. The droplets have a diameter of 16 µm and a spacing of about 45 µm. The proton beam is detected by a micro-channel plate as described in Section 5.3. The magnification of the droplets is about 70-fold.

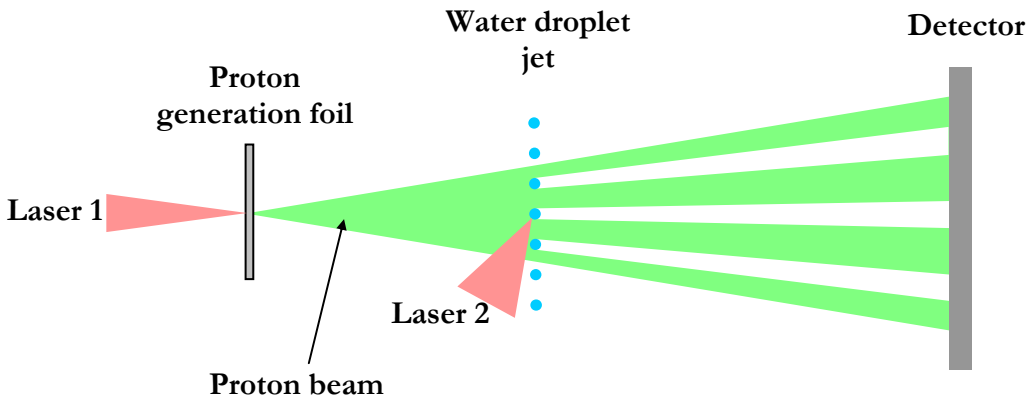

Fig. 7.10: A laser-irradiated water droplet is probed by a laser-generated proton beam.

A proton image of a laser-irradiated water droplet is depicted in Fig. 7.11. The laser irradiates the target from the left side. The shadow of the water droplet jet is clearly visible. The effect of the electric field in the vicinity of the laser-irradiated droplet can be observed as a ring-like increase of the detected proton density.

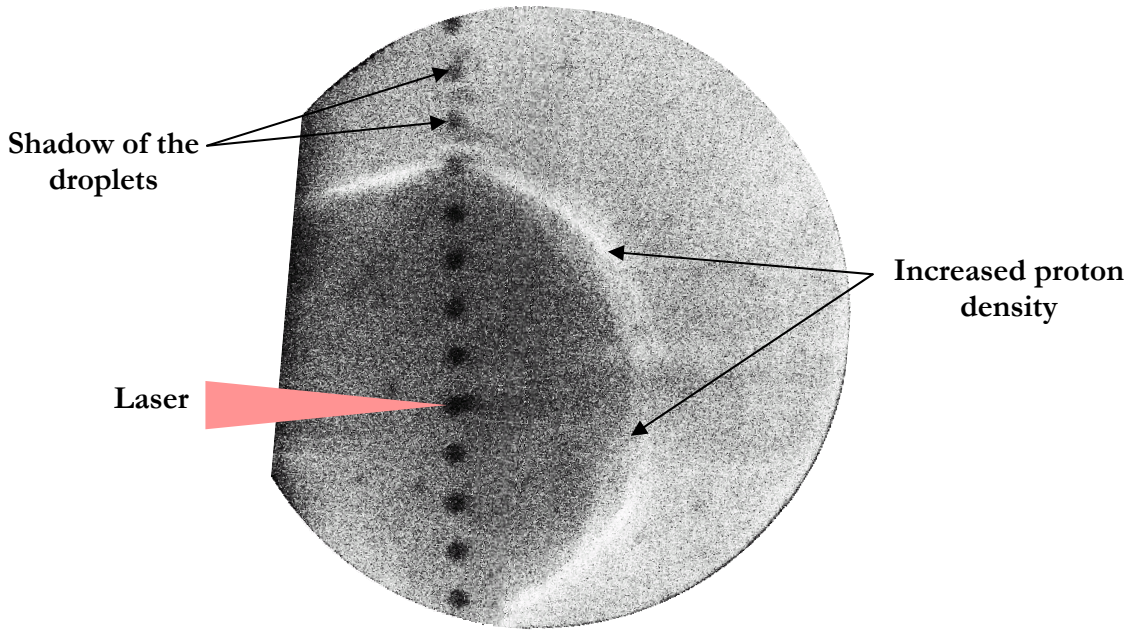

Fig. 7.11: Proton image of a laser-irradiated droplet. Contrast enhanced.

One can assume that the protons are deflected by an electric field that is caused by the positive charge-up of the laser-irradiated target. The setup is reconstructed in a particle tracing code. The droplets are assumed to be charged up on the picosecond time scale. The charge is assumed to decay exponentially. The decay time and the maximum charge can be obtained by fitting a one dimensional profile of the simulated proton density distribution to the corresponding profile of the experimental data (cf. Fig. 7.12 and Fig. 7.13). The maximum charge is determined to be $1.8 \cdot 10^{-10}$ C. The decay time is found to be about 75 ps. The decay time determined by this method is relatively short when compared to the one of a large target. For the large foil target investigated in Section 7.1 e.g., the decay time lay in the order of hundreds of picoseconds. This fast discharge of the droplet can be attributed to water vapour surrounding the water droplet jet. In vacuum, the gas is inevitably evaporated by the water droplets. The vapour can easily be ionised by the electric field and compensates the charge of the droplet subsequently.

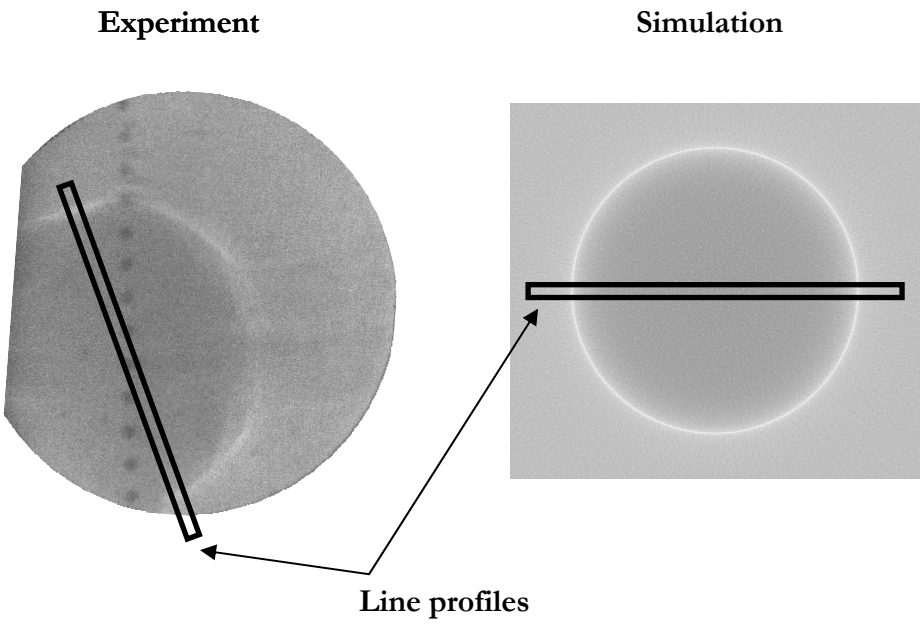

Fig. 7.12: Comparison of the experimental proton image and the simulated proton density distribution.

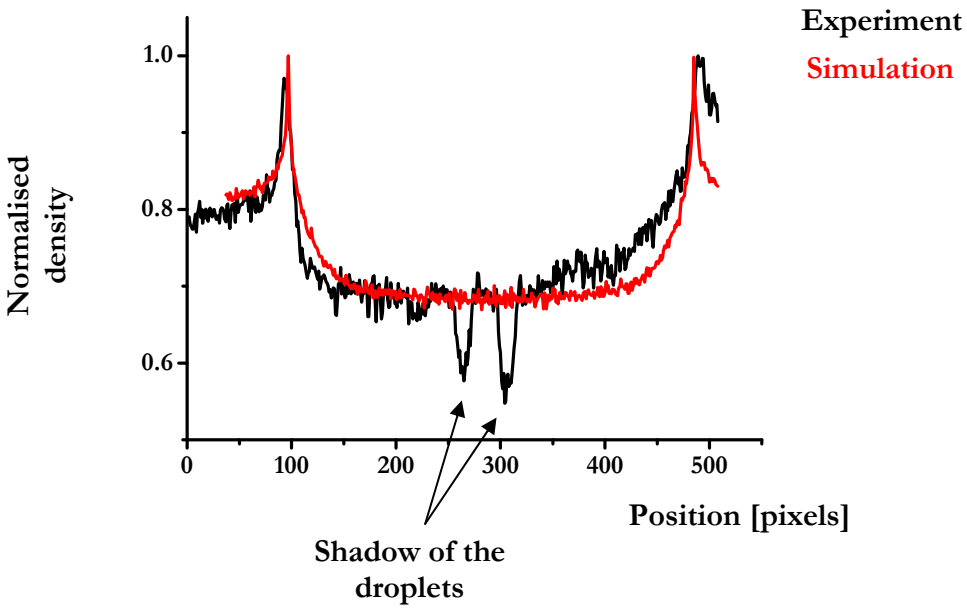

Fig. 7.13: Proton density line profiles taken from the experimental proton image and the simulated proton density distribution. By varying the charge decay time and the maximum charge of the droplet, the profile from the simulation can be fitted to the one obtained in the experiment.

The reproducibility of the experiment is limited since the exact position of the individual droplets cannot be controlled. When the laser pulse irradiates a droplet, it is uncertain whether the droplet is really centred in the focus of the beam or not. Therefore, the result differs from shot to shot. In addition to the halo around the laser-irradiated droplet that is visible in Fig. 7.11, an effect in the forward direction of the laser can be observed. Fig. 7.14 shows an example.

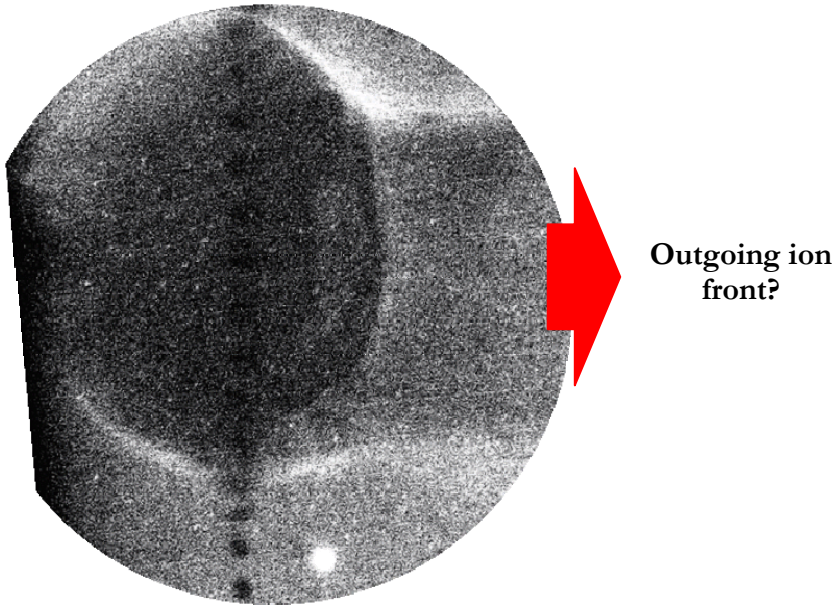

Fig. 7.14: Proton image of a laser-irradiated droplet including the effect in the forward direction of the laser. Contrast enhanced.

The feature in the proton image seems to correspond to an outgoing object deflecting the probe protons laterally. To clarify the relation of this phenomenon to the laser acceleration of protons from water droplets, the possibility of the formation of a laser-induced plasma expansion on the rear side of the target is investigated. It is not so obvious why such an expansion should originate only from the rear side of the droplet target. One could also imagine the electrons heated by the laser pulse to spread all over the surface of the droplet. But actually, this is not the case.

Fig. 7.15 shows the result of a PIC simulation of the beginning of a plasma expansion on a laser-irradiated water droplet. The electric field is not isotropic at all. It is clearly located on the rear side of the target.

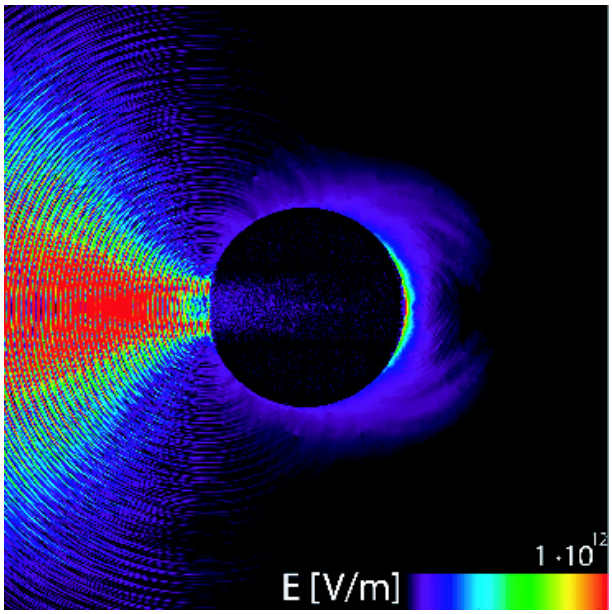

Fig. 7.15: PIC simulation – electric field distribution in the vicinity of a laser-irradiated water droplet 220 fs after the interaction peak. (Simulation conducted by Toma Toncian.)

A PIC simulation can cover only hundreds of femtoseconds. The proton image depicted in Fig. 7.14, however, is taken with protons ranging from 1.7 MeV to 2.0 MeV. This corresponds to a time interval of 65 ps. To simulate the processes in the experiment in this time interval, the evolution of the electric field is modelled and implemented into a particle tracer code. The electric field is a superposition of the charge up field from the simulation depicted in Fig. 7.12 and the plasma expansion field used in Section 7.1. The electron sheath is downscaled to the size of the droplets. Taking into account the oval shape of the halo around the laser-irradiated droplet visible in Figs. 7.11 and 7.14, the positive charge is assumed to be distributed over the laser-irradiated droplet and its neighbour droplets. Intensity plots of two dimensional cross sections of the electric field at different times are depicted in Fig. 7.16.

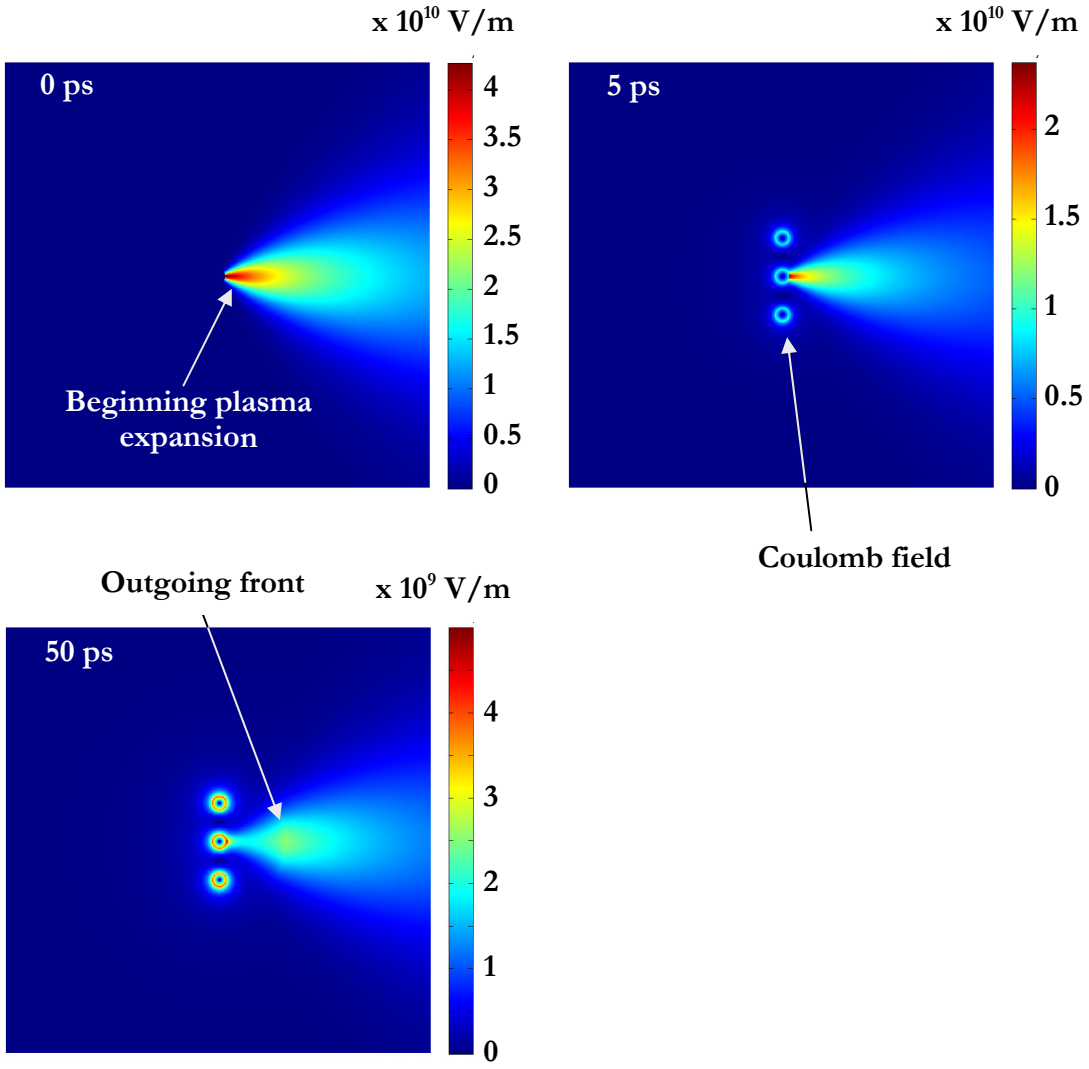

Fig. 7.16: Two dimensional cross sections of the modelled electric field at different times.

Fig. 7.17 shows a comparison of the experimental result and the corresponding simulated image. The shape of the halo caused by the positive charge up of the droplet is well reproduced in the simulation. The effect of the electric field that accompanies the plasma expansion is also clearly visible in the simulation: As in the experiment, a reduction of the proton density can be observed on the right side of the image. In the simulation, the reduction of the proton density shows a triangular shape. This is to be expected since the electric field front originates from a small object and propagates into space under a certain solid angle. In the experimental image, however, the boundaries of the area of a reduced proton density seem to be almost parallel. An additional effect like the incomplete neutralisation of the proton beam originating from the droplet seems to play a role. Further investigation is necessary to obtain a deeper understanding of this phenomenon.

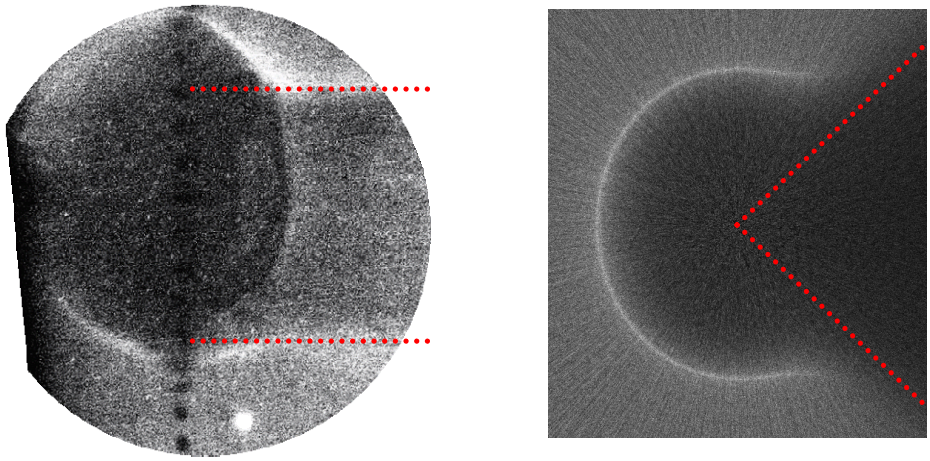

Fig. 7.17: Comparison of the proton image of a laser-irradiated droplet and the corresponding simulated image. A reduction of the proton density is visible on the right side of both images. The shape of this area is indicated by the red dotted lines.

8 Summary and outlook

Laser-accelerated protons and other ions offer a wide variety of appealing applications. To put these applications into practice, the properties of the laser-accelerated particle beams have to be controlled precisely. The present work approaches this task both by advancing the design of ion sources and by improving the understanding of the physical processes that accompany the laser acceleration of protons and heavier ions.

The performance of ion sources is tested experimentally. Experiments concerning mass-limited targets are conducted: Plain foil targets are used to investigate the influence of the target size on the properties of laser-accelerated proton beams. It is found that the reduction of the foil size leads to an increased number of accelerated particles and to a reduction of the beam divergence. In addition, the maximum proton energy is increased significantly. The observation is explained by established models describing the formation of the electric field that drives the proton acceleration. The advantages of mass-limited targets can only be exploited by the use of high contrast lasers. Due to the recent progress in laser development, commercial high contrast laser systems are now available. Size reduction of the targets is a simple way to improve the properties of laser-accelerated proton beams at theses laser systems.

Furthermore, carbon ion sources are investigated. Compared to protons, carbon ions offer considerable advantages for the production of warm dense matter and cancer radiotherapy. Both applications require beam focussing or collimation. Radiotherapy additionally requires a monoenergetic beam. A proton focussing technique is transferred to carbon ions: The possibility of focussing a laser-accelerated carbon ion beam using a laser-irradiated hollow metal film cylinder is investigated. Difficulties are encountered and attributed to the low carbon ion flux that was available in this experiment. New acceleration techniques such as the use of mass-limited targets have the potential to generate significantly higher amounts of carbon ions at higher energies. As soon as improved carbon ion beams are available, carbon ion focussing using a laser-irradiated hollow metal foil cylinder is likely to become feasible.

It is shown experimentally that heated targets without any catalytic surface properties can be a source of quasi-monoenergetic carbon ions. This is attributed to the formation of a thin residual carbon contaminant layer on the surface of the targets. Not being restricted to a particular material, a broad application of this method is now possible.

This thesis also provides an insight into the physical processes connected to the production and the control of laser-accelerated ions. For this purpose, laser-accelerated protons are employed to probe plasma phenomena on laser-irradiated targets. The electric field in the expanding plasma on the rear side of a laser-irradiated foil is probed using proton streak deflectometry. Simulations based on a model of the electric field are conducted in order to determine the spatial and temporal evolution of the field. The propagation of an electric field front is observed and its propagation velocity is determined. These results are used to interpret another experiment: The plasma expansion on the surface of a laser-irradiated hollow metal foil cylinder is imaged using laser-accelerated protons. The model is applied to this target geometry and the electric field evolution is reconstructed in simulations. The results show that the model used to interpret the experiments is valid under the given experimental conditions. It can now be used for the design of new targets: The electric field accompanying the plasma expansion can be predicted for a given target geometry. A secondary laser-irradiated target can be designed to influence a proton beam in a desired way – the electric fields can be used to displace, collimate or focus laser-accelerated proton beams.

In previous work, laser-irradiated water droplet targets could be shown to be the origin of quasi-monoenergetic protons and deuterons. These mass-limited targets are investigated using proton imaging. The laser-induced charge up of the droplets is discussed. The charge decay time is determined. The charge decay time sheds light on the degree to which a droplet can be considered to be isolated. A structure on the rear side of the laser-irradiated droplet is observed. The possibility to attribute this structure to an outgoing electric field front is discussed. An improved understanding of these phenomena could contribute to the elucidation the processes involved in the laser generation of quasi-monoenergetic proton beams from droplet targets.

In the framework of this thesis, significant progress could be achieved in the control of laser-accelerated proton and carbon ion beams. There is still work to be done to realise the appealing future applications of these beams. But after all, we are on the right path.

Appendix A: Particle tracing

A particle tracer is a computer simulation program that calculates the path of individual particles through a given virtual environment. In our case, the simulated particles are protons or heavier ions and the given virtual environment is a replica of an experimental setup. Electric and magnetic fields influencing the path of the particles and solid objects blocking the path of the particles need to be taken into account. The trajectories of the particles are calculated by standard methods: The initial conditions of each particle are given. If the electric and the magnetic field are given by a model as described in Section 2.3, they can be calculated analytically for each position and time. If the fields are inferred from PIC-simulations, they are implemented in the particle tracer on a spatial and temporal grid. An integrator performs a stepwise calculation of the particle trajectory.

A particle beam can be simulated calculating a number of particles. The initial conditions of these particles reproduce the properties of a real particle beam (such as energy distribution or solid angle of emission). After having been traced through the virtual experimental setup, the particles can be collected by a virtual spectrometer or detector. As soon as all particles are collected, the program renders a detector image that corresponds to the image detected in the experiment.

If an experiment is analysed as described in Section 7.1, the fields influencing the path of the particles are modelled analytically. The model contains a set of parameters whose values can be varied to fit the simulation to the experimental result. After a simulation run, one of the parameters is changed to improve the fit. The procedure is repeated until the simulation agrees with the experiment. This iterative method requires a lot of simulation runs to analyse only one experiment. The result of the simulation needs to be compared to the experiment by eye since a computer program cannot easily recognise structures caused by a physical effect or distinguish a signal from an experimental artefact. That is why the simulation code has to provide acceptable results on a simple PC within minutes. Only few particles can be simulated and from these few particles, a complete detector image needs to be rendered.

Fig. A.1 shows the principle of an interpolation technique that is able to reconstruct a complete detector image from few simulated particles.

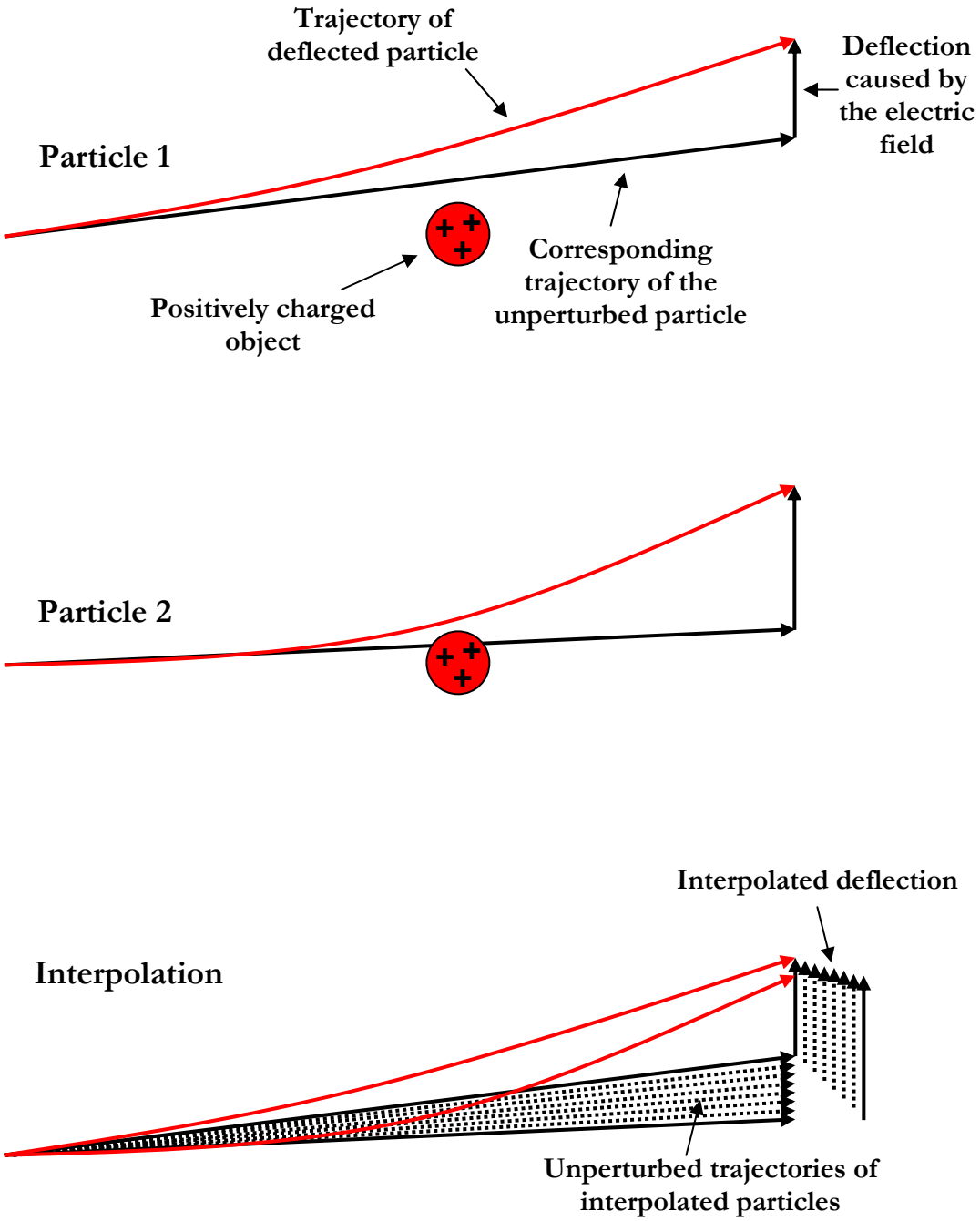

Fig. A.1: One dimensional illustration of an interpolation scheme for particle tracing.

Imagine a particle that is not influenced by any kind of field or obstacle. Knowing the initial conditions of the particle, the position where it hits the detector can easily be calculated. If the same particle is deflected by a field, it will hit the detector at another position. The (vectorial) difference can be seen as the deflection caused by the field. Let us add a second particle emitted under another angle. If the field is again imagined to be switched off, the two particles will hit the detector at different positions. If the field is switched on, the particles will also show a different

deflection. This deflection is now interpolated with respect to the position where the unperturbed particle would have hit the detector. This can be illustrated by the following example: The detector position of two particles is already known – both for the field-free case and the case of particle deflection. We now consider a third particle in the field-free case that ends up directly in the middle of the first two particles. When the field is active, we can assume the third particle to experience a deflection corresponding to the mean value of the deflections of particles 1 and 2. The final position of particle 3 can be estimated without calculating its trajectory explicitly. In this way, a large number of particles can be interpolated within a short time. Having calculated the detector position of an amount of particles that might be even as large as in the experiment, a simulated detector image that resembles the experimental one can be rendered. This interpolation scheme is to some degree equivalent to algorithms implemented in computer graphic cards and yields good results. However, it relies on the assumption that there is a linear relation between a small change in the final position of a particle in the field-free case and the change of the particle deflection caused by the field. This lacks a clear physical motivation. A similar, but more accurate interpolation scheme is obtained if one assumes a linear relation between a small change in the initial conditions of a particle and the change in its final position and momentum. Since there is no chaotic behaviour to be expected when using an analytical field model, this assumption is reasonable. In contrast to the scheme that interpolates particle deflections, the interpolation scheme based on initial conditions automatically includes the interpolation of particles with different energies.

Another problem particle tracers have to face is the presence of solid objects in the path of the beam. These objects absorb or scatter particles and thus, they produce a shadow onto the detector. If there is no deflection field, this shadow can simply be calculated by mathematical projection. But since it is usually a deflection field that is to be studied with the particle tracer, this method is hardly applicable.

If an object is situated between the particle source and the region of the deflection field, it is known in advance, which particle will pass the object and which particle will be absorbed. Then, only those particles that will pass the object are simulated. This method is applied to meshes used in proton deflectometry as described in Section 5.2. The mesh intersects the whole proton beam into many individual beams with a quadratic profile. Only these small beams are simulated; the particles that hit the bars of the mesh are neglected.

If the object is located in the region of the deflection field, the situation is more complicated. This is the case for a laser-irradiated solid state target, e.g. Then, the objects need to be scanned

by the simulated particle beam. As mentioned above, only few particles can be simulated in a simulation run. Therefore, the resolution of the scan is usually much lower than the resolution of the virtual detector. Consequently, aliasing occurs. Fig. A.2 shows a simulated proton image of a tilted cylinder as described in Section 7.1.

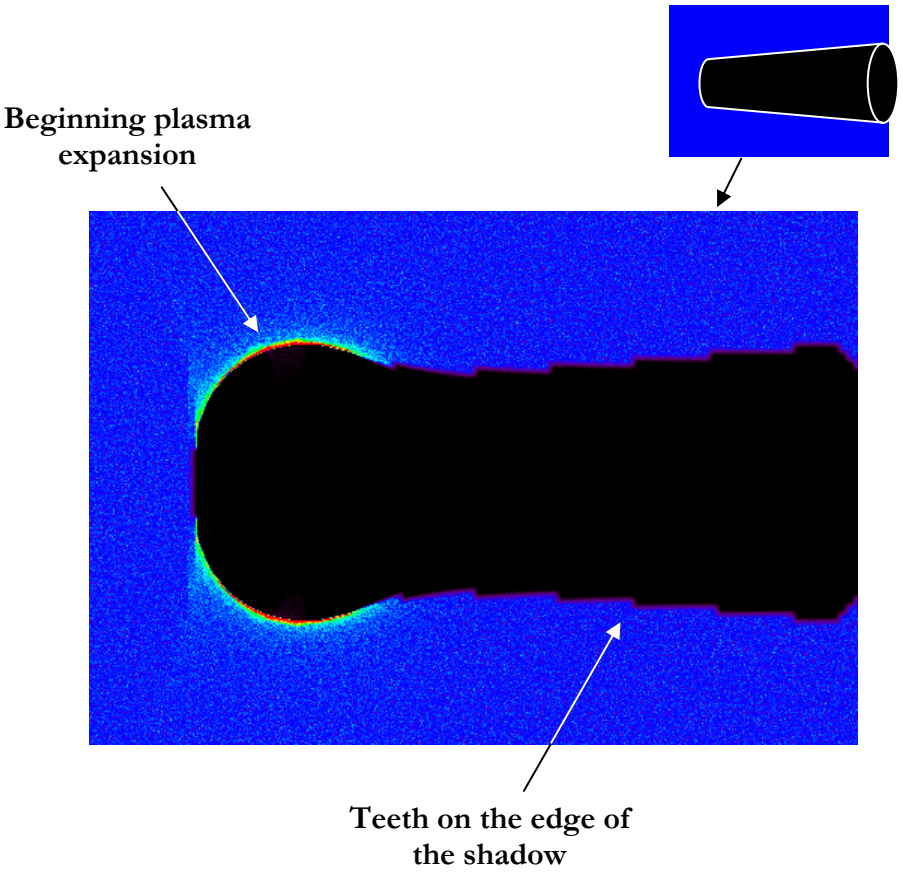

Fig. A.2: Shadow of a tilted cylinder showing aliasing.

On the edge of the shadow, teeth appear as a consequence of the low resolution of the particle scan. To obtain a more realistic image, an anti-aliasing technique is applied: A new property is attributed to the probe particles – a value that can be interpreted as brightness. If a simulated particle passes the cylinder nearby, its brightness is reduced and the spot that the particle creates on the detector is fainter than the one of a particle that passes the cylinder in great distance. A particle that penetrates the object near its surface is not dimmed completely. A particle that deeply penetrates the object becomes black. Fig. A.3 illustrates this technique.

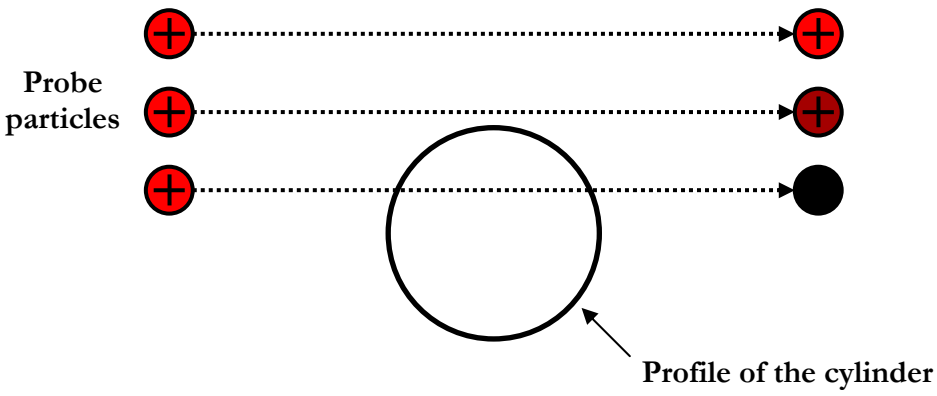

Fig. A.3: Anti-aliasing – the brightness of the probe particles passing the cylinder nearby is reduced.

For the interpolated particles, the brightness is also interpolated. Fig. A.4 shows the result of the anti-aliasing. The edge of the shadow appears smooth and thus much more realistic. Yet, the edge appears a bit blurred, an effect that is well-known from anti-aliasing in computer graphics. Figs. A.2 and A.4 represent examples for one step in the iterative method described above. Once the values of all parameters are determined, the number of simulated particles can be increased to obtain a better resolution. In Fig. 7.9 from Section 7.1 for example, almost no blurring of the edge of the shadow is visible.

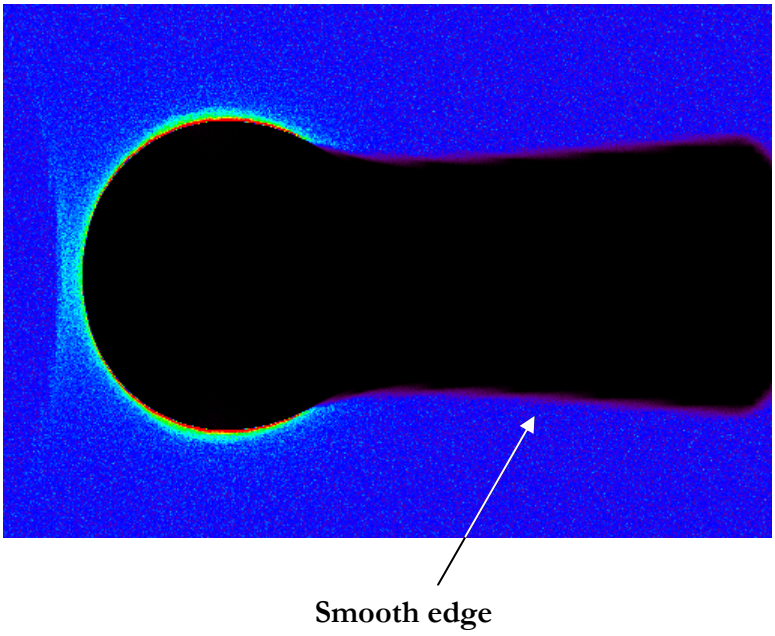

Fig. A.4: Anti-aliasing – the edge of the cylinder appears smooth. (In this picture, the plasma expansion has proceeded a bit with respect to Fig. A.2. This is not an effect of the anti-aliasing.)

Appendix B: The production of thin dot targets

As described in Section 3.2, quasi-monoenergetic proton beams have been reported to originate from metal foil targets with a small dot on the rear side. The dot contained the protons that were to be accelerated. The dots used in that experiment were relatively thick (~500 nm) – there is no longitudinal limitation of the layer. As mentioned in Section 3.2, there is no simple explanation for the occurrence of quasi-monoenergetic protons without a longitudinal limitation of the acceleration zone. To investigate the influence of dot thickness and size and to extend the experiment to carbon ions, thin carbon dots are coated onto metal foil targets: First of all, a template is manufactured. A femtosecond laser is used to bore holes of different sizes into a 50 µm copper foil. Subsequently, individual tantalum foil targets are clamped onto a carrier. The template is clamped onto the targets. A spacer prevents the template from being in direct contact to the target surface. The assembly is then inserted into a vacuum evaporator. In the evaporator, carbon sublimates from a heated sample. The carbon atoms fly ballistically to the target assembly. On the tantalum targets, a coating in the shape of the holes of the mask is formed. The targets are exposed to the carbon vapour until the desired layer thickness is attained. The thickness may range from few atomic layers to about 250 nm. Fig. B.1 shows a photograph of a small dot.

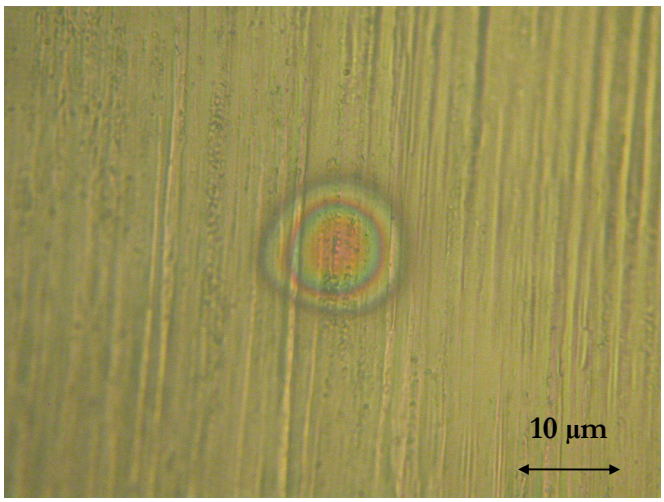

Fig. B.1: Photograph of a carbon dot on a tantalum target. The picture shows the interference colours of the coating that is about 250 nm thick.

To use these targets in experiments, different problems need to be solved:

- Alignment: A dot of a few nanometres thickness is hardly visible. An alignment procedure that facilitates the positioning of the dot in the laser acceleration experiment is to be developed.

- Surface roughness: Atomic force microscope measurements showed that the surface roughness of the tantalum foil lies in the order of 200 μm. On such a surface, a uniform deposition of the carbon coating cannot be guaranteed. Although high surface quality foils are available, their applicability needs to be investigated.

- Heat resistivity: To get rid of the proton contaminants, the dotted target is heated as described in Section 6.2. Unfortunately, the coating is not able to withstand a high temperature since carbon shows a low adhesion on a metal substrate. Another way of cleaning the target or a more heat resistive compound needs to be conceived.

Acknowledgements

First of all, I would like to thank Prof. Oswald Willi for supporting me during the time that I worked towards my Ph.D. degree in his group. He gave me the opportunity to broaden my horizon and encouraged me to realise my ideas. I also would like to thank my colleagues from the Institute of Laser and Plasma Physics and from the research training group GRK1203 for endless discussions about experimental setups, computer simulations, plasma physics phenomena and other topics and for the fun that we had during this time. In particular, I would like to thank Toma Toncian for close collaboration in the field of laser-accelerated protons and heavier ions.

I also would like to thank Claudia Dingle, Christiane Braun and Renate ter Horst for organisational support. Without their help, I probably would have spent most of my time with administrative work.

Christof Bolten, Helmut Borrmann, Andreas Karmann, Stefan Manderla and Werner Sigosch provided technical support. Their creativity in solving technical problems was extremely helpful.

I would like to thank the teams of the experiments and their leaders for good collaboration – even under difficult conditions: Patrick Audebert, Julien Fuchs, Ana Mancic, Livia Lancia, Sébastien Buffechoux and Patrizio Antici from the LULI at the École Polytechnique, Marco Borghesi, Carlo A. Cecchetti, Puthenparampil Wilson, Gianluca Sarri and Lorenzo Romagnani from the School of Mathematics and Physics at the Queen's University Belfast, Prof. Wolfgang Sandner, Peter V. Nickles, Matthias Schnürer, Thomas Sokollik and Sargis Ter-Avetisyan from the Max-Born-Institut Berlin, Prof. Ryosuke Kodama and Motonobu Tampo from the Institute of Laser Engineering, Osaka University, Prof. Thomas Cowan, Trevor Burris and Karl Zeil from the Forschungszentrum Dresden-Rossendorf, Prof. Markus Roth, Marius Schollmeier, Frank Nürnberg and Knut Harres from the Gesellschaft für Schwerionenforschung Darmstadt and, of course, Prof. Oswald Willi, Toma Toncian and Ariane Pipahl from our institute. There was a fruitful collaboration with the Prof. Thomas Heinzel's group from the Condensed Matter Physics Laboratory at our university. Mihai Cerchez and Stefan Hugger worked overtime to help me in the production of layered targets. I would like to thank the experimental team of the first carbon ion focussing experiment including Prof. Manuel Hegelich for providing me the data from this experiment that I could not participate in. I also would like to mention that the experiments

conducted in the framework of this thesis would have been impossible without the help of the engineers and technicians at the laser facilities.

I thank Emanuel d'Humières and Toma Toncian who conducted the PIC simulations used in this work.

This work was conducted in the framework of the DFG research training group GRK1203. My work also benefited from collaboration with the A6 project of the DFG SFB TR18. The experiments conducted at the LULI, École Polytechnique, and at the Rutherford Appleton Laboratory were funded Laserlab Europe.

I would like to thank my family for support. In particular, I thank my wife for encouraging me constantly during the time that I worked towards my Ph.D. degree.

Bibliography

[1] S.J. Gitomer, R.D. Jones, F. Begay, A.W. Ehler, J.F. Kephart and R. Kristal, *Fast ions and hot electrons in the laser–plasma interaction*, Phys. Fluids **29**, 2679 (1986).

[2] R.A. Snavely, M.H. Key, S.P. Hatchett, T.E. Cowan, M. Roth, T.W. Phillips, M.A. Stoyer, E.A. Henry, T.C. Sangster, M.S. Singh, S.C. Wilks, A. MacKinnon, A. Offenberger, D.M. Pennington, K. Yasuike, A.B. Langdon, B.F. Lasinski, J. Johnson, M.D. Perry and E.M. Campbell, *Intense High-Energy Proton Beams from Petawatt-Laser Irradiation of Solids*, Phys. Rev. Lett. **85**, 2945 (2000).

[3] A. Maksimchuk, S. Gu, K. Flippo, D. Umstadter and V.Yu. Bychenkov, *Forward Ion Acceleration in Thin Films Driven by a High-Intensity Laser*, Phys. Rev. Lett. **84**, 4108 (2000).

[4] E.L. Clark, K. Krushelnick, J.R. Davies, M. Zepf, M. Tatarakis, F.N. Beg, A. Machacek, P. A. Norreys, M.I.K. Santala, I. Watts and A.E. Dangor, *Measurements of Energetic Proton Transport through Magnetized Plasma from Intense Laser Interactions with Solids*, Phys. Rev. Lett. **84**, 670 (2000).

[5] S.P. Hatchett, C.G. Brown, T.E. Cowan, E.A. Henry, J.S. Johnson, M.H. Key, J.A. Koch, A.B. Langdon, B.F. Lasinski, R.W. Lee, A.J. Mackinnon, D.M. Pennington, M.D. Perry, T.W. Phillips, M. Roth, T.C. Sangster, M.S. Singh, R.A. Snavely, M.A. Stoyer, S.C. Wilks and K. Yasuike, *Electron, photon, and ion beams from the relativistic interaction of Petawatt laser pulses with solid targets*, Phys. Plasmas **7**, 2076 (2000).

[6] M. Borghesi, A.J. Mackinnon, D.H. Campbell, D.G. Hicks, S. Kar, P. K. Patel, D. Price, L. Romagnani, A. Schiavi and O. Willi, *Multi-MeV Proton Source Investigations in Ultraintense Laser-Foil Interactions*, Phys. Rev. Lett. **92**, 055003 (2004).

[7] T.E. Cowan, J. Fuchs, H. Ruhl, A. Kemp, P. Audebert, M. Roth, R. Stephens, I. Barton, A. Blazevic, E. Brambrink, J. Cobble, J. Fernández, J.-C. Gauthier, M. Geissel, M. Hegelich, J. Kaae, S. Karsch, G.P. Le Sage, S. Letzring, M. Manclossi, S. Meyroneinc, A. Newkirk, H. Pépin and N. Renard-LeGalloudec, *Ultralow Emittance, Multi-MeV Proton Beams from a Laser Virtual-Cathode Plasma Accelerator*, Phys. Rev. Lett. **92**, 204801 (2004).

[8] T. Sokollik, M. Schnürer, S. Ter-Avetisyan, P.V. Nickles, E. Risse, M. Kalashnikov, W. Sandner, G. Priebe, M. Amin, T. Toncian, O. Willi and A.A. Andreev, *Transient electric fields in laser plasmas observed by proton streak deflectometry*, Appl. Phys. Lett. **92**, 091503 (2008).

[9] P.V. Nickles, M. Schnürer, T. Sokollik, S. Ter-Avetisyan, W. Sandner, M. Amin, T. Toncian, O. Willi and A. Andreev, *Ultrafast laser-driven proton sources and dynamic proton imaging*, J. Opt. Soc. Am. B, **25**, B155 (2008).

[10] M. Borghesi, C.A. Cecchetti, T. Toncian, J. Fuchs, L. Romagnani, S. Kar, P.A. Wilson, P. Antici, P. Audebert, E. Brambrink, A. Pipahl, M. Amin, R. Jung, J. Osterholz, O. Willi, W. Nazarov, R.J. Clarke, M. Notley, D. Neely, P. Mora, T. Grismayer, G. Schurtz, A. Schiavi, Y. Sentoku and E. d'Humières, *Laser-Driven Proton Beams: Acceleration Mechanism, Beam Optimization, and Radiographic Applications*, IEEE T. Plasma Sci. **36**, 1833 (2008).

[11] J.D. Lawson, *Lasers and Accelerators*, IEEE Trans. Nucl. Sci. **26**, 4217 (1979).

[12] C. Smith and M.N. Wise, *Energy and Empire: A Biographical Study of Lord Kelvin*, Cambridge University Press, Cambridge (1989).

[13] P. Gibbon, *Short Pulse Laser Interactions with Matter – An Introduction*, Imperial College Press, London (2005).

[14] M.C. Kaluza, *Characterisation of Laser-Accelerated Proton Beams*, Dissertation, TU München (2004).

[15] H. Stöcker, *Taschenbuch der Physik – Formeln, Tabellen, Übersichten*, 5th edition, Wissenschaftlicher Verlag Harri Deutsch, Frankfurt am Main (2004).

[16] J. Meyer-ter-Vehn, A. Pukhov and Zh.M. Sheng, *Relativistic Laser Plasma Interactions*, in: D. Batani, C.J. Joachain, S. Martellucci and A.N. Chester (Eds.), *Atoms, Solids, and Plasmas in Super-Intense Laser Fields*, Kluwer Academic/Plenum Publishers, New York, NY (2001).

[17] M.H. Key, M.D. Cable, T.E. Cowan, K.G. Estabrook, B.A. Hammel, S.P. Hatchett, E.A. Henry, D.E. Hinkel, J.D. Kilkenny, J.A. Koch, W.L. Kruer, A.B. Langdon, B.F. Lasinski, R.W. Lee, B.J. MacGowan, A. MacKinnon, J.D. Moody, M.J. Moran, A.A. Offenberger, D.M. Pennington, M.D. Perry, T.J. Phillips, T.C. Sangster, M.S. Singh, M.A. Stoyer, M. Tabak, G.L. Tietbohl, M. Tsukamoto, K. Wharton and S.C. Wilks, *Hot electron production and heating by hot electrons in fast ignitor research*, Phys. Plasmas **5**, 1966 (1998).

[18] H. Alfvén, *On the Motion of Cosmic Rays in Interstellar Space*, Phys. Rev. **55**, 425 (1939).

[19] J.R. Davies, *The Alfvén limit revisited and its relevance to laser-plasma interactions*, Laser Part. Beams **24**, 299 (2006).

[20] J.J. Santos, A. Debayle, Ph. Nicolaï, V. Tikhonchuk, M. Manclossi, D. Batani, A. Guemnie-Tafo, J. Faure, V. Malka and J.J. Honrubia, *Fast-electron transport and induced heating in aluminum foils*, Phys. Plasmas **14**, 103107 (2007).

[21] A. Pukhov, *Three-Dimensional Simulations of Ion Acceleration from a Foil Irradiated by a Short-Pulse Laser*, Phys. Rev. Lett. **86**, 3562 (2001).

[22] S.C. Wilks, A.B. Langdon, T.E. Cowan, M. Roth, M. Singh, S. Hatchett, M.H. Key, D. Pennington, A. MacKinnon and R.A. Snavely, *Energetic proton generation in ultra-intense laser–solid interactions*, Phys. Plasmas **8**, 542 (2001).

[23] L. Romagnani, J. Fuchs, M. Borghesi, P. Antici, P. Audebert, F. Ceccherini, T. Cowan, T. Grismayer, S. Kar, A. Macchi, P. Mora, G. Pretzler, A. Schiavi, T. Toncian and O. Willi, *Dynamics of Electric Fields Driving the Laser Acceleration of Multi-MeV Protons*, Phys. Rev. Lett. **95**, 195001 (2005).

[24] H. Ruhl, T. Cowan and J. Fuchs, *The generation of micro-fiducials in laser-accelerated proton flows, their imaging property of surface structures and application for the characterization of the flow*, Phys. Plasmas **11**, L17 (2004).

[25] Y. Sentoku, T.E. Cowan, A. Kemp and H. Ruhl, *High energy proton acceleration in interaction of short laser pulse with dense plasma target*, Phys. Plasmas **10**, 2009 (2003).

[26] T. Ceccotti, A. Lévy, H. Popescu, F. Réau, P. D'Oliveira, P. Monot, J.P. Geindre, E. Lefebvre and Ph. Martin, *Proton Acceleration with High-Intensity Ultrahigh-Contrast Laser Pulses*, Phys. Rev. Lett. **99,** 185002 (2007).

[27] J.C. Fernández, B.M. Hegelich, J.A. Cobble, K.A. Flippo, S.A. Letzring, R.P. Johnson, D.C. Gautier, T. Shimada, G.A. Kyrala, Y. Wang, C.J. Wetteland and J. Schreiber, *Laser-ablation treatment of short-pulse laser targets: Toward an experimental program on energetic-ion interactions with dense plasmas*, Laser Part. Beams **23**, 267 (2005).

[28] K. Nemoto, A. Maksimchuk, S. Banerjee, K. Flippo, G. Mourou, D. Umstadter and V.Yu. Bychenkov, *Laser-triggered ion acceleration and table top isotope production*, Appl. Phys. Lett. **78**, 595 (2001).

[29] A.J. Mackinnon, M. Borghesi, S. Hatchett, M.H. Key, P.K. Patel, H. Campbell, A. Schiavi and R. Snavely, *Effect of Plasma Scale Length on Multi-MeV Proton Production by Intense Laser Pulses*, Phys. Rev. Lett. **86**, 1769 (2001).

[30] M. Allen, P.K. Patel, A. Mackinnon, D. Price, S. Wilks and E. Morse, *Direct experimental evidence of back-surface ion acceleration from laser-irradiated gold foils*, Phys. Rev. Lett. **93**, 265004 (2004).

[31] E. d'Humières, E. Lefebvre, L. Gremillet and V. Malka, *Proton acceleration mechanisms in high-intensity laser interaction with thin foils*, Phys. Plasmas **12**, 062704 (2005).

[32] J. Fuchs, Y. Sentoku, S. Karsch, J. Cobble, P. Audebert, A. Kemp, A. Nikroo, P. Antici, E. Brambrink, A. Blazevic, E M. Campbell, J.C. Fernández, J.-C. Gauthier, M. Geissel, M. Hegelich, H. Pépin, H. Popescu, N. Renard-LeGalloudec, M. Roth, J. Schreiber, R. Stephens and T. E. Cowan, *Comparison of Laser Ion Acceleration from the Front and Rear Surfaces of Thin Foils*, Phys. Rev. Lett. **94**, 045004 (2005).

[33] P. Mora, *Plasma Expansion into a Vacuum*, Phys. Rev. Lett. **90,** 185002 (2003).

[34] J. Fuchs, P. Antici, E. d'Humières, E. Lefebvre, M. Borghesi, E. Brambrink, C.A. Cecchetti, M. Kaluza, V. Malka, M. Manclossi, S. Meyroneinc, P. Mora, J. Schreiber, T. Toncian, H. Pépin and P. Audebert, *Laser-driven proton scaling laws and new paths towards energy increase*, Nat. Phys. 2, 48 (2006).

[35] P. Mora, *Thin-foil expansion into a vacuum*, Phys. Rev. E **72**, 056401 (2005).

[36] P. Mora, *Collisionless expansion of a Gaussian plasma into a vacuum*, Phys. Plasmas **12**, 112102 (2005).

[37] M. Passoni, V.T. Tikhonchuk, M. Lontano and V.Yu. Bychenkov, *Charge separation effects in solid targets and ion acceleration with a two-temperature electron distribution*, Phys. Rev. E **69**, 026411 (2004).

[38] M.D. Perry, D. Pennington, B.C. Stuart, G. Tietbohl, J.A. Britten, C. Brown, S. Herman, B. Golick, M. Kartz, J. Miller, H.T. Powell, M. Vergino and V. Yanovsky, *Petawatt laser pulses*, Opt. Lett. **24**, 160 (1999).

[39] M. Honda, J. Meyer-ter-Vehn and A. Pukhov, *Collective Stopping and Ion Heating in Relativistic-Electron-Beam Transport for Fast Ignition*, Phys. Rev. Lett. **85**, 2128 (2000).

[40] Frank Hinterberger, *Physik der Teilchenbeschleuniger und Ionenoptik*, 2nd edition, Springer-Verlag, Berlin/Heidelberg (2008).

[41] J. Fuchs, T.E. Cowan, P. Audebert, H. Ruhl, L. Gremillet, A. Kemp, M. Allen, A. Blazevic, J.-C. Gauthier, M. Geissel, M. Hegelich, S. Karsch, P. Parks, M. Roth, Y. Sentoku, R. Stephens and E.M. Campbell, *Spatial Uniformity of Laser-Accelerated Ultrahigh-Current MeV Electron Propagation in Metals and Insulators*, Phys. Rev. Lett. **91**, 255002 (2003).

[42] J. Schreiber, S. Ter-Avetisyan, E. Risse, M.P. Kalachnikov, P.V. Nickles, W. Sandner, U. Schramm, D. Habs, J. Witte and M. Schnürer, *Pointing of laser-accelerated proton beams*, Phys. Plasmas **13**, 033111 (2006).

[43] M. Borghesi, J. Fuchs, S.V. Bulanov, A.J. Mackinnon, P.K. Patel and M. Roth, *Fast ion generation by high-intensity laser irradiation of solid targets and applications*, Fusion Sci. Technol. **49**, 412 (2006).

[44] M. Kaluza, J. Schreiber, M.I.K. Santala, G.D. Tsakiris, K. Eidmann, J. Meyer-ter-Vehn and K.J. Witte, *Influence of the Laser Prepulse on Proton Acceleration in Thin-Foil Experiments*, Phys. Rev. Lett. **93**, 045003 (2004).

[45] M. Schollmeier, K. Harres, F. Nürnberg, A. Blažević, P. Audebert, E. Brambrink, J. C. Fernández, K.A. Flippo, D.C. Gautier, M. Geißel, B.M. Hegelich, J. Schreiber and M. Roth, *Laser beam-profile impression and target thickness impact on laser-accelerated protons*, Phys. Plasmas **15**, 053101 (2008).

[46] A.J. Kemp, J. Fuchs, Y. Sentoku, V. Sotnikov, M. Bakeman, P. Antici and T.E. Cowan, *Emittance growth mechanisms for laser-accelerated proton beams*, Phys. Rev. E **75**, 056401 (2007).

[47] J. Fuchs, C.A. Cecchetti, M. Borghesi, T. Grismayer, E. d'Humières, P. Antici, S. Atzeni, P. Mora, A. Pipahl, L. Romagnani, A. Schiavi, Y. Sentoku, T. Toncian, P. Audebert and O. Willi, *Laser-Foil Acceleration of High-Energy Protons in Small-Scale Plasma Gradients*, Phys. Rev. Lett. **99**, 015002 (2007).

[48] P.K. Patel, A.J. Mackinnon, M.H. Key, T.E. Cowan, M.E. Foord, M. Allen, D.F. Price, H. Ruhl, P.T. Springer and R. Stephens, *Isochoric Heating of Solid-Density Matter with an Ultrafast Proton Beam*, Rev. Lett. **91**, 125004 (2003).

[49] A. Heller, *Using proton beams to create and probe plasma*, Science & Technology Review, December 2003, pp. 11-16.

[50] T. Toncian, M. Borghesi, J. Fuchs, E. d'Humières, P. Antici, P. Audebert, E. Brambrink, C.A. Cecchetti, A. Pipahl, L. Romagnani and O. Willi, *Ultrafast Laser-Driven Microlens to Focus and Energy-Select Mega-Electron Volt Protons*, Science **312**, 410 (2006).

[51] M. Schollmeier, S. Becker, M. Geißel, K.A. Flippo, A. Blažević, S.A. Gaillard, D.C. Gautier, F. Grüner, K. Harres, M. Kimmel, F. Nürnberg, P. Rambo, U. Schramm, J. Schreiber, J. Schütrumpf, J. Schwarz, N.A. Tahir, B. Atherton, D. Habs, B.M. Hegelich and M. Roth, *Controlled Transport and Focusing of Laser-Accelerated Protons with Miniature Magnetic Devices*, Phys. Rev. Lett. **101**, 055004 (2008).

[52] T. Eichner, F. Grüner, S. Becker, M. Fuchs, D. Habs, R. Weingartner, U. Schramm, H. Backe, P. Kunz and W. Lauth, *Miniature magnetic devices for laser-based, table-top free-electron lasers*, Phys. Rev. ST Accel. Beams **10**, 082401 (2007).

[53] T.Zh. Esirkepov, S.V. Bulanov, K. Nishihara, T. Tajima, F. Pegoraro, V.S. Khoroshkov, K. Mima, H. Daido, Y. Kato, Y. Kitagawa, K. Nagai and S. Sakabe, *Proposed Double-Layer Target for the Generation of High-Quality Laser-Accelerated Ion Beams*, Phys. Rev. Lett. **89**, 175003 (2002).

[54] B.M. Hegelich, B.J. Albright, J. Cobble, K. Flippo, S. Letzring, M. Paffett, H. Ruhl, J. Schreiber, R.K. Schulze and J.C. Fernández, *Laser acceleration of quasi-monoenergetic MeV ion beams*, Nature **439**, 441 (2006).

[55] H. Schwoerer, S. Pfotenhauer, O. Jäckel, K.-U. Amthor, B. Liesfeld, W. Ziegler, R. Sauerbrey, K.W.D. Ledingham and T. Esirkepov, *Laser–plasma acceleration of quasi-monoenergetic protons from microstructured targets*, Nature **439**, 445 (2006).

[56] A.P.L. Robinson and P. Gibbon, *Production of proton beams with narrow-band energy spectra from laser-irradiated ultrathin foils*, Phys. Rev. E **75**, 015401 (2007).

[57] S.M. Pfotenhauer, O. Jäckel, A. Sachtleben, J. Polz, W. Ziegler, H.-P. Schlenvoigt, K.-U. Amthor, M.C. Kaluza, K.W.D. Ledingham, R. Sauerbrey, P. Gibbon, A.P.L. Robinson and H. Schwoerer*, Spectral shaping of laser generated proton beams*, New J. Phys. **10**, 033034 (2008).

[58] S. Ter-Avetisyan, M. Schnürer, P.V. Nickles, M. Kalashnikov, E. Risse, T. Sokollik, W. Sandner, A. Andreev and V. Tikhonchuk, *Quasimonoenergetic Deuteron Bursts Produced by Ultraintense Laser Pulses*, Phys. Rev. Lett. **96**, 145006 (2006).

[59] A.V. Brantov, V.T. Tikhonchuk, O. Klimo, D.V. Romanov, S. Ter-Avetisyan, M. Schnürer, T. Sokollik and P.V. Nickles, *Quasi-mono-energetic ion acceleration from a homogeneous composite target by an intense laser pulse*, Phys. Plasmas **13**, 122705 (2006).

[60] K.A. Flippo, E. d'Humières, S.A. Gaillard, J. Rassuchine, D.C. Gautier, M. Schollmeier, F. Nürnberg, J.L. Kline, J. Adams, B. Albright, M. Bakeman, K. Harres, R.P. Johnson, G. Korgan, S. Letzring, S. Malekos, N. Renard-LeGalloudec, Y. Sentoku, T. Shimada, M. Roth, T.E. Cowan, J.C. Fernández and B.M. Hegelich, *Increased efficiency of short-pulse laser-generated proton beams from novel flat-top cone targets*, Phys. Plasmas **15**, 056709 (2008).

[61] R. Kodama, Y. Sentoku, Z.L. Chen, G.R. Kumar, S.P. Hatchett, Y. Toyama, T.E. Cowan, R.R. Freeman, J. Fuchs, Y. Izawa, M.H. Key, Y. Kitagawa, K. Kondo, T. Matsuoka, H. Nakamura, M. Nakatsutsumi, P.A. Norreys, T. Norimatsu, R.A. Snavely, R.B. Stephens, M. Tampo, K.A. Tanaka and T. Yabuuchi, *Plasma devices to guide and collimate a high density of MeV electrons*, Nature **432**, 1005 (2004).

[62] T. Esirkepov, M. Borghesi, S.V. Bulanov, G. Mourou and T. Tajima, *Highly Efficient Relativistic-Ion Generation in the Laser-Piston Regime*, Phys. Rev. Lett. **92**, 175003 (2004).

[63] T.V. Liseikina, D. Prellino, F. Cornolti and A. Macchi, *Ponderomotive Acceleration of Ions: Circular Versus Linear Polarization*, IEEE T. Plasma Sci. **36**, 1866 (2008).

[64] L. Yin, B.J. Albright, B.M. Hegelich and J.C. Fernández, *GeV laser ion acceleration from ultrathin targets: The laser break-out afterburner*, Laser Part. Beams **24**, 291 (2006).

[65] M. Hegelich, S. Karsch, G. Pretzler, D. Habs, K. Witte, W. Guenther, M. Allen, A. Blazevic, J. Fuchs, J.C. Gauthier, M. Geissel, P. Audebert, T. Cowan and M. Roth, *MeV Ion Jets from Short-Pulse-Laser Interaction with Thin Foils*, Phys. Rev. Lett. **89**, 085002 (2002).

[66] K. Flippo, B.M. Hegelich, B.J. Albright, L. Yin, D.C. Gautier, S. Letzring, M. Schollmeier, J. Schreiber, R. Schulze and J.C. Fernández, *Laser-driven ion accelerators: Spectral control, monoenergetic ions and new acceleration mechanisms*, Laser Part. Beams **25**, 3 (2007).

[67] A.M. Koehler, *Proton Radiography*, Science **160**, 303 (1968).

[68] M. Borghesi, A. Schiavi, D.H. Campbell, M.G. Haines, O. Willi, A.J. MacKinnon, L.A. Gizzi, M. Galimberti, R.J. Clarke and H. Ruhl, *Proton imaging: a diagnostic for inertial confinement fusion/fast ignitor studies*, Plasma Phys. Control. Fusion **43**, A267 (2001).

[69] D. West and A.C. Sherwood, *Radiography with 160 MeV protons*, Nature **239**, 157 (1972).

[70] A.J. Mackinnon, P.K. Patel, M. Borghesi, R.C. Clarke, R.R. Freeman, H. Habara, S.P. Hatchett, D. Hey, D.G. Hicks, S. Kar, M.H. Key, J.A. King, K. Lancaster, D. Neely, A. Nikkro, P.A. Norreys, M.M. Notley, T.W. Phillips, L. Romagnani, R.A. Snavely, R.B. Stephens and R.P.J. Town, *Proton Radiography of a Laser-Driven Implosion*, Phys. Rev. Lett. **97**, 045001 (2006).

[71] J.R. Rygg, F.H. Séguin, C.K. Li, J.A. Frenje, M.J.-E. Manuel, R.D. Petrasso, R. Betti, J.A. Delettrez, O.V. Gotchev, J.P. Knauer, D.D. Meyerhofer, F.J. Marshall, C. Stoeckl and W. Theobald, *Proton Radiography of Inertial Fusion Implosions*, Science **319**, 1223 (2008).

[72] National Research Council (U.S.) Committee on High Energy Density Plasma Physics, *Frontiers in High Energy Density Physics: The X-Games of Contemporary Science*, National Academic Press, Washington, D.C. (2003).

[73] R.A. Snavely, B. Zhang, K. Akli, Z. Chen, R.R. Freeman, P. Gu, S.P. Hatchett, D. Hey, J. Hill, M.H. Key, Y. Izawa, J. King, Y. Kitagawa, R. Kodama, A.B. Langdon, B.F. Lasinski, A. Lei, A.J. MacKinnon, P. Patel, R. Stephens, M. Tampo, K.A. Tanaka, R. Town, Y. Toyama, T. Tsutsumi, S.C. Wilks, T. Yabuuchi and J. Zheng, *Laser generated proton beam focusing and high temperature isochoric heating of solid matter*, Phys. Plasmas **14**, 092703 (2007).

[74] P. Antici, M. Fazi, A. Lombardi, M. Migliorati, L. Palumbo, P. Audebert and J. Fuchs, *Postacceleration of laser-generated high-energy protons through conventional accelerator linacs*, IEEE T. Plasma Sci. **36**, 1843 (2008).

[75] S. Pfalzner, *An Introduction To Inertial Confinement Fusion*, Taylor & Francis, New York/London (2006).

[76] M. Tabak, J. Hammer, M.E. Glinsky, W.L. Kruer, S.C. Wilks, J. Woodworth, E.M. Campbell, M.D. Perry and R.J. Mason, *Ignition and high gain with ultrapowerful lasers*, Phys. Plasmas **1**, 1626 (1994).

[77] M. Roth, T.E. Cowan, M.H. Key, S.P. Hatchett, C. Brown, W. Fountain, J. Johnson, D.M. Pennington, R.A. Snavely, S.C. Wilks, K. Yasuike, H. Ruhl, F. Pegoraro, S.V. Bulanov, E.M. Campbell, M.D. Perry and H. Powell, *Fast Ignition by Intense Laser-Accelerated Proton Beams*, Phys. Rev. Lett. **86**, 436 (2001).

[78] M. Roth, E. Brambrink, P. Audebert, M. Basko, A. Blazevic, R. Clarke, J. Cobble, T.E. Cowan, J. Fernandez, J. Fuchs, M. Hegelich, K. Ledingham, B.G. Logan, D. Neely, H. Ruhl and M. Schollmeier, *Laser accelerated ions in ICF research prospects and experiments*, Plasma Phys. Control. Fusion **47**, B841 (2005).

[79] M. Temporal, *Fast ignition of a compressed inertial confinement fusion hemispherical capsule by two proton beams*, Phys. Plasmas **13**, 122704 (2006).

[80] M. Temporal, J.J. Honrubia and S. Atzeni, *Proton-beam driven fast ignition of inertially confined fuels: Reduction of the ignition energy by the use of two proton beams with radially shaped profiles*, Phys. Plasmas **15**, 052702 (2008).

[81] M.I.K. Santala, M. Zepf, F.N. Beg, E.L. Clark, A.E. Dangor, K. Krushelnick, M. Tatarakis, I. Watts, K.W.D. Ledingham, T. McCanny, I. Spencer, A.C. Machacek, R. Allott, R.J. Clarke and P.A. Norreys, *Production of radioactive nuclides by energetic protons generated from intense laser-plasma interactions*, Appl. Phys. Lett. **78**, 19 (2001).

[82] I. Spencer, K.W.D. Ledingham, R.P. Singhal, T. McCanny, P. McKenna, E.L. Clark, K. Krushelnick, M. Zepf, F.N. Beg, M. Tatarakis, A.E. Dangor, P.A. Norreys, R.J. Clarke, R.M. Allott and I.N. Ross, *Laser generation of proton beams for the production of short-lived positron emitting radioisotopes*, Nucl. Instr. Meth. B **183**, 449 (2001).

[83] K.W.D. Ledingham, P. McKenna, T. McCanny, S. Shimizu, J.M. Yang, L. Robson, J. Zweit, J.M. Gillies, J. Bailey, G.N. Chimon, R.J. Clarke, D. Neely, P.A. Norreys, J.L. Collier, R.P. Singhal, M.S. Wei, S.P.D. Mangles, P. Nilson, K. Krushelnick and M. Zepf, *High power laser production of short-lived isotopes for positron emission tomography*, J. Phys. D: Appl. Phys. **37**, 2341 (2004).

[84] Stabsstelle Presse- und Öffentlichkeitsarbeit (Press and Public Relations Office) des Universitätsklinikums Heidelberg und der Medizinischen Fakultät der Universität Heidelberg, *The Heidelberg Ion-Beam Therapy Center HIT*, Heidelberg (2008).

[85] D. Schardt and the Heavy-Ion Therapy Collaboration, *Tumor therapy with high-energy carbon ion beams*, Nucl. Phys. A **787**, 633 (2007).

[86] Ute Linz and Jose Alonso, *What will it take for laser driven proton accelerators to be applied to tumor therapy?* Phys. Rev. ST Accel. Beams **10**, 094801 (2007).

[87] S.V. Bulanov and V.S. Khoroshkov, *Feasibility of Using Laser Ion Accelerators in Proton Therapy*, Plasma Phys. Rep. **28**, 453 (2002), translated from Fizika Plazmy **28**, 493 (2002).

[88] C. Rullière (Ed.), *Femtosecond Laser Pulses – Principles and Experiments*, 2nd edition, Springer, New York, NY (2005).

[89] J. Eichler and H.J. Eichler, *Laser – Bauformen, Strahlführung, Anwendungen*, 6th edition, Springer, Berlin/Heidelberg (2006).

[90] D. Strickland and G. Mourou, *Compression of amplified chirped optical pulses*, Opt. Commun. **56**, 219 (1985).

[91] H.C. Kapteyn, M.M. Murnane, A. Szoke and R.W. Falcone, *Prepulse energy suppression for high-energy ultrashort pulses using self-induced plasma shuttering*, Optics Letters **16**, 490 (1991).

[92] International Speciality Products, http://www.gafchromic.com

[93] Fujifilm, http://www.fujifilm.com/products/life_science/si_imgplate/img_plate.html

[94] V.R. Oganesyan, *Untersuchung des Porenöffnungsprozesses latenter Spuren leichter niederenergetischer Ionen in CR-39 mittels elektrolytischer Ätzung*, Dissertation, Technischen Universität Dresden (2005).

[95] S.A. Durrani and R.K. Bull, *Solid state nuclear track detection: principles, methods and applications*, Pergamon Press, Oxford, UK (1987).

[96] J.L. Wiza, *Microchannel Plate Detectors*, Nucl. Instrum. Methods **162**, 587 (1979).

[97] J.J. Thomson, *Rays of Positive Electricity*, Phil. Mag. **21**, 255 (1911).

[98] W. Demtröder, *Experimentalphysik 3 – Atome, Moleküle und Festkörper*, Springer, Berlin/Heidelberg (2005).

[99] M. Borghesi, L. Romagnani, A. Schiavi, D.H. Campbell, M.G. Haines, O. Willi, A.J. Mackinnon, M. Galimberti, L. Gizzi, R. J. Clarke and S. Hawkes, *Measurement of highly transient electrical charging following high-intensity laser–solid interaction*, Appl. Phys. Lett. **82**, 1529 (2003).

[100] S. Busch, M. Schnürer, M. Kalashnikov, H. Schönnagel, H. Stiel, P. V. Nickles, W. Sandner, S. Ter-Avetisyan, V. Karpov and U. Vogt, *Ion acceleration with ultrafast lasers*, Appl. Phys. Lett. **82**, 3354 (2003).

[101] T. Toncian, *Ultrafast Laser Driven Micro-Lens to Focus and Energy Select MeV Protons*, Dissertation, Heinrich-Heine-Universität, Düsseldorf (2008).

Die hier vorgelegte Dissertation habe ich eigenständig und ohne unerlaubte Hilfe angefertigt. Die Dissertation wurde in der vorgelegten oder in ähnlicher Form noch bei keiner anderen Institution eingereicht. Ich habe bisher keine erfolglosen Promotionsversuche unternommen.

Düsseldorf, den 18.12.2008